Stony Brook University

Measurement of the Single Neutral Pion Production Cross Section in Neutral-Current Neutrino Interactions in the T2K Pi-zero Detector

A Dissertation Presented

by

Glenn David Lopez

to

The Graduate School

in Partial Fulfillment of the

Requirements

for the Degree of

Doctor of Philosophy

in

Physics

Stony Brook University

May 2012

Stony Brook University

The Graduate School

Glenn David Lopez

We, the dissertation committee for the above candidate for the
Doctor of Philosophy degree, hereby recommend
acceptance of this dissertation.

Dr. Chang Kee Jung - Dissertation Advisor
Professor of Physics, Department of Physics and Astronomy

Dr. George Sterman - Chairperson of Defense
Distinguished Professor of Physics, Department of Physics and Astronomy

Dr. Thomas Weinacht
Associate Professor of Physics, Department of Physics and Astronomy

Dr. Vittorio Paolone
Associate Professor of Physics, University of Pittsburgh

This dissertation is accepted by the Graduate School.

Charles Taber
Interim Dean of the Graduate School

Abstract of the Dissertation

Measurement of the Single Neutral Pion Production Cross Section in Neutral-Current Neutrino Interactions in the T2K Pi-zero Detector

by

Glenn David Lopez

Doctor of Philosophy

in

Physics

Stony Brook University

2012

The T2K experiment is a long baseline neutrino oscillation experiment designed for the primary goal of measuring $\nu_\mu \rightarrow \nu_e$ oscillation, thereby providing a measurement of the neutrino mixing angle θ_{13}. To achieve this goal, a beam of muon neutrinos is produced at the Japanese Proton Accelerator Research Complex in Tokai, Japan and sent 295 kilometers across Japan towards the Super-Kamiokande detector. One of the major backgrounds of the ν_e appearance measurement is from neutral current ν_μ interactions where a single π^0 is produced and the photons from the π^0 decay mimic the ν_e appearance signal. To constrain the uncertainty on this background, a π^0-detector has been constructed as part of the T2K near detector facility at 280 meters from the proton beam target. This dissertation presents a measurement of the neutral current single π^0 (NC1π^0) production cross section using 8.55×10^{19} protons-on-target (POT) of T2K data. This is achieved by using pre-defined selection criteria to enhance the NC1π^0 signal events over background events in the invariant mass distribution of NC1π^0 candidate events. An extended likelihood fit is then performed on the data distribution to extract the number of signal events. We measure the ratio of the NC1π^0production cross section normalized by the ν_μ Charged-Current Inclusive interaction to be 0.81 ± 0.15 (stat) ± 0.14 (sys).

Contents

List of Tables

List of Figures

Acknowledgments

I would first like to give thanks to the members of the PØD π^0 group, in alphabetical order, Bruce Berger, Norm Buchanan, Fahmida Khanam, Dan Ruterbories, and Jackie Schwehr. Without their contributions to the T2K technical note, this thesis wouldn't be possible.

I would like to thank the other members of the T2K USB280 group whose contributions led to the success of the PØD. And thanks to the T2K Collaboration as a whole. After 8 years, you meet so many people that listing them individually is just not possible. I would like to especially thank Dave Warner, who designed and built the PØD. Thanks to Maki Sakurai for being the best secretary ever in addition to being a great friend. And thanks to Kevin Connolly for the good company in Japan.

I would like to thank the conveners of the T2K π^0 group for their assistance with the analysis, especially Antonin Vacheret for his insight and advice. I also owe a lot to Clark McGrew, who saw this analysis through to the end.

Thank you to the members of the Stony Brook NNGroup - Chiaki Yanagisawa, and Peter Paul, for that time when he ripped my presentation to shreds in order to make it better. Thanks to Ian Taylor for being the incredible postdoc that he is. I've learned a lot from him in the short time that he's been at Stony Brook. Thank you to Karin Gilje for contributing greatly to this analysis. Thanks to the current students Dima Beznosko, Joshua Hignight, and Jay Hyun Jo. Thank you to the group secretaries Joan Napolitano, Alice Dugan, and Jennifer Flynn. And special thanks to the past NNGroup students Fumi Kato, Ryan Terri, and Lisa Whitehead for the good times.

I would like to thank Leah Morabito and Aubrey Henretty for proofreading this thesis. I thank my mom for being the wonderful person that she is. I thank my girlfriend, Katherine Alatalo, for her love and support 2500 miles away. I also thank the rest of my friends and family for being there.

Finally, I would like to thank my advisor, Chang Kee Jung for being like a father to me during my graduate school career, and for not giving up on me despite me giving him every opportunity to do so.

Chapter 1

Introduction

The neutrino is a fundamental particle of nature occuring in a wide variety of phenomena throughout our universe. Despite their abundance, neutrinos are extremely difficult to detect and study because they can only interact with familiar matter via the weak nuclear force and, to a lesser extent, gravity. As a result, several of the neutrino's properties remain unknown to this day. In this chapter we will examine the history of the neutrino, from its theoretical introduction to its experimental discovery. We will also survey several topics in neutrino physics that pertain to this dissertation.

1.1 History of the Neutrino

The history of the neutrino begins with the discovery of radioactivity by Henri Becquerel in 1896 [1]. Shortly thereafter, Ernest Rutherford observed that the by-products of radioactivity came in two types, corresponding to α- and β-decay [2], with γ radiation discovered later by Paul Villard [3]. Thereafter it was discovered that the energy spectra in β-decay were continuous, in contrast to α and γ spectra, which were discrete. This discovery provided scientists with the first physical evidence of the neutrino. The reason is that in a two-body decay, as β-decay was believed to be at the time, where nucleus A decays at rest into a lighter nucleus B and an electron, the energy of the electron is emitted with an energy given by the equation

$$E_e = \frac{m_A^2 + m_e^2 - m_B^2}{2m_A} \tag{1.1}$$

which, with the masses being fixed for a given nucleus, should yield a discrete energy spectrum if energy is to be conserved. While some scientists, most notably Niels Bohr, were prepared to abandon strict conservation of energy, Wolfgang Pauli offered a different solution. In a now famous letter [4] to the attendees at a physics conference in Tubingen, Pauli wrote:

> I have hit upon a desperate remedy to save the...law of conservation of energy. Namely, the possibility that in the nuclei there could exist electrically neutral particles, which I will call neutrons, that have spin 1/2 and obey the exclusion principle and that further differ from light quanta in that they do not travel with the velocity of light. The mass of the neutrons should be of the same order of magnitude as the electron mass and in any event not larger than 0.01 proton mass. - The continuous beta spectrum would then make sense with the assumption that in beta decay, in addition to the electron, a neutron is emitted such that the sum of the energies of neutron and electron is constant.

Pauli named his particle the neutron, and in 1932 James Chadwick discovered the neutron as it is known today. It was, however, too heavy to be the particle Pauli spoke of, and so as a result, Pauli's "neutron" was renamed "neutrino" by Enrico Fermi.

At the time there was skepticism over whether the neutrino would or could ever be observed. Pauli himself is alleged to have said, "I have done something very bad today in proposing a particle that cannot be detected; it is something no theorist should ever do." However, 25 years after Pauli's initial proposal, the neutrino was directly observed by Frederick Reines and Clyde Cowan in 1956 at the Savannah River reactor [5]. Their strategy was to detect the neutrinos from the reactor via inverse β-decay

$$\overline{\nu}_e + p \rightarrow e^+ + n. \tag{1.2}$$

Using an experimental setup consisting of $CdCl_2$ dissolved in water and surrounded by liquid scintillator, they observed the neutrino interaction by detecting the 511 keV photons from positron-electron annihilation followed by a delayed neutron capture signal. In 1995 their work was finally honored with the Nobel Prize.

In 1962, Leon Lederman, Melvin Schwartz, and Jack Steinberger discovered a new type of neutrino, the ν_μ, at Brookhaven Laboratory. Their work was based on an earlier suggestion by Pontecorvo that the ν_μ would be distinct from the ν_e if the process

$$\nu_\mu + n \rightarrow p + e^- \tag{1.3}$$

was forbidden. Their experiment, the first of its kind to create neutrinos with an accelerator, used the Brookhaven AGS to produce a highly pure ν_μ beam, which was then sent towards a spark chamber detector that detected the neutrino interactions. The resulting observation [6], 29 μ-like events and only 6 e-like events, confirmed Pontecorvo's suggestion. For their work, they were awarded the Nobel Prize in 1988.

Table 1.1: Summary of the elementary particles that make up the Standard Model. The top table shows the fermions, the bottom table shows the bosons.

Particles	Flavor			Charge
Quarks	u	c	t	$+^2/_3$
	d	s	b	$-^1/_3$
Leptons	ν_e	ν_μ	ν_τ	0
	e	μ	τ	-1

Force	Electromagnetic	Weak	Strong
Mediator	γ	$W^{\pm}$, Z^0	g

With the formulation of the electroweak theory by Glashow, Weinberg, and Salam, it was predicted that there should be another type of neutrino interaction via the exchange of the Z boson. In 1973 this prediction was verified by the Gargamelle experiment at CERN which observed events without a charged lepton in the final state, thus establishing the existence of neutral current interactions [7, 8].

In 1975, the discovery of the tau lepton implied the existence of a third type of neutrino, the ν_τ. In 2000, the DONUT Collaboration at the Fermi National Accelerator Laboratory made the first direct observation of the tau neutrino [9].

1.2 Neutrinos in the Standard Model

The Standard Model of particle physics [10] is the phenomenological framework that describes the interaction of the fundamental particles in terms of the strong and electroweak forces, with gravity excluded. In the Standard Model, particles are classified as fermions and bosons. The fermions are comprised of quarks and leptons, each consisting of 3 generations, the first of which makes up nearly all matter as we know it. The bosons are the photons, the weak gauge bosons, and the gluons which act as the mediators of the electromagnetic, weak and strong nuclear forces, respectively. Table 1.1 shows the particles that make up the Standard Model

In the Standard Model, there are 3 generations of neutrinos, ν_e, ν_μ, and ν_τ, corresponding to the electron, muon and tau leptons. Neutrinos have no electrical charge and no color, so they do not interact via the electromagnetic or strong interactions. Neutrinos interact with leptons and quarks solely through the weak interaction by exchanging the weak gauge bosons W and Z corre-

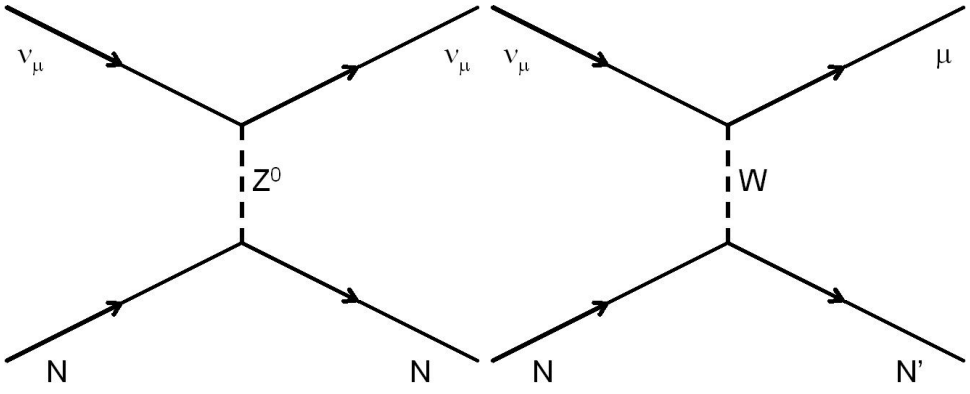

Figure 1.1: Left: Interaction via the neutral current. Right: Interaction via the charged current.

sponding to charged and neutral current interaction, respectively. Figure 1.1 shows Feynman diagrams for these interactions.

Neutrinos in nature are all characterized as having left-handed helicity, with anti-neutrinos having right-handed helicity. The neutrino helicity was first measured in a famous experiment by Goldhaber *et. al* [11], in 1958. For a spin-$\frac{1}{2}$ particle obeying the Dirac equation, both left and right-handed helicity states are required to produce a mass term. As a result, neutrinos in the Standard Model were assumed to be massless. Evidence of a non-zero neutrino mass can be thought of as one example of new physics beyond the Standard Model.

1.3 Neutrino Mass and Mixing

Despite the assumed masslessness of the neutrino, experiments have attempted to measure the mass of the neutrino. By observing the characteristics of β-decay, π-decay and τ-decay it is possible for an effective mass of the ν_e, ν_μ and ν_τ to be inferred. So far only the upper limits $m_{\nu_e} < 2$ eV, $m_{\nu_\mu} <$ 0.19 MeV, and $m_{\nu_\tau} < 18.2$ MeV[12]have been measured. A non-zero neutrino mass would also have implications on cosmological observations. Based on measurements of the Lyman-α forest power spectrum and cosmic microwave background, the limit on the sum of the neutrino masses has been determined to be $\sum m_\nu = 0.17$ eV [13].

1.3.1 Neutrino Oscillation

Neutrino oscillation is a quantum mechanical phenomenon in which the neutrino flavor eigenstate changes as it propagates. This change is a result of

the interference between different neutrino masses. Neutrino oscillation was first proposed in 1957 by Bruno Pontecorvo as an oscillation between neutrino and anti-neutrino states [14]. The oscillation of neutrino flavor was formulated by Maki, Nakagawa and Sakata in 1962 [15].

If neutrinos have mass, then in addition to the neutrino flavor eigenstates $|\nu_\alpha\rangle$ ($\alpha = e, \mu, \tau$), there exist mass eigenstates $|\nu_i\rangle$ ($i = 1, 2, 3$). In general, the flavor eigenstates and mass eigenstates do not have to be equivalent. They are instead related to each other by the linear superposition

$$|\nu_\alpha\rangle = \sum_i U^*_{\alpha i}|\nu_i\rangle. \tag{1.4}$$

The quantity $U^*_{\alpha i}$ is a unitary matrix known as the Pontecorvo-Maki-Nakagawa-Sakata (PMNS) matrix. The mass eigenstates are stationary states of the free particle hamiltonian

$$H|\nu_i\rangle = E_i|\nu_i\rangle \tag{1.5}$$

with the energy E_i given by

$$E_i = \sqrt{p_i^2 + m_i^2}. \tag{1.6}$$

Solving the Time-Dependant Schrodinger equation, we obtain

$$|\nu_i(t)\rangle = e^{-iE_i t}|\nu_i\rangle \tag{1.7}$$

for the mass eigenstates at a time t. Inserting this result into Equation 1.4 gives the flavor eigenstates as a function of time:

$$|\nu_\alpha(t)\rangle = \sum_i U^*_{\alpha i} e^{-iE_i t}|\nu_i\rangle. \tag{1.8}$$

By inverting Equation 1.4, the mass eigenstates are given by:

$$|\nu_i\rangle = \sum_\alpha U_{\alpha i}|\nu_\alpha\rangle. \tag{1.9}$$

Inserting this result into Equation 1.8, the time evolution of the flavor eigenstates becomes

$$|\nu_\alpha(t)\rangle = \sum_\beta \sum_i U^*_{\alpha i} e^{-iE_i t} U_{\beta i}|\nu_\beta\rangle. \tag{1.10}$$

The amplitude of a transition of a neutrino in flavor state α to flavor state β is given by

$$A_{\nu_\alpha \to \nu_\beta} \equiv \langle \nu_\beta|\nu_\alpha(t)\rangle = \sum_i U^*_{\alpha i} U_{\beta i} e^{-iE_i t}. \tag{1.11}$$

The probability for this transition to occur is given by the square of the amplitude

$$P_{\nu_\alpha \to \nu_\beta} = \mid A_{\nu_\alpha \to \nu_\beta} \mid^2 = \sum_{i,j} U^*_{\alpha i} U_{\beta i} U_{\alpha j} U^*_{\beta j} e^{-i(E_i - E_j)t}. \tag{1.12}$$

Since the neutrino mass is so small, all neutrinos are ultrarelativistic and we can approximate Equation 1.6 by

$$E_i \approx p_i + \frac{m_i^2}{2p}. \tag{1.13}$$

Thus the energy difference of neutrino mass eigenstates is given by the mass squared differences

$$E_i - E_j \approx \frac{m_i^2 - m_j^2}{2p} = \frac{\Delta m_{ij}^2}{2p}, \tag{1.14}$$

where it has been assumed that the neutrino mass states have equivalent momenta. In the relativistic regime we can approximate the momentum as being equal to the energy, and the time of propagation, t, as being equal to the distance propagated, L. Thus the probability of oscillation becomes

$$P_{\nu_\alpha \to \nu_\beta} = \sum_{i,j} U^*_{\alpha i} U_{\beta i} U_{\alpha j} U^*_{\beta j} exp(-i \frac{\Delta m_{ij}^2 L}{2E}). \tag{1.15}$$

Through algebraic manipulation and using the properties of unitary matrices, Equation 1.15 can be rewritten as

$$\begin{aligned} P_{\nu_\alpha \to \nu_\beta} &= \delta_{\alpha\beta} \\ &\quad -4 \sum_{i>j} \mathrm{Re}\, U^*_{\alpha i} U_{\beta i} U_{\alpha j} U^*_{\beta j} \sin^2(\frac{\Delta m_{ij}^2 L}{4E}) \\ &\quad +2 \sum_{i>j} \mathrm{Im}[U^*_{\alpha i} U_{\beta i} U_{\alpha j} U^*_{\beta j}] \sin(\frac{\Delta m_{ij}^2 L}{2E}). \end{aligned} \tag{1.16}$$

From Equation 1.16 it is clear that observation of oscillation of neutrino flavor eigenstates would imply a non-zero neutrino mass since otherwise the values of Δm^2 would then be zero.

For 3 neutrino generations, the PMNS matrix is a 3-by-3 unitary matrix. It can be parameterized by 3 real parameters, called the mixing angles, and 1 complex phase. The matrix is commonly represented as a product of three matrices

$$U = \begin{pmatrix} 1 & 0 & 0 \\ 0 & c_{23} & s_{23} \\ 0 & -s_{23} & c_{23} \end{pmatrix} \begin{pmatrix} c_{13} & 0 & s_{13}e^{-i\delta} \\ 0 & 1 & 0 \\ -s_{13}e^{i\delta} & 0 & c_{13} \end{pmatrix} \begin{pmatrix} c_{12} & s_{12} & 0 \\ -s_{12} & c_{12} & 0 \\ 0 & 0 & 1 \end{pmatrix} \quad (1.17)$$

where $c_{ij}\,(s_{ij}) = \cos\theta_{ij}(\sin\theta_{ij})$ and δ is the CP violating phase.

1.3.2 Neutrino Mass Heirarchy

One of the current unknowns in neutrino physics is the relative sizes of the neutrino masses, the neutrino mass heirarchy. From experiments that observe neutrinos from the sun, it is known that $m_1 < m_2$. However, much of the information about the relative sizes of m_2 and m_3 comes from experiments that measure the ν_μ produced in the atmosphere where the survival probability is

$$P_{\mu\mu} \approx 1 - \sin^2(2\theta_{13})\sin^2(\frac{\Delta m^2_{13}L}{4E}). \quad (1.18)$$

It is clear from this equation that the survival probability is not sensitive to the sign of Δm^2_{13}. To measure this value, it is necessary to look to the subleading terms in the survival probability, something that the current experiments are not capable of doing. The two possibilities of the neutrino mass heirarchy are the normal heirarchy, where $m_1 < m_2 < m_3$ and the inverted heirarchy, where $m_3 < m_1 < m_2$.

1.3.3 Results from Neutrino Oscillation Experiments

In 1998, the Super-Kamiokande collaboration announced the first experimental observation of neutrino oscillation in atmospheric neutrinos [16]. Since then, experiments have measured or set limits on most of the parameters that make up the PMNS matrix.

Neutrino oscillation experiments can be classified according to the types of neutrinos being observed and the experimental apparatus used to observe them. The 4 classes of experiments are atmospheric, solar, reactor and accelerator neutrino experiments.

Atmospheric neutrino experiments are experiments that study the neutrinos produced in earth's atmosphere. Cosmic rays approaching the earth collide with nuclei in the atmosphere, producing a shower of hadronic particles, mainly pions. These pions decay into muons and ν_μs, with the muons subsequently decaying into ν_μs. Because these experiments primarily study muon neutrinos, the parameters they are sensitive to are represented by the left and middle matrices in Equation 1.17. These experiments in particular

provide a good measurement of the survival probability of muon neutrinos, thereby measuring θ_{23} and Δm^2_{23}.

Accelerator neutrino experiments measure beams of muon neutrinos produced by particle accelerators. The T2K Experiment is an example of an accelerator experiment. Because the neutrinos from the atmosphere and accelerators both consist primarily of muon neutrinos, these experiments measure the same neutrino oscillation parameters. The values of these parameters have recently been measured by the MINOS experiment. They find $\Delta m^2_{23} = 2.32^{+0.12}_{-0.08} \times 10^{-3}\ eV^2$, $\sin^2 2\theta_{23} > 0.90$ at 90%CL [17] and $2\sin^2\theta_{23}\sin^2 2\theta_{13} = 0.041^{+0.047}_{-0.031}(0.079^{+0.071}_{-0.053})$ for a normal(inverted) neutrino mass hierarchy [18].

Solar neutrino experiments measure electron neutrinos produced in the fusion reactions in the sun's core. These experiments typically measure the survival probability of electron neutrinos and therefore provide measurements of the θ_{12} and Δm^2_{12} parameters. Super-Kamiokande and SNO are examples of solar neutrino experiments.

Reactor neutrino experiments measure anti-electron neutrinos produced in man-made nuclear reactors. These experiments provide complementary measurements of the solar and accelerator parameters since the survival probability of these neutrinos has terms that depend on θ_{12} and Δm^2_{12} in addition to the θ_{13} and Δm^2_{13} parameters. Examples of reactor neutrino experiments include the KamLAND, CHOOZ, and Daya Bay experiments.

1.4 Overview of the T2K Neutrino Oscillation Experiment

The Tokai-to-Kamioka (T2K) experiment is a long-baseline neutrino oscillation experiment located in Japan. In Tokai, Japan, a beam of mostly pure muon neutrinos is produced at the Japanese Proton Accelerator Research Complex (J-PARC). At 280m from the neutrino beam origin, a suite of near detectors measures the properties of the neutrino beam prior to oscillation. The neutrinos traverse 295km to Kamioka, Japan, where they are detected by the Super-Kamiokande 50 kiloton water Cherenkov detector. Figure 1.2 shows a horizontal view of the T2K baseline.

T2K aims to measure the appearance of electron neutrinos from the beam of muon neutrinos. According to Equation 1.16 the probability for this transition to occur is

$$P_{\nu_\alpha \to \nu_\beta} \approx \sin^2\theta_{23}\sin^2 2\theta_{13}\sin^2(\frac{\Delta m^2_{32}L}{4E_\nu}) \tag{1.19}$$

with additional terms providing negligible contributions. With a baseline of 295 kilometers, the first oscillation maximum corresponds to a neutrino energy of 0.6 GeV. To enhance the selection of neutrinos with this energy, T2K uses

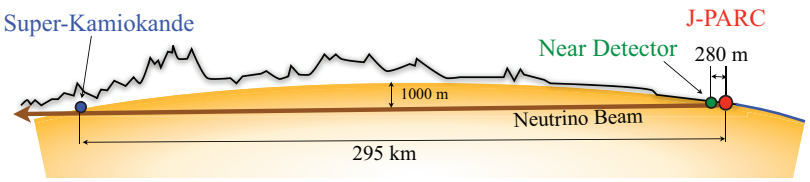

Figure 1.2: Horizontal view of the T2K experiment baseline

an off-axis beam configuration which exploits the kinematics of pion decay to produce a narrow-band beam.

In addition to the primary goal of measuring electron neutrino appearance, T2K will also measure the atmospheric parameters θ_{23} and Δm^2_{32} to a higher precision than previous experiments due to its high-intensity beam. T2K will also provide measurements of neutrino interaction cross sections, one of which is the subject of this dissertation.

1.5 Motivation for the NC1π^0 Measurement

T2K measures electron neutrino events via the charged current quasi-elastic interaction:

$$\nu_e + n \rightarrow e^- + p. \tag{1.20}$$

The experimental signature for this interaction is the observation of a single electron as the proton is usually too low in energy to be detected. At the Super-Kamiokande detector, neutrino interactions occur on water and the scattered particles are detected via the Cherenkov radiation produced as they propagate through the detector. Super-Kamiokande is able to distinguish μ-like particles from e-like particles by the pattern of hits produced by the Cherenkov radiation. Figure 1.3 shows event displays for the two different particle hypotheses.

When a neutral pion (π^0) is produced, it typically decays into two photons, with each photon producing its own electromagnetic shower and therefore producing e-like rings. In situations where one of the photons from the π^0-decay is not properly reconstructed, these π^0 events will mimic the experimental signature of electron neutrino appearance. This typically occurs in instances where the opening angle between the two gammas is very small or where, due to an asymmetric decay, one of the decay photons is too low in energy to be reconstructed. This is shown in Figure 1.4, which has been

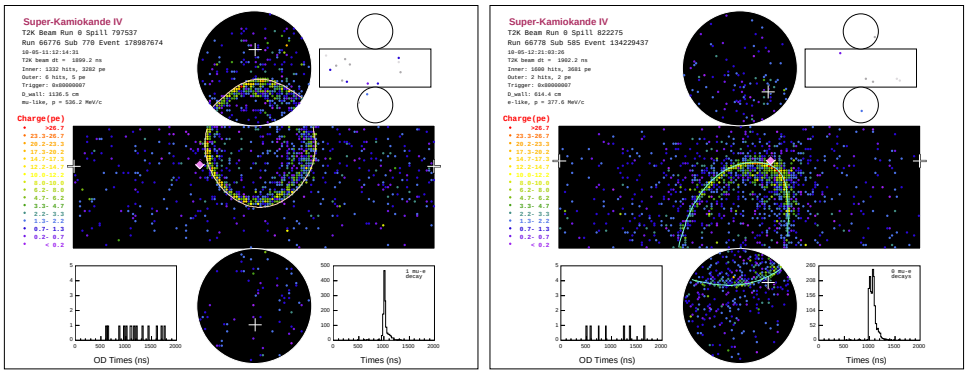

Figure 1.3: Super-Kamiokande event displays. Left: Muon-like event. Right: Electron-like event.

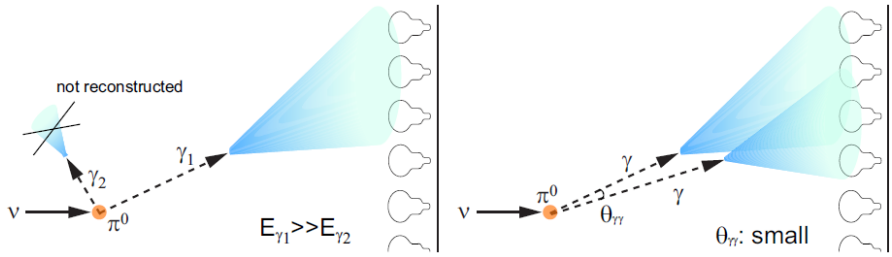

(a) Highly asymmetric energy decay (b) Small opening angle

Figure 1.4: Typical scenarios where a π^0 event can mimic a ν_e signal event

reprinted from another thesis [19].

Figure 1.5 shows the reconstructed energy of the events that make up the background in the T2K ν_e oscillation analysis. Along with the intrinsic ν_e-contamination in the beam, π^0 events are expected to make up the dominant contribution to the background of the ν_e appearance search. Therefore it is crucial to have a measurement of the NC1π^0 production cross section on water so that the π^0 background can be accurately prediced at Super-Kamiokande. To that effect, the T2K experiment has constructed a π^0-detector designed to measure that reaction as a part of its near detector facility. The detector consists of active tracking layers as well as layers of water targets that may be filled and emptied. The detector will make two measurements of the NC1π^0 interaction rate, one with the detector filled with water, and one with the detector drained. A subtraction of the relative rates will then yield the cross section on water. This dissertation will describe in detail a measurement of the NC1π^0 production cross section performed while the T2K π^0 detector was filled with water.

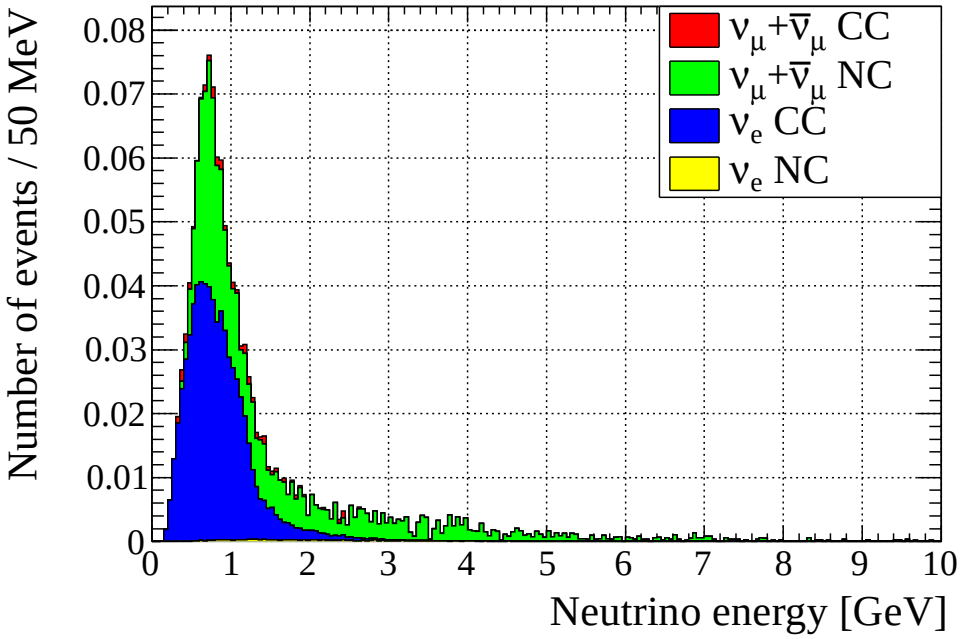

Figure 1.5: The predicted energy spectrum of the beam background events for the ν_e oscillation analysis at Super-Kamiokande

Chapter 2

The T2K Experiment

The T2K experiment is a long-baseline neutrino oscillation experiment that aims to measure electron neutrino appearance from a beam of muon neutrinos, therefore providing a measurement of θ_{13}, the last unknown neutrino mixing angle. An overview of the experiment was given in Chapter 1. In this chapter we will give a summary of the experimental components, including the neutrino beamline, the near detector facility at 280 m and the Super-Kamiokande detector. A fully detailed description is given in recently published documents [20]. We will conclude this chapter by presenting some initial oscillation results.

2.1 J-PARC Accelerators

At the J-PARC facility, protons are accelerated up to 30 GeV by a series of three accelerators, a linear accelerator (LINAC), a rapid-cycling synchrotron (RCS), and a main ring (MR) synchrotron. In the LINAC, a H^- beam is accelerated to 181 MeV. Charge-stripping foils convert the H^- to H^+ at the end of the LINAC and are injected into the RCS. In the RCS, the proton beam

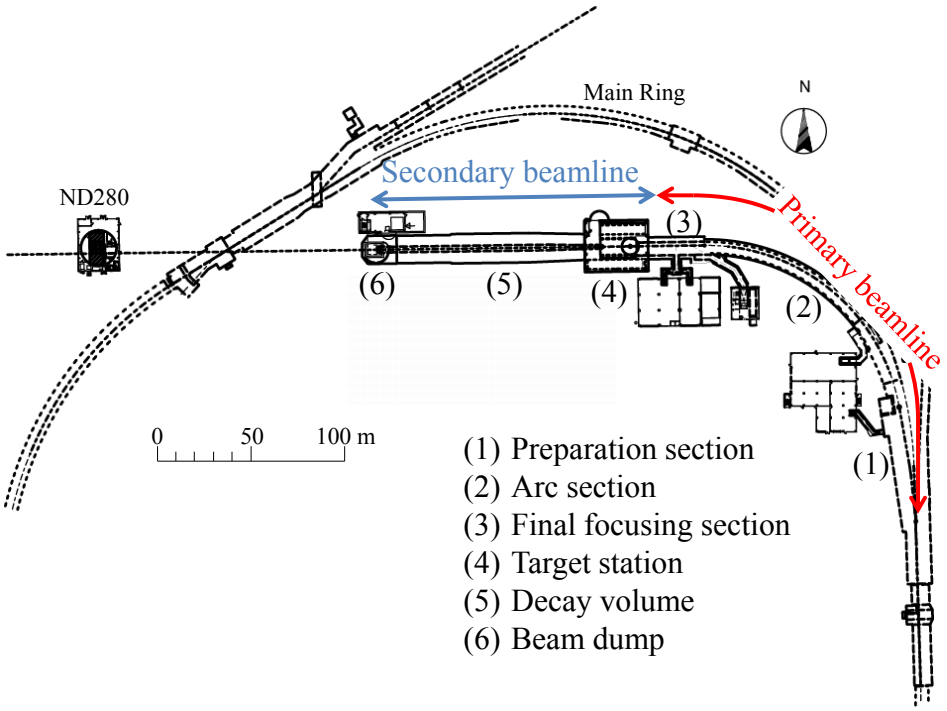

Figure 2.1: Overview of the T2K neutrino beamline.

is accelerated up to 3 GeV in 2 bunches on a 25 Hz cycle. From there the protons are dispensed to various experimental facilities within J-PARC. Five percent of the proton bunches are distributed to the MR where the protons are finally accelerated up to 30 GeV in bunches of 8 (6 prior to a summer 2010 upgrade). To produce the T2K neutrino beam, proton bunches are extracted in a single turn by a series of 5 kicker magnets.

2.2 T2K Neutrino Beamline

The neutrino beamline is composed of two sections, termed the primary and secondary beamlines, and is shown in Figure 2.1. In the primary beamline, the proton beam is extracted from the MR in a single turn and bent in the direction towards Super-Kamiokande. In the secondary beamline, the proton beam impacts a graphite target, producing secondary particles consisting primarily of charged pions and kaons. Just downstream from the target, a series of magnetic horns provide focusing of the charged particles in the forward direction. The particles then travel along a decay volume where they decay, producing mostly muons and muon neutrinos. Because of the presence of muons and kaons, there is a small component of electron neutrinos in the beam from the decay of these particles. The electron neutrino contamination

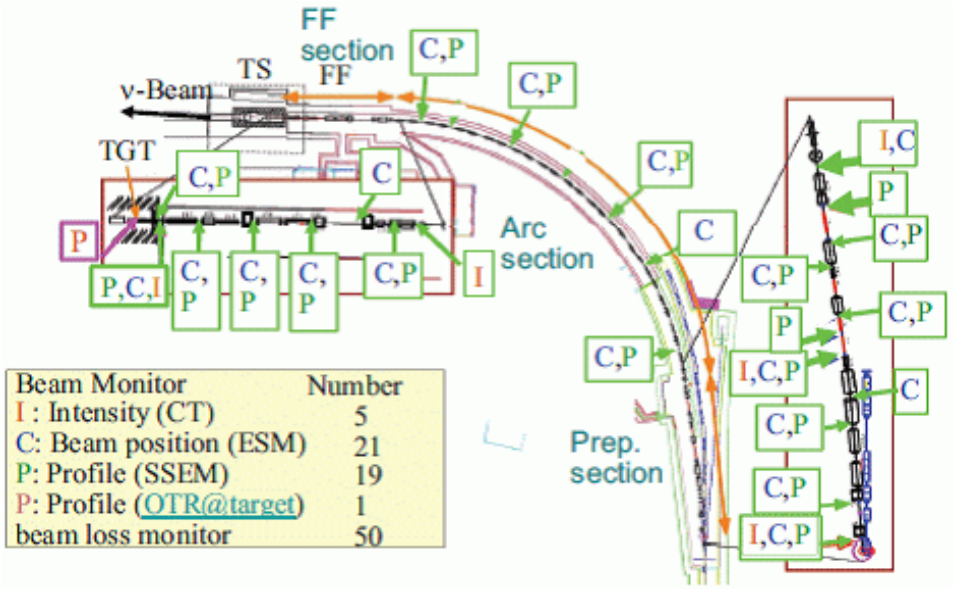

Figure 2.2: Overview of the primary beamline and the beamline monitors.

in the beam is estimated to be ∼1%. At the end of the decay volume is a beam dump which absorbs most of the remaining undecayed particles. Just downstream from the beam dump sits a muon monitor that monitors the direction of the beam by observing the direction of high-energy muons traversing the dump.

2.2.1 Primary Beamline

The primary beamline is comprised of three sections: the preparation section, the arc section, and final focusing section. In the preparation section, the proton beam is prepared for the arc section by a series of 11 normal conducting magnets. In the arc section, the proton beam is bent in the general direction towards the Super-Kamiokande detector. To make the extreme change in direction, approximately 80.7° at a radius of 104 m in curvature, a set of 14 pairs of superconducting combined function magnets and 3 pairs of superconducting magnets provide the necessary steering. In the final section, the focusing section, a set of 10 normal conducting magnets provide the steering and focusing of the proton beam downward at an angle of 3.637° and into the target.

The precise monitoring of the proton beam in the primary beamline is crucial for stable neutrino production. As a result, the primary beamline is instrumented with 5 current transformers (CTs), 21 electrostatic monitors (ESMs), 19 segmented secondary emission monitors (SSEMs), and 50 beam loss monitors (BLMs) designed to measure the intensity, position, profile, and

beam loss, respectively. The primary beamline, along with the positions of the beamline monitors, are shown in Figure 2.2.

The proton beam intensity is measured by 5 CTs. The CTs consist of a toroidal coil wrapped around a ferromagnetic core. Protons passing through the CT induce a current in the coil, and from that, the intensity of the proton beam can be measured. The CT can measure the absolute proton beam intensity to within 2% and the timing of the beam to within 10 ns.

The proton beam position is measured by the 21 ESMs. The ESMs consist of 4 cylindrical electrodes that surround the proton beam. As the proton beam passes through the ESM, a current is induced on each of the electrodes. By measuring the up-down and left-right asymmetry of the induced current, the central position of the beam can be determined.

The proton beam profile is measured by the 19 SSEMs. The SSEM has two thin titanium foils stripped horizontally and vertically sandwiching an anode HV foil. The strips are hit by the proton beam and emit secondary electrons in proportion to the number of protons that go through the strip. The electrons drift along the electric field and induce currents on the strips. The proton beam profile is reconstructed from the resulting charge distribution.

Unlike the ESMs and CTs, which measure the beam non-destructively, the SSEMs cause beam loss of roughly 0.005%. As a result they are remotely inserted into the beam orbit only during beam tuning, and then extracted from the beam orbit during continuous beam operation.

2.2.2 Secondary Beamline

Proton Beam Target

The proton beam target is housed in the target station. It consists of the baffle, optical transition radiation monitor, target, and horns, all located inside a helium vessel.

The proton beam target is a graphite rod 91.4 cm long and 2.6 cm in diameter. Graphite was deliberately chosen because a material with a significantly greater density would melt due to the high beam power. The target is surrounded by a 2 mm thick graphite tube and sealed in a titanium supporting case. The target is cooled by helium gas flowing through the gaps between the core and the tube and case. The target is located entirely within the first magnetic horn, shown in Figure 2.3

Magnetic Horns

The T2K beamline uses three magnetic horns. Each horn is a set of two aluminum coaxial conductors enclosing an empty volume. A pulsed current applied to the horn conductor generates a toroidal magnetic field in the volume of the horn. The field varies as $1/r$, where r is the distance from the horn

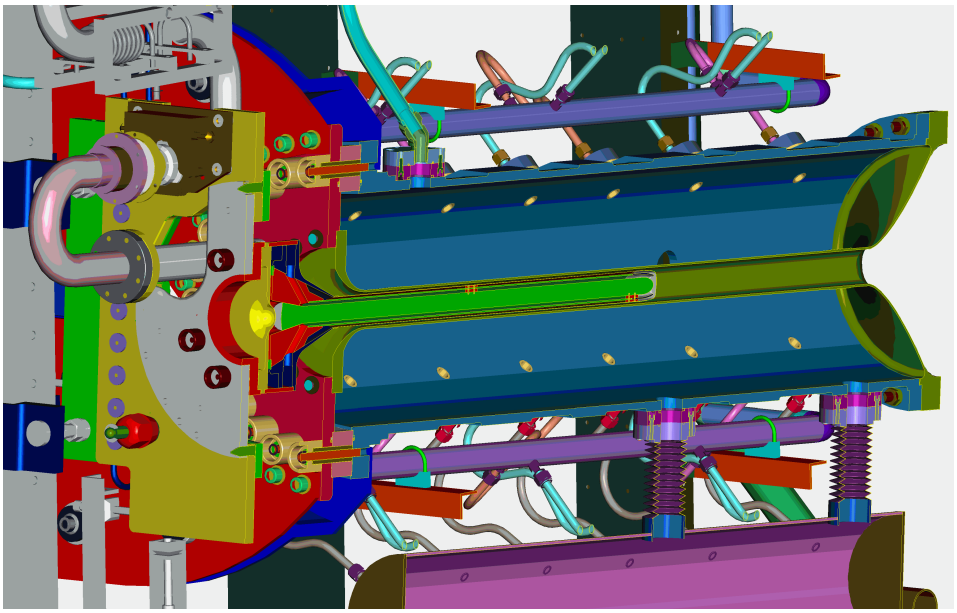

Figure 2.3: The T2K beam target and magnetic horn

axis, and acts to focus the charged pions produced in the target. The first horn encloses the target itself, and focuses the pions initially produced in the target interactions. The second and third horns provide further focusing of the charged pions. When the horns operate at their nominal current, the flux of neutrinos at Super-Kamiokande is increased by a factor of 16 at the peak neutrino energy compared to the case without any horns.

Decay Volume and Beam Dump

The decay volume is a 96 m long steel tunnel. It is 1.4 m wide and 1.7 m high at the upstream end and flares out to 3.0 m wide and 5.0 m high at the downstream end. The purpose of the decay volume is to allow the pions to decay in flight, producing neutrinos. The decay volume is filled with helium gas to reduce secondary interactions of the pions before they can decay.

At the end of the decay volume sits the beam dump. The beam dump consists of a 75 ton block of graphite at its core. This core is enclosed within a helium vessel. Surrounding the helium vessel are a series of iron plates, for a total iron thickness of 2.4 m. The purpose of the beam dump is to stop any pions and muons that fail to decay in the volume. Only muons with an energy of 5.0 GeV or greater are able to make it through the beam dump and into the downstream muon monitor.

Muon Monitor

Since the energy of the neutrinos produced in pion decay depends on the angle with respect to the pion momentum axis, the monitoring of the 0° direction is necessary to verify that the peak neutrino energy remains constant. In addition, the monitoring of the neutrino beam intensity is crucial for stable neutrino production. The neutrino beam intensity and direction can be monitored on a bunch-by-bunch basis by measuring the distribution profile of muons since the muons are mainly produced along with neutrinos from the pion two-body decay. The neutrino beam direction is determined to be the direction from the target to the center of the muon profile. The muon monitor is located just behind the beam dump and is designed to measure the neutrino beam direction with a precision better than 0.25 mrad, which corresponds to a 3 cm precision of the muon profile center. It is also required to monitor the stability of the neutrino beam intensity with a precision better than 3%. More details on the muon monitor can be found in a separate publication [21].

2.3 Near Detectors

At 280 m from the neutrino beam target, a set of detectors has been constructed with the purpose of measuring the neutrino energy spectrum, flavor content, and rates of various interaction modes of the neutrino beam prior to oscillation. This information is then used to predict the neutrino interactions at Super-Kamiokande. There are two detectors at the near detector facility. The first is a detector located on-axis as defined by the initial proton beam. The second is a detector located along the direction towards Super-Kamiokande, 2.5° off of the proton beam axis.

2.3.1 INGRID On-axis Detector

The Interactive Neutrino GRID (INGRID) is the on-axis near detector. It is composed of 14 modules arranged in a cross-like pattern. The modules span a transverse section of 10 m × 10 m, which represents the $\pm 1\sigma$ spatial width of the neutrino beam at 280 m from the target. Two additional modules are placed at positions offset from the main cross with the purpose of measuring the axial symmetry of the neutrino beam. Figure 2.4 shows the arrangment of the 16 INGRID modules looking in the downstream direction.

Each INGRID module is composed of a sandwich structure of 9 iron planes, which provide the target mass for neutrino interactions, and 11 scintillator planes, which provide the tracking. Surrounding each module in the x and y dimension is a layer of scintillator that acts as a veto to particles entering the module. Neutrino interactions are therefore selected by requiring the

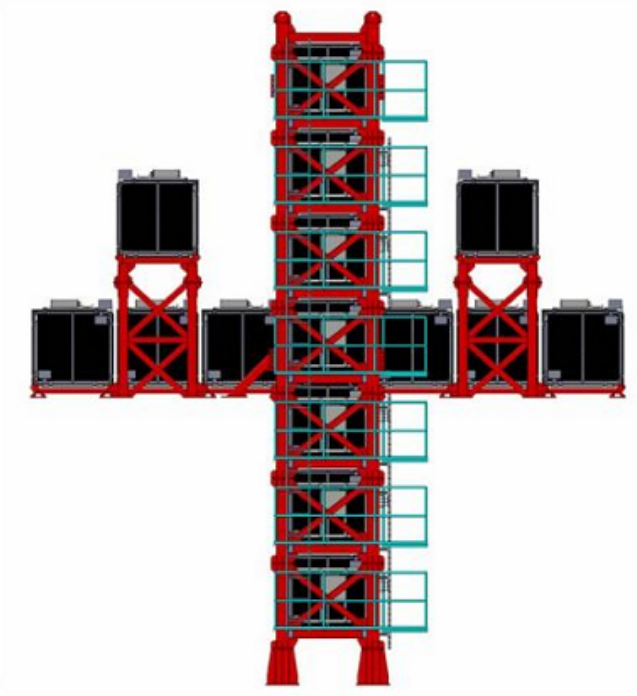

Figure 2.4: INGRID on-axis detector

starting points of the track to be within the surrounding scintillator planes. Figure 2.5 shows a diagram of an INGRID module.

The purpose of the INGRID detector is to provide daily monitoring of the neutrino beam direction and intensity, complementary to the measurements provided by the muon monitor. INGRID measures the direction and intensity of the neutrinos produced from pion parents with a phase space similar to the rest of T2K whereas the muon monitor measures the direction from high-energy pions only. Over the course of T2K running, INGRID has measured the neutrino beam direction to better than 0.4 mrad, and the beam intensity with 4% precision. More detailed descriptions of the INGRID detector and the measurements of the beam direction and intensity can be found elsewhere [20, 22].

2.3.2 Off-axis Detector

The off-axis detector intends to measure the neutrino flux and energy spectrum of neutrinos prior to oscillation. In addition, it will measure the intrinsic ν_e contamination in the beam as well as various neutrino cross sections that make up the backgrounds of the oscillation analyses. The off-axis detector itself consists of a set of detectors: a π^0 detector (PØD) that intends to measure

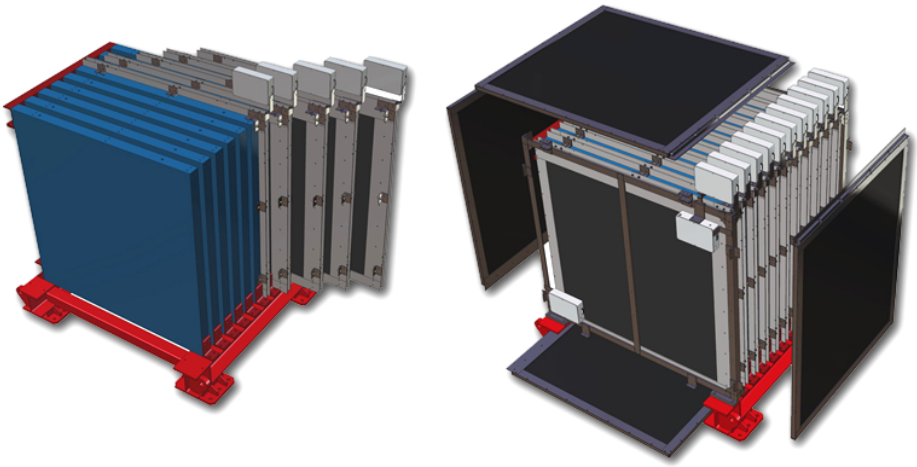

Figure 2.5: An INGRID module. Left: The scintillator tracking planes (blue) and iron target planes. Right: The scintillator veto planes surrounding the module.

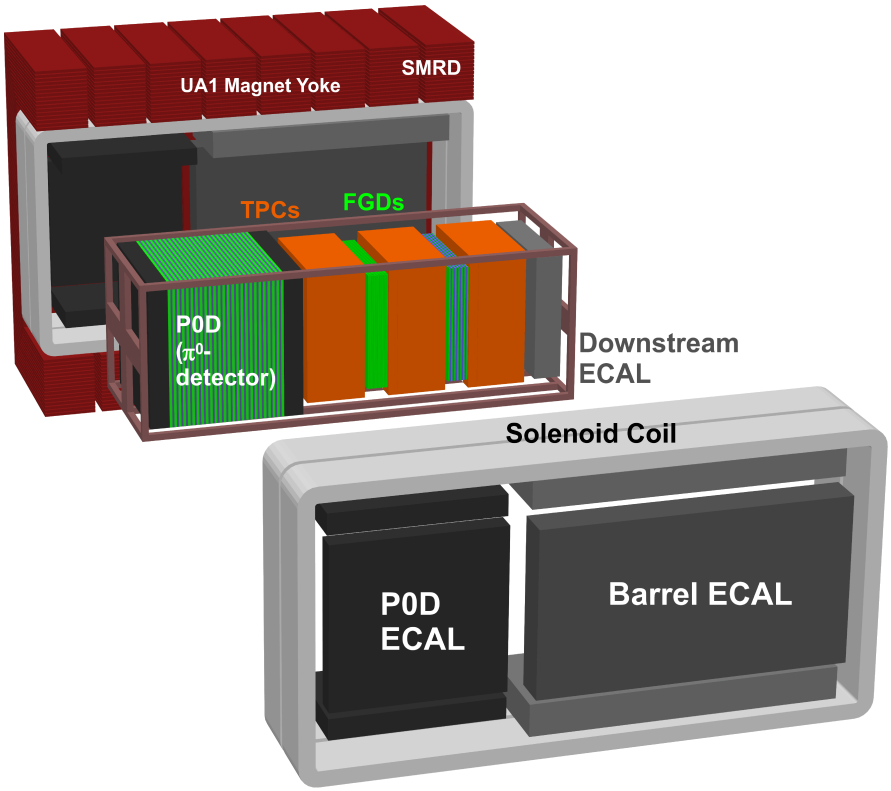

Figure 2.6: ND280 off-axis detector

the NC1π^0 cross section, a tracking detector consisting of time projection chambers (TPCs) and fine-grained detectors (FGDs) that intend to measure the intrinsic ν_e component of the beam along with other neutrino cross sections, and an electromagnetic calorimeter that surrounds the PØD-Tracker system, providing coverage for particles exiting the inner detectors. These detectors are housed in the recycled CERN UA1/NOMAD magnet so as to provide a magnetic field for the tracking detectors. A side-muon range detector (SMRD) has been placed in the magnet yokes to detect muons exiting at large angles from the inner detectors.

UA1 Magnet

The recycled UA1/NOMAD magnet from CERN is used to produce the magnetic field used to measure the momentum and sign of charged particles. The magnet consists of a set of aluminum coils that produce a horizontal dipole field of 0.2 T and a return yoke. The outer dimensions of the magnet system is 7.6 m $\times$ 5.6 m $\times$ 6.1 m. The combined weight of the 16 iron yokes is 850 tons. The yoke system sits on rails, allowing it to be closed when maintenance of the inner detectors is required.

SMRD

The SMRD consists of a total of 440 scintillator modules. Each module consists of an extruded polystyrene scintillator counter. Each counter has an s-shape groove machined in it, allowing the insertion of a wavelength-shifting fiber. The fiber is attached, via an optical connecter, to a multi-pixel photon counter (MPPC) that detects the light coming along the fiber. The scintillator modules are inserted into the 1.7 cm gaps in the magnetic yokes. The scintillator modules are layered 3 or more, depending on in which of the 16 yokes they are placed. The primary purpose of the SMRD is to measure the momentum and angle of muons escaping the inner detectors. In addition, it provides a trigger on cosmic ray muons entering the inner detector and a way to identify beam neutrino interactions in the magnet and surrounding earth.

PØD

The PØD will be explained in detail in Chapter 3.

Time Projection Chambers

The TPCs serves a variety of functions in the near detector. First, with their excellent tracking ability, in particular the ability to determine the number and direction of particle traversing the detector, they provide a means for selecting high-purity samples of various types of neutrino interactions. In

addition, by observing the bending due to the magnetic field, they provide a means of accurately measuring the momentum of charged particles, which is crucial for measuring the energy spectrum of neutrinos prior to oscillation. Lastly, the TPCs have an excellent ability to identify the types of particles passing through the detector by measuring the ionization due to the particle. Each TPC consists of an inner and outer box. The inner box is subdivided by a central cathode. The walls of the inner box are covered with a series of copper strips, which together with the cathode act to produce a uniform electric field perpendicular to the plane of the cathode. The inner box is filled with an argon-based gas. Charged particles traversing through the inner box ionize the gas, producing electrons that drift towards the ends of the TPC where they are readout by bulk micromegas. The outer box contains the inner box and is filled with CO_2 as an insulator. A more detailed description of the TPC components can be found elsewhere [23]. There are three TPCs total. Placed in between them are two fine-grained detectors.

Fine-Grained Detector

The fine-grained detector provides the target mass for neutrino interactions in the tracker. The FGD is composed of extruded polystyrene scintillator bars oriented in the x and y directions, perpendicular to the beam. Within each bar is a hole where a wavelength-shifting fiber is placed. At one end of the fiber is a reflective coating. The other end of the fiber is attached to an MPPC where the light from the fiber is converted to an electrical signal and read out by the electronics. There are two FGDs in total, each with dimensions of 2300 mm $\times$ 2400 mm $\times$ 365 mm in x, y and z, respectively. The first FGD consists purely of scintillator bars, 5760 total, arranged into 30 layers with alternating x or y orientation. The second FGD contains 7 xy scintillator modules along with 6 modules of water 2.5 cm in thickness. A comparison of the rates of neutrino interactions between the two FGD allows one to determine the cross sections on water, which is necessary to apply the near detector measurements to Super-Kamiokande.

Electromagnetic Calorimeter

Surrounding the PØD, TPC, and FGD detectors is an electromagnetic calorimeter (ECal). The ECal is made up of 13 modules: 6 Barrel-ECal modules surrounding the TPC and FGD parallel to the beam direction, 1 downstream ECal module providing coverage of the Tracker in the downstream direction, and 6 PØD-ECal modules surrounding the PØD parallel to the beam direction. Each ECal module is made up of layers of scintillator bars and lead absorber. The purpose of the ECal is to provide coverage of the inner detectors, aiding the reconstruction of π^0 events.

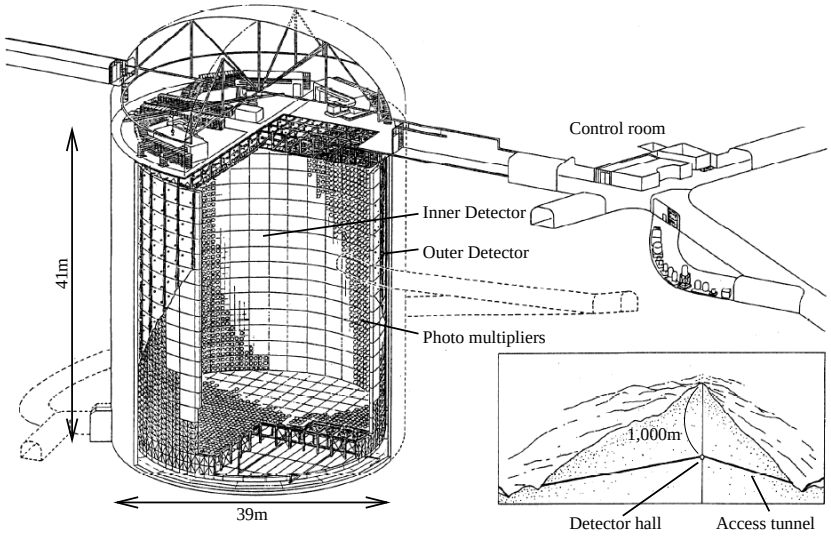

Figure 2.7: Diagram of the Super-Kamiokande detector.

2.4 Far Detector: Super-Kamiokande

The water Cherenkov detector, Super-Kamiokande, serves as the far detector in the T2K experiment. The detector is situated 295 km west of the neutrino beam origin at a depth of 1 km in Mt. Ikenoyama. Super-Kamiokande is a cylindrical cavern containing 50 kilotons of ultra-pure water. The detector consists of two separate volumes, an inner detector and outer detector. The inner detector (ID) is a cylindrical volume 33.8 m in diameter and 36.2 m in height. Inside the ID are 11,129 inward-facing 50 cm diameter photomultiplier tubes. Enclosing the ID is the outer detector (OD). The OD is concentric with the ID, and extends an additional 2 m radially from the ID boundary. Inside the OD are 1,885 outward-facing 20 cm photomultiplier tubes. The boundary of the two volumes is marked by a steel structure that supports the PMTs. The steel structure is covered by layers of black plastic which acts to optically separate the two regions, with the OD acting as a veto region used to reject events where a particle enters from outside the detector. Charged particles from neutrino interactions produce Cherenkov rings as they travel through the water. Particles are identified based on the characteristics of the Cherenkov ring imaged by the PMTs. The Super-Kamiokande detector has been in operation since 1996 and is a well-understood and successful detector. A more detailed description of the detector can be found in [24].

2.5 Neutrino Oscillation Results from T2K

The T2K physics results published so far are the results of two data-taking runs: Run I (Jan. 2010 - Jun. 2010), and Run II (Nov. 2010 - Mar. 2011).

2.5.1 Electron Neutrino Appearance

T2K has published results that represent the first indication of $\nu_\mu \rightarrow \nu_e$ appearance [25]. T2K observes 6 e-like events at Super-Kamiokande. In three flavor mixing scenario with the parameters $|\Delta m^2_{23}| = 2.4 \times 10^{-3}$ eV^2, $\sin^2 2\theta_{23} = 1$, and $\sin^2 2\theta_{13} = 0$, the null hypothesis, the expected number of e-like events would be 1.5 ± 0.3. The probability to observe 6 events, assuming the null hypothesis is correct, is 7×10^{-3}, with a significance of 2.5σ. At 90% C.L., T2K observes $0.03(0.04) < \sin^2 2\theta_{13} < 0.28(0.34)$ for the normal(inverted) mass hierarchy.

2.5.2 Muon Neutrino Disappearance

T2K has also reported a measurement of muon neutrino disappearance [26], observing 31 μ-like events with an expectation of 103 ± 14. The measured oscillation parameters are consistent with other experiments.

Chapter 3

The PØD Detector

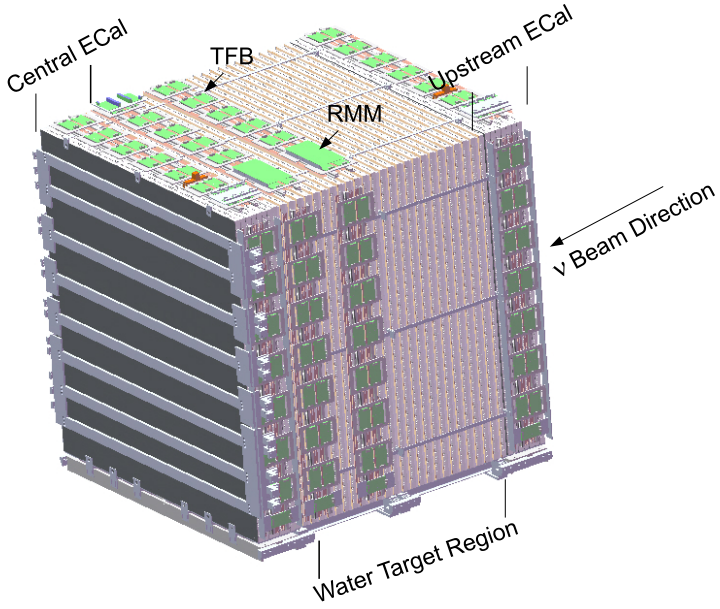

The PØD is a segmented sampling calorimeter optimized for detecting π^0 events. In particular, its primary goal is the measurement of the neutral current single π^0 production cross section, as that constitutes a significant backround to the ν_e-appearance oscillation analysis. The PØD will also provide measurements of the intrinsic ν_e contamination in the beam and other neutrino interaction cross sections. The PØD is constructed in modules. The most basic units, tracking modules called PØDules, are constructed of layers of x and y oriented bars. Combined with the PØDules are layers of absorber and water targets to form larger modules called Super-PØDules. There are 2 types of Super-PØDules: electromagnetic calorimeter (ECal) Super-PØDules consisting of sandwiched layers of PØDules and lead radiators, and water target Super-PØDules consisting of layers of PØDules, brass radiators and water

target layers. This chapter describes the detector components as well as its performance. A more detailed description can be found in a recent publication [27].

3.1 Detector Components

3.1.1 Scintillator Bars and Wavelength-shifting Fibers

The PØD is composed of 10,400 polystyrene scintillator bars that were produced at the extrusion facility at the Fermi National Accelerator Laboratory. Each bar is made of Dow Styron 663 W scintillator base material doped with 1% PPO and 0.03% POPOP. The bars are triangular with a cross section of 17 mm height and 33 mm width. Each bar was produced by co-extruding polystyrene scintillator with a layer of TiO_2, and a 2 mm central hole for the insertion of a wavelength-shifting fiber. The TiO_2 is meant to maximize the internal reflection of light produced by the scintillator, thereby increasing the probability of capture of the light by the fiber. Prior to their assembly into PØDules, the bars are glued into planks by applying a layer of epoxy to each bar and then allowing the plank to cure under vacuum pressure.

A Kurary multi-clad, S-35, J-type, Y-11, 1 mm diameter wavelength-shifting (WLS) fiber is inserted into each hole in the bar. One end of the fiber is diamond polished before a layer of aluminum coating is applied, thus mirroring the fiber. A layer of epoxy is applied to the mirrored end to protect the aluminum coating. The other end of the fiber is glued to a ferrule and is then diamond polished. The ferrule is designed to mount inside an optical connector holding an MPPC.

3.1.2 MPPC

The device that collects the light from the WLS fiber and converts it into an electronic signal is the Hammamatsu Multi-Pixel Photon Counter (MPPC) [28]. This photosensor was chosen because it meets the major requirements of T2K. First, it must be able to operate within the 0.2 T magnetic field. Second, it must be compact enough to fit within the limited space inside the detectors. Third, the large number of overall channels, 10,400 for the PØD and 64,000 overall require that it be low in cost. Lastly it must have a photon detection efficiency equal to or greater than the multi-anode PMT, which was used on other experiments using WLS fiber readout but does not meet the previous requirements. The MPPC has been extensively tested for performance and quality control for its use in the T2K experiment[29].

An MPPC is composed of a number (100 - 1,000) of avalanche photodiodes (APDs) on an area of the order 1 mm $\times$ 1 mm. The APDs operate independently in limited geiger mode with the bias voltage slightly above the

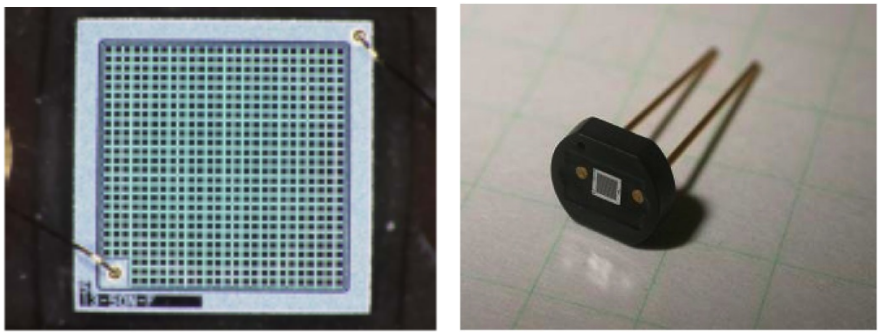

Figure 3.1: Left: Magnified photgraph of the sensitive area of the MPPC. Right: The MPPC in its ceramic housing.

Table 3.1: Main parameters of the T2K MPPCs

Number of pixels	667
Active area	1.3×1.3 mm^2
Pixel size	50×50 μm^2
Operational voltage	$68 - 71$ V
Gain	$\sim 10^6$
Photon detection efficiency at 525 nm	$26 - 30\%$
Dark rate, threshold = 0.5 p.e., T = 25 °C	≤ 1.35 MHz

breakdown voltage. When the light from the WLS fiber is incident on the sensor, it induces a geiger avalanche. The output charge is independant of the number of photoelectrons that were produced within a given pixel and is the same for all pixels. Therefore, the total output charge gives the number of APDs that were discharged and yields the number of photoelectrons. Figure 3.1 shows photographs of the MPPCs used in the T2K experiment. The design specifications are given in Table 3.1.

Prior to their insertion into the PØD, the MPPCs were placed in a custom made optical connector to ensure good alignment and optical contact with the WLS fiber. All 10,400 MPPCs and 1,100 spares underwent quality control to measure their operational characteristics and ensure functionality.

Figure 3.2: A completed PØDule sitting on the gluing table

3.1.3 Electronics

The PØD uses electronics based on the Trip-T ASIC to read out the MPPCs. Up to 64 MPPCs are routed via coaxial cable to a Trip-T front end board (TFB) housing 4 Trip-T ASICs. The TFB integrates the charge in integration cycles that are synchronized with the T2K beam. The TFBs are processed through Readout Merger Modules which provide bi-directional communication between the front end and the data aquisition system. More information on the electronics system can be found elsewhere [30].

3.2 The PØD Module: PØDule

The PØDule provides both the active tracking and basic structural element of the PØD. It is composed of 134 scintillator bars oriented in the x direction and 126 bars oriented in the y direction. The layers of scintillator are glued together with HYSOL epoxy glue. Providing support for the bars are 4 PVC frames which are machined to support either the MPPCs or light injection system. Each frame has precision-aligned holes for their assembly into Super-PØDules. The PØDule is kept light-tight by two sheets of HDPE black plastic. Each PØDule was constructed on a custom made gluing table. When completed the PØDule's outer dimensions are 2212 mm $\times$ 2348 mm $\times$ 38.75 mm. Figure 3.2 shows a finished PØDule just after assembly. A step-by-

Figure 3.3: Left: Lead plates being placed into position. Right: Stainless steel sheets provide support.

step description of the assembly is provided in Appendix A. After assembly the response of each PØDule was measured using a radioactive source placed in an automated scanner. The purpose of the scanning was to measure the position of the bars in the PØDule, the variation of the response as a function of its distance from the sensor, and to check for dead channels.

3.3 Radiators

The purpose of the radiators is to facilitate the conversion of γs into charged particles, usually through pair production, so that they can be detected by the scintillator. In the PØD there are two types of radiators, lead and brass radiators for use in the ECal and water target Super-PØDules, respectively.

3.3.1 Lead Radiators

A lead radiator consists of a 3.45 mm (0.67 X_0) layer of lead sheet. Due to lead's malleability, smaller sized lead plates are inserted one by one to lessen the likelihood of deformities. The lead plates are supported on the outside by 4 aluminum frames, and supported on the front and back by a 0.5 mm stainless steel sheet. All of the components are glued into place using HYSOL epoxy. The aluminum frames contain alignment holes for assembly into Super-PØDules. Figure 3.3 shows a lead radiator during construction.

3.3.2 Brass Radiators

The brass radiators consist of two 1.5 mm (0.1 X_0) thick brass sheets side by side. Because brass is easy to handle, no epoxy is necessary and they

Table 3.2: The mass, dimensions, and depth in radiation lengths for each Super-PØDule.

Super-PØDule	Mass (kg)	Dimensions (mm×mm×mm)	Depth in R.L.
Upstream ECal	2900	2298×2468×305	4.946
Upstream Water Target:		2298×2468×888	
Empty	3600		1.370
Filled	5100		2.379
Central Water Target:		2298×2468×854	
Empty	3500		1.356
Filled	4900		2.287
Central ECal	2900	2298×2468×304	4.946

are simply installed in-situ with the water target Super-PØDule.

3.4 Water Targets

Each water target consists of two water bladders surrounded by 4 HDPE frames. Each water target layer is 28 mm (0.08 X_0) thick. The water targets are instrumented with pressure sensors and several binary wet/dry sensors to monitor the water depth.

3.5 The Super-PØDule

The PØD contains two types of Super-PØDules: the ECal Super-PØDule (ECal), and the water target Super-PØDule (WT). There are two ECals in the PØD, the upstream and central ECals. Each consist of 7 PØDules and 7 lead radiators. There are two WTs in the PØD, the upstream and central water targets. The upstream (central) WT consists of 13 PØDules, 13 (12) water target layers and 13 (12) brass radiators. The dimensions of each Super-PØDule are given in Table 3.2. Figure 3.4 shows a schematic of the PØD and the positioning of each Super-PØDule. Figure 3.5 shows fully assembled ECal and water target Super-PØDules.

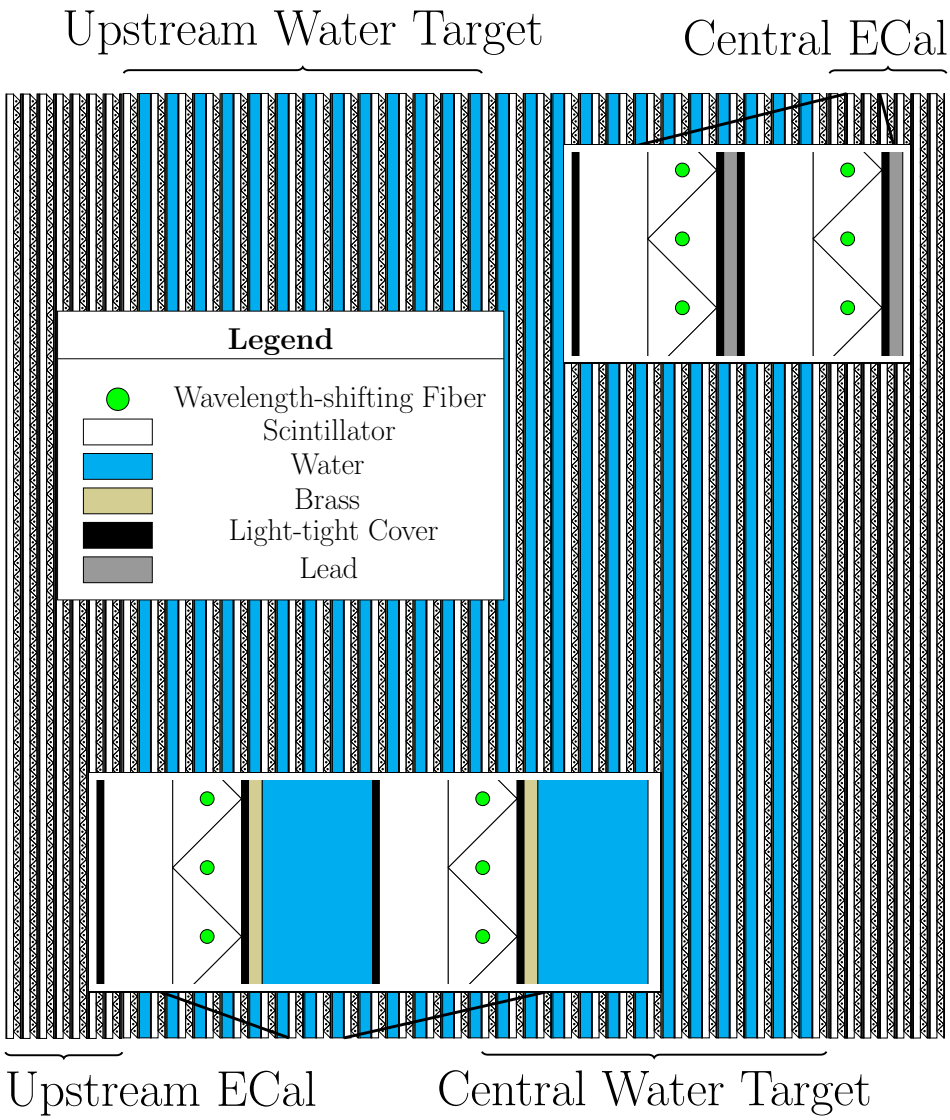

Figure 3.4: A schematic of the four PØD Super-PØDules as installed in the detector. Beam direction: left to right.

Figure 3.5: Completed Super-PØDules. Left: The central water target Super-PØDule. Right: The central ECal Super-PØDule.

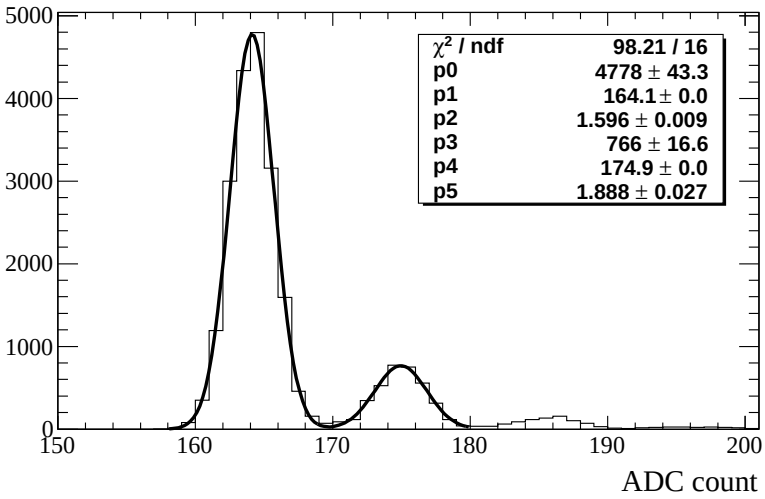

Figure 3.6: Typical digitized dark noise spectrum of an MPPC with a double Gaussian function fitted to the pedestal and 1 p.e. peaks.

3.6 Calibration

3.6.1 Low-level Charge Calibration

The low-level charge calibration converts the electronics signal into the equivalent number of photoelectrons (p.e). It involves the determination of the electronics signal with no input from the MPPCs, i.e. pedestal subtraction, corrections to the MPPC gain, and corrections of non-linearity in the TFB electronics. The pedestal subtraction and MPPC gain corrections are both determined by measuring the electronics response to dark noise. Figure 3.6 shows a typical dark noise spectrum. The dominant peak is the pedestal. Directly to the right of the pedestal is the 1 p.e. peak. The pedestal constant is determined by fitting the dominant peak to a Gaussian distribution. The mean of the Gaussian fit is the value used for the pedestal subtraction. To determine the MPPC gain, the distribution in Figure 3.6 is fitted with a double Gaussian distribution. The separation of the pedestal and 1 p.e. Gaussian means gives the number of p.e. in terms of the ADC response. The last step involves correcting for the non-linearity of the electronics. Each TFB is equipped with a circuit that injects charge into the MPPC readout channels. From there the response of the electronics can be measured for a range of input charge levels. Figure 3.7 shows such a response. The charge vs. ADC value distribution is fit to a bi-cubic polynomial and the fitted parameters are used to correct the raw ADC value during offline calibration. More information on the calibration can be found elsewhere [31].

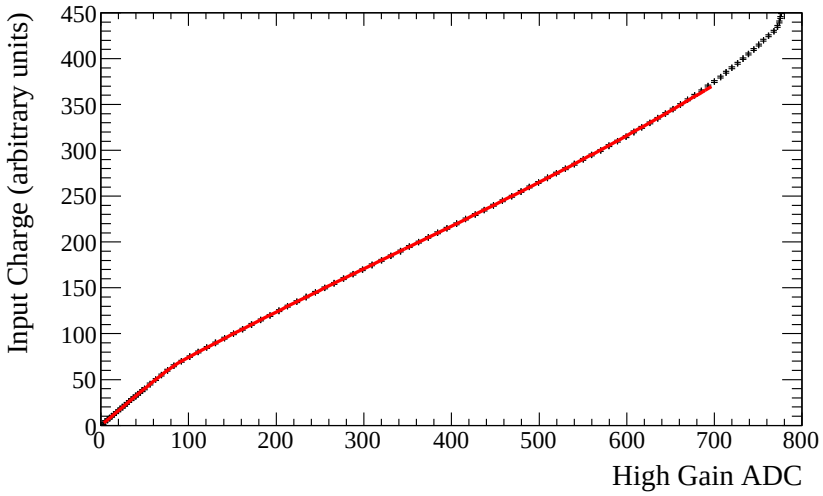

Figure 3.7: Charge versus ADC for a high-gain Trip-T channel fit to a bi-cubic function.

3.6.2 MIP Light Yield

For muons with energies on the order of 0.1 - 100 GeV the amount of energy deposited per unit length is close to a constant, the minimum ionization, with radiative corrections on the order of a few percent at higher energies. These minimum ionizing particles (MIPs) provide a method of measuring the energy response of the scintillator bars when these MIPs pass through the detector. This light yield measurement has been done using cosmic rays [32] as well as muons produced in external neutrino interactions that traverse the detector. Figure 3.8 shows the charge deposited after calibration, path length and attenuation correction, in the scintillator layer for through-going muons. The distribution has been fit to a Gaussian-Landau distribution. The most probable value of the fit is determined to be 37.9 p.e./MIP/cm. This value provides the reference point for the energy response of all PØD channels.

3.6.3 Light Injection System

The purpose of the light injection system (LIS) is to monitor the MPPC response over the range of light levels expected from neutrino interactions. In addition, the LIS provides a method to check for the functionality of all 10,400 PØD channels. The LIS consists of fast pulsed 400 nm UV LEDs that are installed in each PØDule PVC support frame. Dedicated light injection runs are taken periodically to monitor the PØD channels.

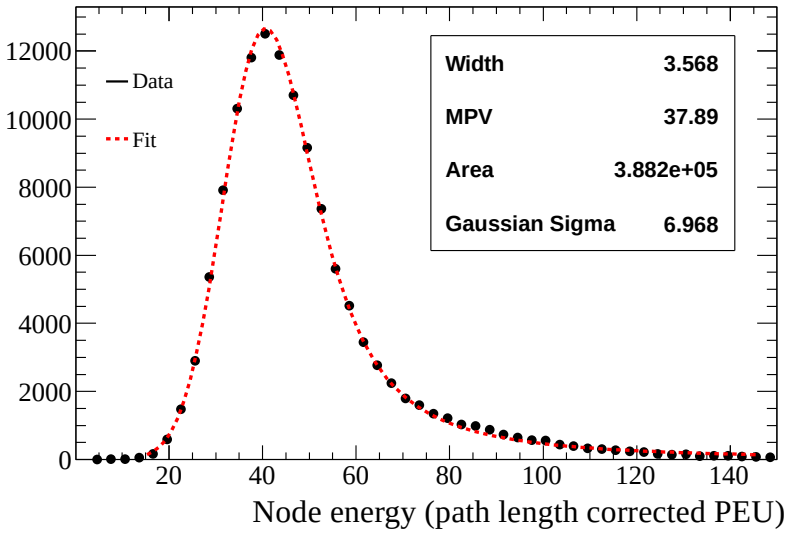

Figure 3.8: The summed charge, in photo electron units (PEU), deposited in a layer of scintillator for through-going muons originating from neutrino interactions outside the detector

3.7 Data Acquisition

The PØD data acquisition (DAQ) is handled by the global ND280 data acquisition which consists of two components: the DAQ and the global slow control. The DAQ collects the data from each detector front-end system and stores it in files. The global slow control collects monitoring information, stored in databases such as temperature and voltages. This information is made available to shift workers via a webpage. Both the DAQ and global slow control are based on the MIDAS framework. [33]

Chapter 4

NC1π^0 Analysis Overview

As discussed in Chapter 1, for the T2K ν_e appearance analysis, it is crucial to have an understanding of NC1π^0 production since it forms one of the largest sources of background to the analysis when NC1π^0 events are misidentified as ν_e signal events at Super Kamiokande. This misidentification occurs when only one ring is detected from the decay photons of the π^0. This can occur when the photons are boosted in the forward direction of the lab frame, resulting in overlapping rings, or in instances of asymmetric decay, where the axis of the decay in the π^0 rest frame is along the momentum axis, leading to a photon in the forward direction producing an observable ring, and a backward photon producing little to no ring.

The definition of NC1π^0 events is characterized by the particles present after final state interactions, and not the primary cross section definition. These interactions will be discussed in Chapter 5. For the purposes of this analysis, we define an NC1π^0 interaction as having no charged leptons, no charged mesons and no uncharged mesons other than a single π^0 leaving the nucleus. We allow any number of protons and neutrons.

This dissertation reports a measurement of the observed number of NC1π^0 events in the data compared to the number predicted by the Monte Carlo simulation. We measure two quantities. The first is the ratio of the observed number of PØD NC1π^0 events in data relative to the number predicted by the simulation

$$r = \frac{N^{Data}_{NC1\pi^0}}{N^{MC}_{NC1\pi^0}}. \tag{4.1}$$

This quantity is equivalent to the ratio of the measured cross section to that predicted by the simulation. Because this has large systematic uncertainties associated with the beam flux, we also report the double ratio of the number of observed NC1π^0 events in the PØD to the number of inclusive charged current (CC inclusive) events in the tracker in data relative to the simulation. By taking the ratio of NC1π^0 to CC inclusive we get cancellation of the beam

flux systematics. However, because of the different detector acceptances for the PØD and tracker, we must take the ratio of the data to the simulation. Mathematically, this double ratio is equivalent to the quantity in Equation 4.1, normalized by the tracker CC inclusive measurement as shown by

$$\begin{aligned} R &= \frac{N^{Data}_{NC1\pi^0}/N^{Data}_{CC}}{N^{MC}_{NC1\pi^0}/N^{MC}_{CC}} \\ &= (\frac{N^{Data}_{NC1\pi^0}}{N^{MC}_{NC\pi^0}})/(\frac{N^{Data}_{CC}}{N^{MC}_{CC}}) \end{aligned} \tag{4.2}$$

The first term in Equation 4.2 is simply Equation 4.1. The second term is equivalent to the inverse of the CC inclusive measurement performed by the ND280 tracker for the ν_e appearance analysis [25, 34]. This value was measured to be

$$\frac{N^{Data}_{CC}}{N^{MC}_{CC}} = 1.036 \pm 0.028(stat.)^{+0.044}_{-0.037}(det.syst) \pm 0.038(phys.syst). \tag{4.3}$$

Equation 4.2 is equivalent to the ratio of the NC1π^0 to CC inclusive cross section as measured by the data relative to the value predicted by the simulation.

To extract the number of events observed in data, we perform an extended likelihood fit of the invariant mass distribution between 0 and 500 MeV/c^2 after all selection cuts have been applied. To perform the likelihood fit, the invariant mass distribution of the simulation is used as the PDF of the likelihood function.

Chapter 5 describes the simulations used to predict the expected number of events and the expected invariant mass distribution. Chapter 6 gives a summary of the data and Monte Carlo samples used in the analysis. Chapter 7 summarizes the reconstruction algorithms used to reconstruct events in the PØD. Chapter 8 summarizes the event selection criteria used to select NC1π^0 events. Chapter 9 details how the number of NC1π^0 events are extracted from the data. Finally, Chapter 10 gives the estimate of the systematic uncertainties for this analysis.

Chapter 5

Simulation

This chapter describes the simulation chain used by this analysis. There are three components to this chain. First, the neutrino beam simulation takes information about the primary proton beam and subsequent hadron production and decay to obtain the expected flux at the near detector. Second, neutrino event generators use the flux information from the beam simulation and the detector geometry model to simulate the neutrino interactions in our detector, with the eventual output being a set of final state particles exiting the nucleus. Lastly, a detector simulation propagates the final state particles through the detector, simulating the energy deposition and trajectory of the particle, any secondary interactions, and the response of the electronics.

5.1 Neutrino Beam Simulation

The T2K neutrino beam simulation (JNUBEAM) is based on the GEANT3 simulation package [35]. JNUBEAM proceeds sequentially with the primary proton beam incident on the graphite target. There, the proton-target interactions are simulated, producing the secondary hadrons. These hadrons are then tracked by JNUBEAM until their simulated decay occurs, producing a neutrino with a given energy and direction. This neutrino is propagated to the near and far detectors resulting in the flux prediction. The flux is tuned using external hadron production data.

5.1.1 Proton Beam and Target Simulation

The proton beam is simulated using the measurements made by the primary proton beam monitors discussed in Chapter 2. Inside the target, secondary hadron production is simulated using the FLUKA [36] hadron production model. The position and momentum information of the exiting secondaries is passed to JNUBEAM.

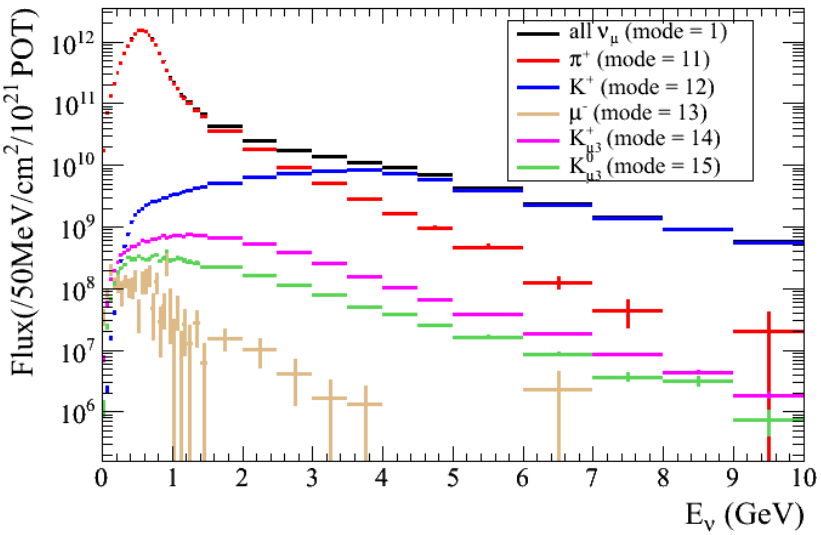

Figure 5.1: The expected flux at ND280 for various neutrino parent particles.

5.1.2 Tracking of Secondary Particles

Secondary particles are tracked using the GEANT package. Interactions of secondary hadrons outside of the target are simulated using the GCALOR hadron production model, with the interaction cross sections tuned to experimental data. The magnetic field due to the horns is implemented according to Ampère's Law. The particles are tracked into the decay volume where they decay and produce neutrinos. For muon neutrinos, JNUBEAM considers the following decay modes with their respective branching ratios:

$$\begin{array}{rcll} \mu^- & \rightarrow & e^- + \nu_\mu + \bar{\nu_e} & (100) \\ \pi^+ & \rightarrow & \mu^+ + \nu_\mu & (100) \\ K^+ & \rightarrow & \mu^+ + \nu_\mu & (63.55) \\ K^+ & \rightarrow & \pi^0 + \mu^+ + \nu_\mu & (3.353) \\ K^0_L & \rightarrow & \pi^- + \mu^+ + \nu_\mu & (27.04) \end{array}$$

Figure 5.1 shows the expected flux at the near detector according to the JNUBEAM 11a flux simulation.

5.1.3 Hadron Production Tuning

Hadron production in the T2K target is tuned using data from the NA61 /SHINE [37] experiment at CERN. The NA61 experiment measures hadrons in T2K's phase space by colliding 30 GeV protons with a replica of T2K's graphite target. The differential cross sections of the charged hadron secondaries in the

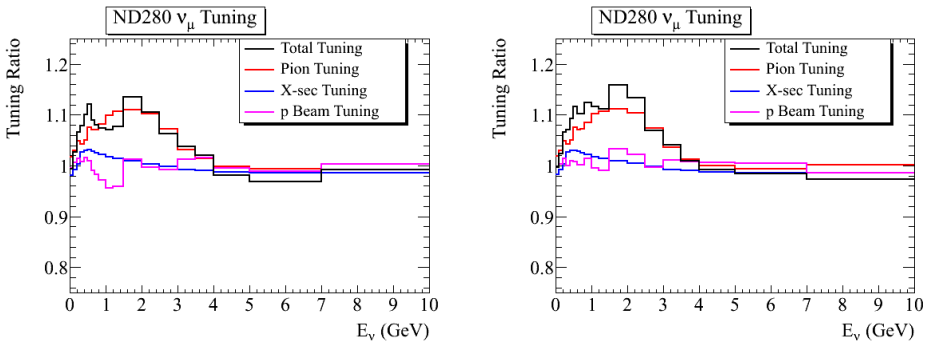

Figure 5.2: Reweighting factors applied to 11a neutrino flux due to 11av1 tuning. Left: Run I. Right: Run II.

p+C interactions are measured as a function of momentum for several angular ranges. The hadron production of the FLUKA simulation is then reweighted so that it reproduces the data.

5.1.4 Neutrino Flux Reweighting

The Monte Carlo files used in this analysis have been produced using the JNUBEAM 11a flux release. This flux simulation is produced using a simplified proton beam centered on the origin of the target, with a spread of 0.42 cm. All horn currents are set to 249.67 kA. The hadrons produced in this simulation are reweighted using smaller files produced with the correct Run I (II) beam parameters. Additional reweighting is applied to the hadron production using NA61 data. This analysis considers two flux reweightings, named 11av1 and 11av2.

11av1 Reweighting

The 11av1 flux tuning uses the same hadron tuning that was used for the T2K ν_e appearance analysis and is based on the data from the NA61 $\pi^{\pm}$ analysis [38, 39]. The production of tertiary hadrons from particles produced in the target is also tuned to the data. Figure 5.2 shows the flux reweighting factors for Run I and Run II.

11av2 Reweighting

The 11av2 reweighting is an update to the 11av1 which incorporates NA61's K^+ data [40]. For K^+ outside of NA61's phase space, as well as K^-'s, an interpolation of external data is used [41, 42].

5.2 Neutrino Interaction Simulation

The T2K experiment uses the NEUT event generator [43] to simulate the neutrino interactions in the detector. NEUT was originally written for use with the Super-Kamiokande experiment and therefore only interactions on water were considered. As a result, NEUT has been adapted for use with T2K and can now simulate interactions on target nuclei other than water. NEUT uses fundamental physics models to predict the interaction rates and kinematics of various neutrino interactions expected in T2K's energy range. Whenever possible, these models are compared with experimental data. The following reactions are simulated in NEUT:

- (Quasi-)Elastic Scattering: $\nu N \rightarrow lN'$
- Single Meson Production: $\nu N \rightarrow lN'm$
- Deep Inelastic Scattering: $\nu N \rightarrow lN'X$
- Coherent Pion Production: $\nu A \rightarrow lA\pi$

where ν is a neutrino, N and N' are nuclei, l is a lepton, m is a meson (π, K, or η), X is a system of hadrons, and A is a nucleus. NEUT also simulates the secondary interactions that take place when the particles pass through the nuclear medium.

5.2.1 (Quasi-)Elastic Scattering

For charged current quasi-elastic scattering, NEUT uses the formalism of Llewelyn-Smith [44] where the hadronic current is parameterized in terms of form factors such that:

$$< N'|J_{had,\lambda}|N >= cos\theta_c \bar{u}(N')[\gamma_\lambda F_V^1(q^2) + \frac{i\sigma_{\lambda\nu}q^\nu \xi F_V^2(q^2)}{2M} + \gamma_\lambda\gamma_5 F_A(q^2)]u(N) \tag{5.1}$$

where θ_c is the Cabibbo angle, F_V^1 and F_V^2 are the vector form factors, $\xi \equiv \mu_p - \mu_n = 3.71$ is the difference between the proton and neutron magnetic moments, M is the nucleon mass, and F_A is the axial form factor. The conserved vector current hypothesis [45] implies that the vector form factors can be written in terms of the Sachs form factors, which are determined from electron scattering data. The axial form factor is parameterized as a dipole:

$$F_A(q^2) = \frac{F_A(q^2 = 0)}{[1 + \frac{q^2}{(M_A^{QE})^2}]^2}. \tag{5.2}$$

For the axial mass, NEUT uses a value of $M_A^{QE} = 1.21 \pm 0.20\ GeV/c^2$ based on measurements made by K2K [47] and MiniBooNE [48]. NEUT simulates the nuclear medium using the relativistic fermi gas model of Smith and Moniz [46]. The fermi momentum is set to 225 MeV/c^2 and the binding energy is 27 MeV.

To estimate the neutral current elastic scattering, NEUT uses the following relations[49, 50]:

$$\begin{array}{rcccl} \sigma(\nu p \to \nu p) & = & 0.153 & \times & \sigma(\nu n \to l^- p) \\ \sigma(\bar{\nu} p \to \bar{\nu} p) & = & 0.218 & \times & \sigma(\bar{\nu} n \to l^+ p) \\ \sigma(\nu n \to \nu n) & = & 1.500 & \times & \sigma(\nu p \to \nu p) \\ \sigma(\bar{\nu} n \to \bar{\nu} n) & = & 1.000 & \times & \sigma(\bar{\nu} p \to \bar{\nu} p) \end{array}$$

5.2.2 Single Meson Production

NEUT uses the Rein-Segal model to simulate single π, η, and K production. This consists of a neutrino interaction, producing a baryon resonance, followed by the decay of that resonance, producing a meson, as in:

$$\begin{array}{rcl} \nu + N & \to & l + N' \\ N' & \to & m + N' \end{array}$$

To calculate the total cross section, NEUT takes into account 18 baryon resonances below 2 GeV. The individual cross sections are then summed with the interferences from overlapping resonances taken into account.

The production cross section for a neutrino to produce a baryon resonance of negligible width is given by:

$$\frac{d\sigma}{dq^2 d\upsilon} = \frac{1}{32\pi m_N E^2} \frac{1}{2} \sum_{spins} |T(\nu N \to l N^*)|^2 \delta(W^2 - M^2) \tag{5.3}$$

where υ is the outgoing resonance momentum, W is the hadronic invariant mass, and M is the pole mass. The transition matrix element is given by:

$$T(\nu N \to l N^*) = \frac{G}{\sqrt{2}} [\bar{u}_l \gamma^\beta (1 - \gamma_5) u_\nu] \langle N^* | J_\beta^+(0) | N \rangle \tag{5.4}$$

The Rein-Segal model uses the relativistic harmonic oscillator quark model to calculate the hadronic part of the matrix element. To take into account of the finite width of the baryon resonance, the delta function is replaced by the Breit-Wigner factor as in:

$$\delta(W - M) \to \frac{1}{2\pi} \frac{\Gamma}{(W - M)^2 + \Gamma^2/4} \tag{5.5}$$

and the cross section is integrated over the appropriate bounds. As in the case of quasi-elastic scattering, the cross section is parameterized by form factors that depend on an axial mass. The axial mass has been set to $M_A^{RES} =$

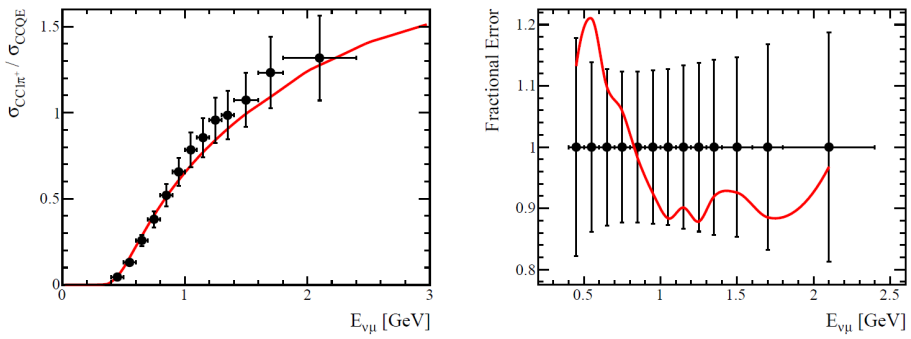

Figure 5.3: Comparison between the NEUT simulation and the MiniBooNE experiment for CC π^+ production

$1.21 \pm 0.2\ GeV/c^2$ based on results from K2K [53, 54], MiniBooNE [55, 56] and SciBooNE [57] for both CC and NC interactions. Figure 5.3 and Figure 5.4 show comparisons between NEUT and MiniBooNE data for single pion production.

5.2.3 Deep Inelastic Scattering

The cross section for deep inelastic scattering (DIS) is given by:

$$\begin{aligned}\frac{d^2\sigma}{dxdy} = \frac{G_F^2 M_N E_\nu}{\pi} \times \\ [(1 - y + \frac{1}{2}y^2 + C_1)F_2(x,q^2) \\ \pm y(1 - \frac{1}{2}y + C_2)xF_3(x,q^2)]\end{aligned} \tag{5.6}$$

where

$$\begin{aligned} C_1 &= \frac{yM_l^2}{4M_N E_\nu x} - \frac{xyM_N}{2E_\nu} - \frac{M_l^2}{4E_\nu} - \frac{M_l^2}{2M_N E_\nu x} \\ C_2 &= -\frac{M_l^2}{4M_N E_\nu x} \\ x &= -\frac{q^2}{2M(E_\nu - E_l)} \\ y &= \frac{E_\nu - E_l}{E_\nu}. \end{aligned}$$

To calculate the cross section, NEUT uses the nucleon structure functions from GRV98 [58] for F_2 and xF_3, and includes corrections in the low Q^2 region

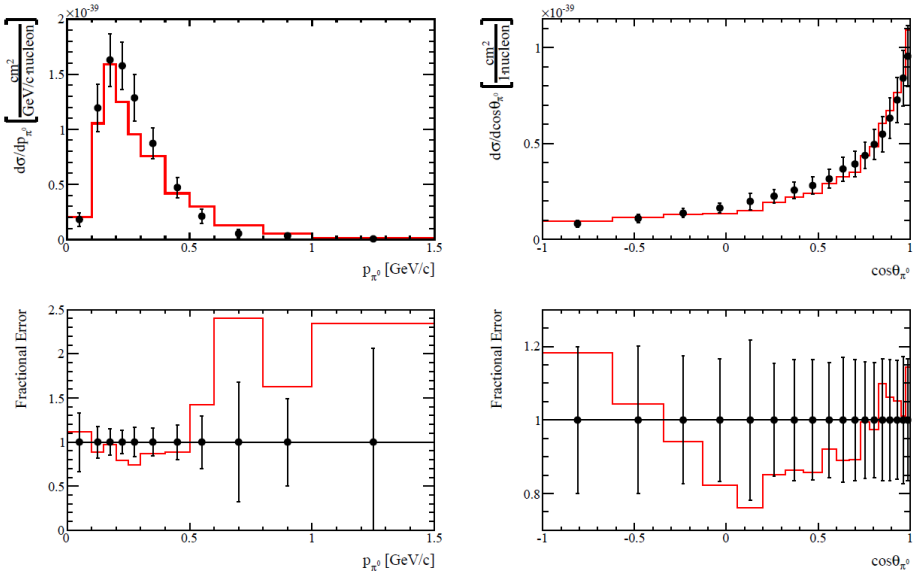

Figure 5.4: Comparison between the NEUT simulation and the MiniBooNE experiment for NC π^0 production

developed by Bodek and Yang [59]. NEUT requires the hadronic invariant mass W to be greater than 1.3 GeV/c^2 and the pion multiplicity to be 2 or greater for $1.3 < W < 2$ GeV/c^2, since single pion production is already taken into account in this region. To generate the multi-hadron states NEUT uses two models: a custom-made program [60] based on data for $1.3 < W < 2$ GeV/c^2, and the PYTHIA/JETSET [61] package for $W > 2$ GeV/c^2.

5.2.4 Coherent Pion Production

Coherent pion production is the process where a neutrino interacts with the entire nucleus, with each nucleon interacting coherently, producing a pion. NEUT simulates coherent pion production using the Rein-Sehgal model [62] and includes updates [63] to the model that attempts to explain the lack of evidence for charge current coherent pion production observed by K2K [64] and SciBooNE [65]. For neutral current coherent pion production, the expectation from NEUT is consistent with recent measurements [66] from the SciBooNE experiment. As in the case with the previous interactions, the cross section for coherent pion production is described in terms of form factors that depend on an axial mass term. The current value for that term is $M_A^{Coh\pi} = 1.0 \pm 0.5$ GeV/c^2. Justification for the choice of this and the other parameters are described elsewhere [67].

5.2.5 Nuclear Effects

The hadrons produced in the primary neutrino-nucleon interactions may undergo secondary interactions, called final state interactions (FSI), with the nuclear medium. These interactions are simulated using a semi-classical cascade model, with each particle traced until it exits the nucleus. The particle is traced along a path that is divided into steps. At each step the probability of a particular interaction is calculated according to a particular model. A random number is generated to determine what, if any, interaction occurs at a given step. Pions, for instance, as they pass through the nuclear medium, may undergo absorption, charge exchange, or scattering. Details of the NEUT cascade model can be found elsewhere [43, 68].

5.3 Detector Simulation

The detector simulation is composed of two separate software packages: the ND280 detector simulation and the electronics simulation.

5.3.1 nd280MC: The T2K Off-Axis Detector Simulation

The ND280 detector simulation, nd280MC, is based on the GEANT4 package [69]. The GEANT4 package takes the output kinematics of particles simulated by the event generator and simulates their passage through the detector. The detector geometry is stored in a ROOT file that includes the shape and composition of significant detector component. As the particle traverses the detector, the energy deposition is stored if it occurs in an active region of the detector. The particle trajectory information is also saved, tracing the particles path step by step. Particles produced from the interactions of primary particles (i.e. decays, pair production, etc.) are also tracked and their information saved. The detector simulation is controlled using GEANT4's macro language, allowing runtime control of detector geometries and thresholds for saving formation among other things. Details of the GEANT4 physics can be found in the documentation [70].

5.3.2 elecSim: The Electronics Simulation

The purpose of elecSim is to simulate the response of the electronics to energy deposited in the active regions of the detector. The simulation proceeds in a chain of three steps: simulation of the active medium, simulation of the MPPC sensor response, and simulation of the Trip-t electronics. In the first step, the simulation takes the energy deposited from nd280MC and converts that into a number of photons. The number of photons per MeV has been set to 39.3. This conversion factor was tuned using throughgoing muons. The

attenuation of the light as it travels down the fiber is also simulated. Next the MPPC response to the light from the fiber is simulated. First, a Monte Carlo process is used to create noise hits with timing, pixel position, and hit type and stores them in a container. Next the potential hits from photons from the fiber are stored in the same container. Noise hits are distributed uniformly in position on the face of the MPPC and uniformly in time within the integration cycle. The position of photon hits is based on the light model of the fiber, which can be either a uniform or 2-D gaussian distribution. Hits due to noise will always generate an avalanche. In the case of photon hits, the photon detection efficiency controls whether an avalanche will occur.

Chapter 6

Summary of Data and Monte Carlo Samples

The data analyzed for this thesis work is an exposure of 8.55×10^{19} POT collected between Run I (March 2010 - June 2010) and Run II (November 2010 - February 2011) while the PØD water target was filled. Due to a leak in one of the water bags, the PØD was drained in February 2011 and data was taken while the PØD was empty up until the earthquake in March 2011. The results from that data-taking period are not reported. The POT for each run period is shown in Table 6.1 and the accumulated POT as a function of time is shown in Figure 6.1. The data was initially processed using the official ND280 software production, called Production 4B, which was used for a variety of near detector analyses. The software was reprocessed locally at Stony Brook University using an updated version of the PØD reconstruction, with all other software packages unchanged. This reprocessing was necessary to correct an inconsistency in the way the MPPC saturation correction is handled between the detector and simulation. This fix has been incorporated into the official software production after 4B.

To select good beam spills, we require both the PØD and the Magnet to have good detector quality as defined by the ND280 Data Quality Group [71]. Since this analysis only uses the results of the PØD detector, the statuses of other detectors were ignored.

Table 6.1: Protons on Target for Run I and Run II data taking with the water in the PØD.

Protons on Target	
Run I	2.85×10^{19}
Run II	5.70×10^{19}

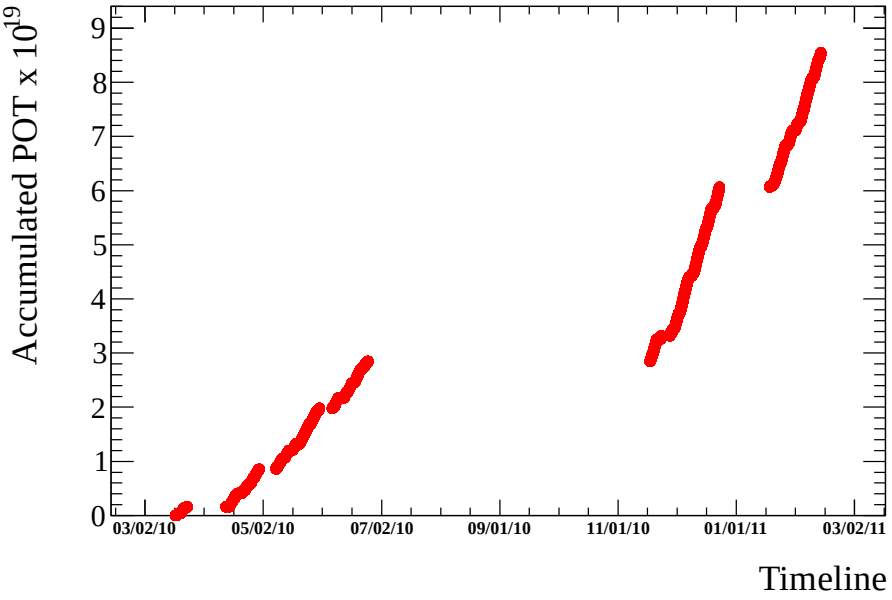

Figure 6.1: Total accumulated POT of the PØD water-in data-taking period.

Table 6.2: Summary of the simulated sample matching Run I and Run II. Beam configuration A(B) corresponds to the 6(8) bunch proton beam.

NEUT MC Summary			
Period	MC Configuration	Beam Configuration	POT
Run I	2010-02-water	A	55.65×10^{19}
Run II	2010-11-water	B	110.15×10^{19}

The simulated sample comes from NEUT Run I and Run II simulation with water in the PØD. The simulation includes the interactions in the entire ND280 Off-Axis detector, including those in the magnet, but not those in the surrounding ground. The beam configuration, POT and normalization for each sample is shown in Table 6.2.

Chapter 7

Event Reconstruction

The PØD reconstruction (p0dRecon) is divided into two main sequential algorithm chains. The first chain is the track reconstruction, which is then followed by the shower reconstruction. The input to the reconstruction is a single collection of PØD hits that will have come from either: the calibration (Chapter 3) for data hits or the electronics simulation (elecSim) for MC simulated hits (Chapter 5). As the PØD electronics produces hits subdivided into 23 cycles, 6 (8) of which will contain neutrino beam for Run I (II), and the cycles are predominantly independent, the first stage of the reconstruction is to separate hits into cycles. The track and shower reconstruction then run on each cycle. At the conclustion of the reconstruction chain, a muon decay search is performed on the hits in the entire beam spill. This chapter details the reconstruction algorithms.

7.1 Hit Filtering and Noise Rejection

The first algorithm in the chain is the rejection of noise hits. Noise hits are low in charge and uncorrelated to the higher charge hits from particle interactions. Therefore, a hit is retained if any of the following three conditions are true:

- It has charge $Q > 15$ *p.e.*
- It has charge $Q > 7$ *p.e.* and has a neighbor in the same view within 30 ns in time and 10 cm in space.
- It has a neighbor within 30 ns in time and 3.5 mm in space (with no charge requirement).

No charge requirement is applied to the neighbor. Hits failing all three of these conditions are excluded from the rest of the reconstruction. Only cycles with at least 5 cleaned hits continue in the reconstruction.

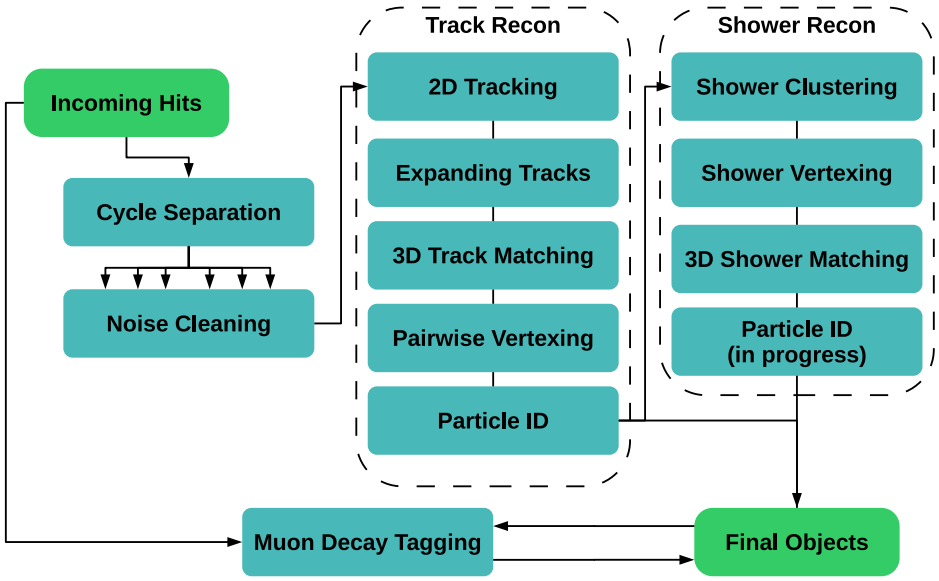

Figure 7.1: A flow chart of the algorithm chain of the PØD reconstruction package.

7.2 Track Reconstruction

7.2.1 2D Tracking

The cleaned hits are then passed to a 2D tracking algorithm. Each of the two 2D views, xz and yz, are considered separately. Track seeds are constructed from a Hough Transform [72] which selects hits that conform to a straight line. The transform is constructed with bin sizes of 1.8° and 25 mm, and seeds must have a minimum of 4 hits.

Once a seed has been constructed, it is extended layer-by-layer using a road following algorithm, based on a Kalman filter [32, 73], which adds hits within a 60 mm wide road, allowing for scattering of up to 0.15 rad. Once a layer has been added, up to 3 extra adjacent hits within the layer are also included.

Finally, the 2D track is extended non-exclusively at the end, so that hits near the vertex can be shared between multiple tracks. A maximum of 4 extra hits are included, using a 40 mm wide road, with no scattering allowed.

7.2.2 3D Track Matching

Once the 2D tracks are fully reconstructed, they are matched between the two views. The intention is to match as many tracks as possible, allowing for one-to-many matchings if required, as there is a good chance that tracks overlap in one view, but can still be distinguished in the other.

Each 2D track is considered in turn, comparing it with 2D tracks from the other view or 3D tracks already constructed from another pair. Each pair is weighted, based on an algorithm that accounts for the number of overlapping layers, the relative disparity between the charges of the two tracks, and whether a track has already been matched. The best possible pairing is selected, and then the algorithm runs again over the remaining 2D tracks, until no possible pairing scores above a set threshold.

7.2.3 3D Vertexing

The full set of 2D and 3D tracks are then passed to a pairwise vertexing algorithm. Potential vertices are created from pairs of tracks by projecting the Kalman fitted direction upstream until the point of closest approach. With the exception of two 2D tracks from different views, each pairing of tracks is considered, including tracks paired with themselves. For these self-paired vertices, the location is the front of the track, otherwise it is the point of closest approach, and the position variance is assigned based on the position and direction variances of the two tracks. Vertices are rejected if: the times of the two tracks are inconsistent ($\Delta t > 40\ ns$), the x or y position uncertainty is greater than 50 cm, or the z position uncertainty is greater than 50 cm.

The selection of candidate vertices are then clustered, as long as the times are consistent ($\Delta t < 40\ ns$), and are not separated by more than 20 cm. Each time, the best matching pair is clustered and removed, being reintroduced as a single vertex, until all vertices have been clustered or no more matchings are possible.

7.2.4 Particle Identification

In last step of the track reconstruction, a particle identification algorithm is run on each of the reconstructed tracks, producing PID objects (TReconPIDs). In the absence of special cases, the particle identification considers two hypotheses: kLightTrack objects, which primarily consist of muons, pions and protons, and kEM objects, which consist of gammas and electrons. The algorithm is based on energy deposition variables in the PØD and requires that the tracks are fully contained in the detector and that the track is fitted with a Kalman fitter. Tracks that fail any of those requirements are considered special cases and are automatically labeled as kOther objects. An additional special case exists for tracks that exit the PØD. Because the particle identifiaction depends on energy deposition, and for exiting tracks this information is lost, these exiting tracks are automatically identified as kLightTrack objects.

Four variables are considered: the charge asymmetry between xz and yz layers in a PØDule, the charge asymmetry between neighboring PØDules, the number of layers with no charge deposit, and the fraction of charge deposited

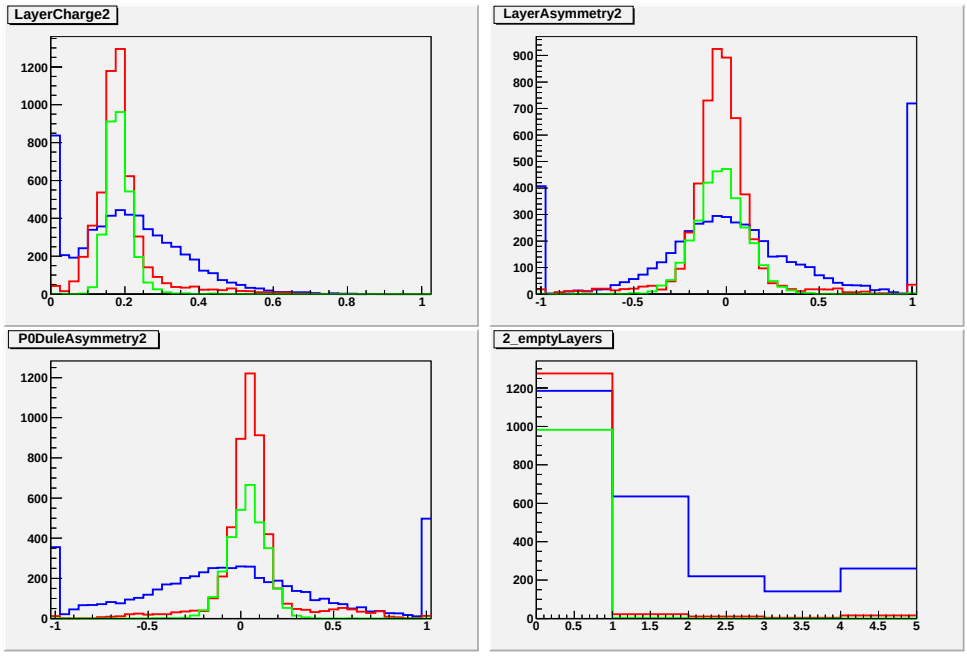

Figure 7.2: Variables used for the particle identification. Top Left: Layer Charge. Top Right: Layer Asymmetry. Bottom Right: Empty Layers. Bottom Left: P0Dule Asymmetry. LightTracks are green. EMs are blue. HeavyTracks are red (not used in this analysis).

in the last five layers of the track. For each of these variables, a pdf template is produced using MC simulated muons and electrons. A likelihood function is then constructed from the value of the variable. The hypothesis with the maximum log-likelihood is chosen as the PID.

7.3 Shower Reconstruction

7.3.1 Shower Reconstruction

The shower reconstruction takes the results of the track reconstruction as input, which is a container of vertices, each containing constituent PID objects. It should be noted that if there are multiple vertices from the tracking algorithm, there must be PID objects identified as kLightTrack, and that the first vertex will contain at least one kLightTrack PID. Initially all the hits passing the cleaning stage are available to the shower reconstruction. The algorithm then iterates through each vertex, removing all hits that belong to PIDs other than kOther and kEM, and passes the remaining hits to the shower vertex algorithm, with the first tracking algorithm vertex as the input vertex in the search. If that vertex contains a kLightTrack PID then the shower vertex

is constrained to be within 5 cm in x and y and 10 cm in z of that vertex. If the vertex does not contain a kLightTrack PID, all the hits are passed to a clustering algorithm to reconstruct the showers and fit the vertex. It is this latter case that is relevant to this analysis.

The shower vertex reconstruction works under the assumption that the hits from showers will fall in a cone when viewed from the interaction vertex. The shower vertex fitter first passes the available hits to a clustering algorithm, which searches for shower seeds using a Hough Transform. With the shower seeds found, a separate algorithm adds neighboring hits to the seed, forming a 2D shower. These reconstructed 2D showers are then passed back to the vertex fitter. Constraints are then applied to the search region of the vertex based on the geometry of the shower. The vertex position is required to be within 100 cm of the shower start position; it is required to be a greater distance away than the width of the shower at the vertex start position; lastly the vertex position must be located sufficiently close to the shower directional axis such that the transverse direction is not larger than the width of the shower.

A grid search is then run within the defined boundaries to locate the best possible vertex position as determined by a likelihood function. The step size of the grid search is initially 4 cm. Several iterations of the grid search are performed, with the step size decreasing by a factor of $^1/_2$ at each iteration until the step size is less than 0.5 cm. At each iteration, hits in each 2D projection are clustered based on their angular separation, with the vertex position as the reference point. With the resulting clusters, the likelihood function is then calculated from 4 quantities: unassigned charge, number of clusters, angular width of clusters, and distance of hits from the vertex. The first quantity penalizes vertex positions in which the angular clustering results in a large number of non-clustered hits. The second quantity penalizes vertex positions in which there are 3 or more clusters, under the assumption that a π^0 will produce at most 2 clusters in each 2D projection. The third quantity penalizes vertex positions that result in clusters that subtend very wide angles. Finally, the fourth term penalizes vertex positions that are a large distance from the first shower hits.

The total likelihood function is then calculated from the sum of the likelihood in each 2D projection. The vertex position is then determined from the position that maximizes this likelihood. The reconstructed showers are determined from the clusters at this position.

7.3.2 3D Shower Matching

The reconstructed showers from the shower reconstruction are 2D objects. As this analysis requires the full 3D information to calculate the invariant mass, it is necessary to match the showers in orthogonal projections, producing 3D showers. As a result, there is an algorithm in p0dRecon that

attempts to perform this matching. For each xz and yz shower pair, a score is calculated from the separation in z of the starting point of the showers, as well as the number of matching and mismatching layers occupied by the showers' hits, where a layer is considered to be a layer of scintillator planes. It is considered a match if both showers have hits in the same layer or any adjacent layer. Otherwise, it is considered a mismatch. The score is then calculated from

$$\text{Score} = (10\text{cm} - \text{dist}) \times \frac{\text{matches}}{\text{matches} + \text{mismatches}} \tag{7.1}$$

where dist is the separation of the showers in z. Once the showers have been matched, a separate algorithm [74] determines the correct charge of a shower in case multiple showers overlap in one of the 2D projections.

7.4 Muon Decay Tagging

To reject charged current events where the muon is either too low in energy to be properly tracked, or where the particle identification has misidentified the track as being EM-like, we employ an algorithm that tags clusters of hits representitive of muon decay. For each reconstruction object found in the spill, the algorithm selects hits 100 ns later in time as candidates for the clustering. The algorithm then selects clusters of hits occuring within a time window of 20 ns, and spatial span of 9 cm. Good decay clusters are selected from these candidate clusters if any of the hits in the cluster are separated from the hits in the reconstruction object by no more than 9 cm. In addition, the total hit charge in the cluster is required to be less than 500 P.E. to reject clusters from neutrino interactions.

The muon decay tagger has been tested using sand muons stopping in the PØD. Out of a total of 4862 true muon decays, the algorithm tagged 1666 decays correctly and misidentified 1320, giving an efficiency of 34% and a purity of 56%.

7.5 Data Summary Tree

The results of p0dRecon are stored in ROOT [75] files along with the output of the other detector reconstruction algorithms. MC files are typically on the order of GB in size, making practical analysis on a large sample of them impossible. Because of this, there is a dedicated software package, oaAnalysis, that is designed to take the results of the reconstruction and convert it into a pure ROOT format. This has the two-fold benefit of making the files smaller and therefore portable, in addition to allowing the individuals performing the analyses to choose which information they would like to save.

For each reconstruction module, there is a separate module that performs the reduction.

For p0dRecon, the summary module is called the TP0DReconModule. The module was designed to be as generic as possible so as to provide access to a large amount of information, without making any assumptions about the structure of the reconstruction output. In the P0DReconModule, there are objects representing vertices, tracks, showers, particles clusters and algorithm results. For each of these objects important information such as time, energy, position, etc. is stored.

7.6 The Absolute Energy Scale Estimator

The energy scale has been estimated using 200,000 MC simulated gamma-rays with energies uniformly distributed below 1 GeV and an isotropic angular distribution. The software version used for this analysis was the same one used for the event reconstruction. The gamma-rays were processed through nd280MC, elecSim, and p0dRecon. Only photons that deposited at least 90% of their energy inside the PØD (limiting the energy scale to fully contained gamma-rays) and which had at least 90% of the collected charge in a single TReconPID object were used for this analysis. For the rest of this section, "fully contained" will mean that at least 90% of the photon energy is deposited in the P0D.

7.6.1 The Estimator

The energy estimator described here is limited to information available in the oaAnalysis files. For showers, we currently save the attenuation-corrected charge for the entire shower, as well as the attenuation-corrected charge for between three and five clusters distributed along the shower. For simplicity, the total attenuation corrected charge has been chosen as the energy estimator.

Figure 7.3 shows the distribution of true energy versus the reconstructed charge for fully contained gamma-rays. This figure shows that there is a large feed-down of high energy gamma-rays to lower total charges. Since there is significant feed-down, within any slice of total charge (e.g. between 1000 and 1100 PEU), the mean true energy is biased and the peak of the true energy distribution will be used instead. This effect can be seen in Figure 7.4.

Figure 7.3 shows the result of the fit to the peak of the true energy for all slices of the attenuation-corrected charge. Each slice has a width of 100 PEU. Each slice is fitted to a Gaussian over a limited range chosen to include the mode of the distribution. This range was determined using the position of the 5% and 70% quantiles which represents a trade-off between fitting a significant region around the peak, while limiting the effect of the tail on the fit result. To be included in the histogram, the fit to a slice must have at least one degree

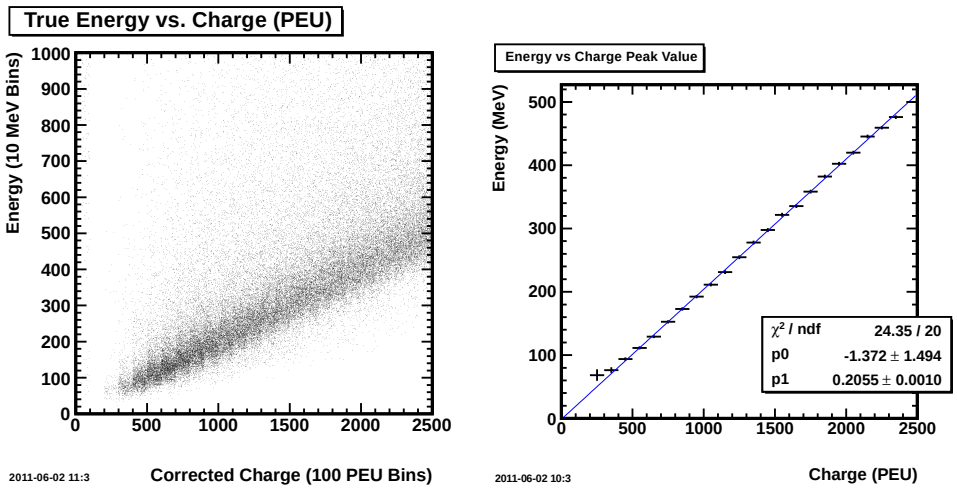

Figure 7.3: The left panel shows the true energy versus the total attenuation corrected charge for reconstructed kEM objects. The right panel shows the fitted peak value of the true energy distribution for each slice in the total attenuation corrected charge vs the total attenuation corrected charge. Only bins with correct fits are shown.

of freedom, and the width of the fitted Gaussian must be less than 1 GeV. The latter criteria eliminated one low statistics bin near the reconstruction threshold. Four examples of fits to the slices can be seen in Figure 7.4 where due to the skew of the distributions a fit to a Gaussian results in a large χ^2 per degree of freedom, and hence an underestimate in the uncertainty on the peak position. To account for this, the uncertainty on the peak position is taken as the RMS of the slice divided by the square-root of the number of entries (i.e. the uncertainty on the mean of the histogram is used as the uncertainty of the peak position).

The fitted peak positions versus the total attenuation-corrected charge are then fitted to a linear model to produce an estimate of the gamma-ray energy as a function of total charge. The parameters of the linear model, $E_\gamma = AQ + B$ are $A = 0.205 \pm 0.001$ MeV/PEU, and $B = -1.4 \pm 1.5$ MeV where Q is the total attenuation-corrected charge. Except at very low energy, this model provides a fairly good description of the peak position as a function of charge ($\chi^2/D.O.F. = 24.4/20$). Below about 80 MeV the effect of the single gamma-ray threshold introduces a bias toward higher energy. We do not expect this to be a significant effect in the π^0 analysis due to the kinematics of the neutral current π^0 production. Since the constant term, B, is consistent with zero and negligibly small in comparison to the energy resolution, it is taken to be zero. As a result, the final energy estimator is

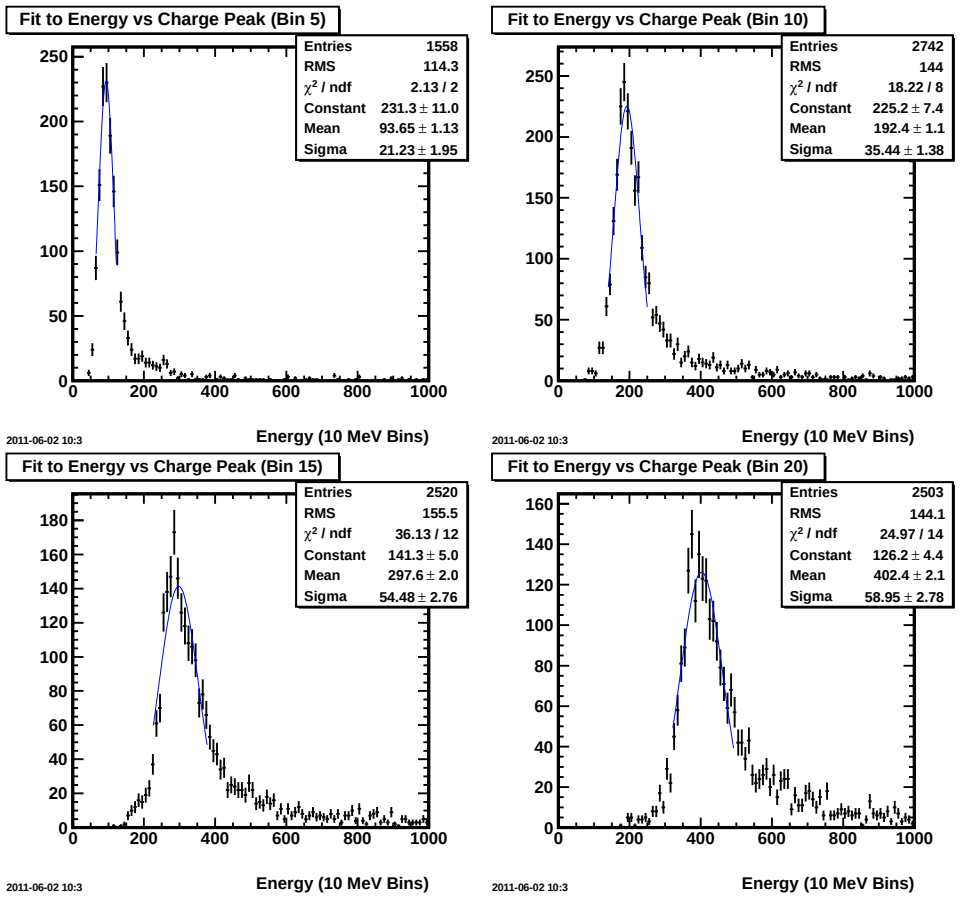

Figure 7.4: The true energy for four different slices in the total attenuation corrected charge. The bins correspond to 500–600 PEU (top left), 1000–1100 PEU (top right), 1500–1600 PEU (bottom left), and 2000–2100 PEU (bottom right).

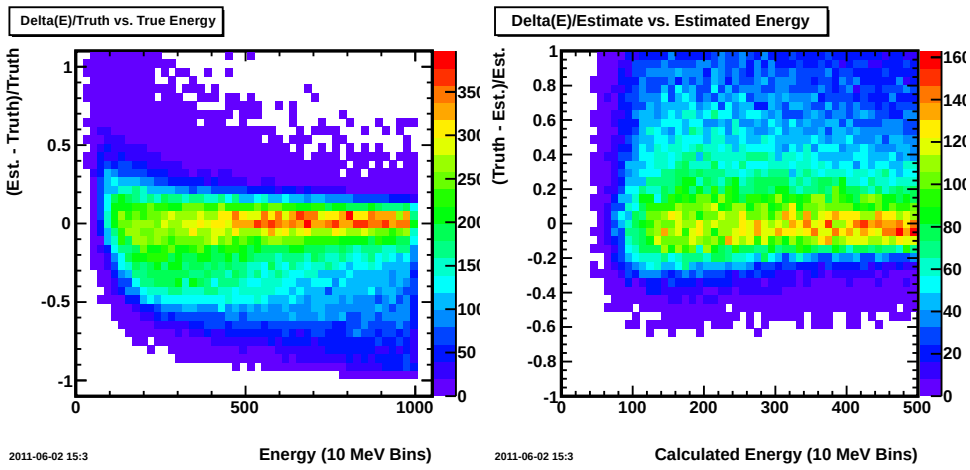

Figure 7.5: The fractional difference between the calculated and true energy as a function of the true energy (left) or the calculated energy (right).

$$E_\gamma = (0.205 \pm 0.001 \text{ MeV/PEU})\, Q \tag{7.2}$$

where Q is the total attenuation corrected charge of the gamma ray.

Energy Resolution

Figure 7.5 shows the fractional difference between the calculated and true energy for the gamma-rays. The left hand plot compares against the true value while the right hand plot compares against the calculated energy. While the distributions have significant tails, the peak values show little bias as a function of either true or estimated energy.

Figure 7.6 shows the fitted width of the energy distribution as a function of the total attenuation corrected charge. The resolution has been fit to

$$\frac{\sigma_E}{E\ (\text{GeV})} = \sqrt{\left(\frac{\sigma_s(\%)}{\sqrt{E\ (\text{GeV})}}\right)^2 + \left(\frac{\sigma_c(\%)}{E\ (\text{GeV})}\right)^2 + \sigma_0^2(\%)} \tag{7.3}$$

with the fitted values being $\sigma_s = 7 \pm 1\%$, $\sigma_c = 0$, and $\sigma_0 = 10 \pm 2.5\%$.

7.7 Reconstruction Results

7.7.1 Gamma Reconstruction

The results of the individual gamma reconstruction are shown in Figures 7.7 and 7.8. Figure 7.7 shows the reconstruction efficiency vs. Energy.

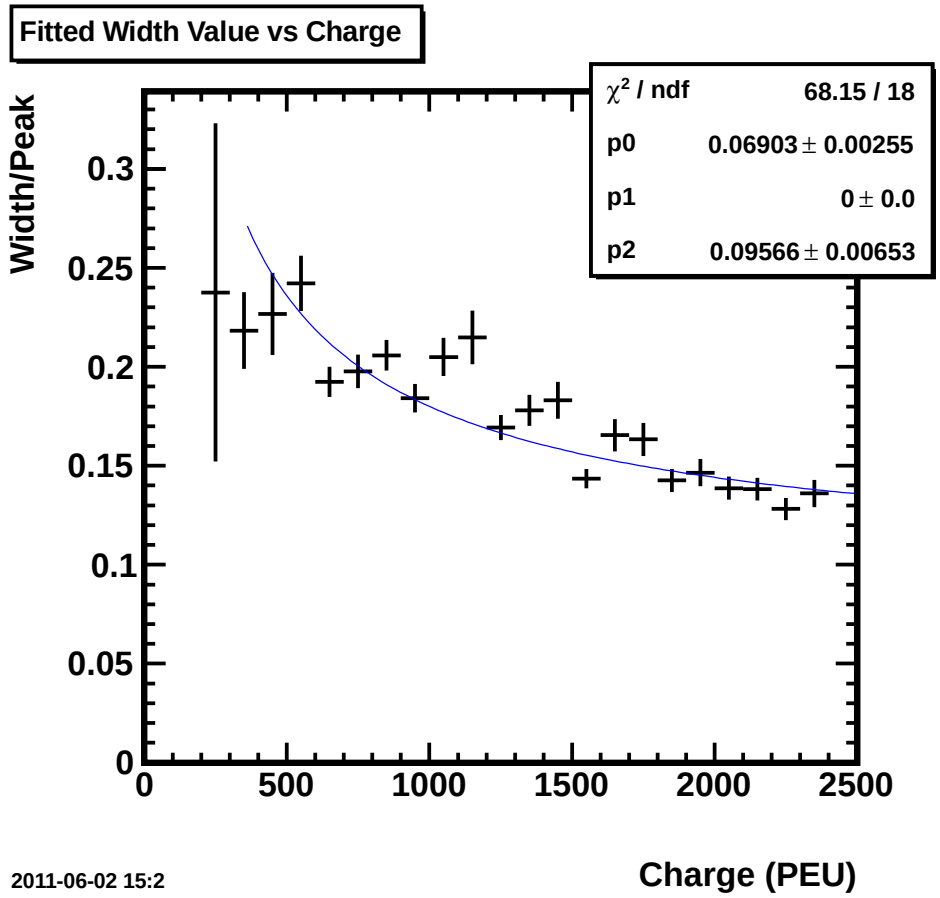

Figure 7.6: The fractional resolution as a function of the measured charge

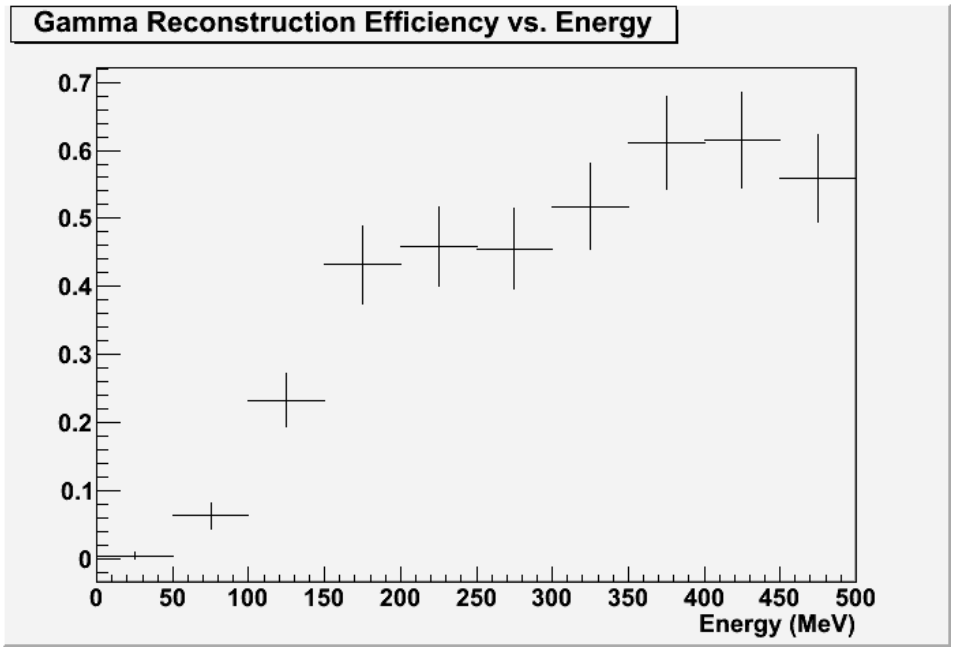

Figure 7.7: The efficiency to reconstruct a gamma as a function of energy

Table 7.1: The vertex position resolution for all NC1π^0 candidate events

X Shift (cm)	X Res. (cm)	Y Shift (cm)	Y Res. (cm)	Z Shift (cm)	Z Res. (cm)
-0.03	6.04	-0.10	7.48	3.30	11.86

The gamma must be correctly identified as kEM to be shown it plot. Figure 7.8 shows the energy and angle efficiency.

7.7.2 NC1π^0 Reconstruction

Figure 7.9 shows the vertex resolution distributions of NC1π^0 that pass all selection cuts described in Chapter 8. The vertex resolution refers to the difference between the true vertex and the final reconstructed vertex position. The resolution and shifts for events which pass all selection criteria are shown in Table 7.1. The columns of Table 7.1 give the shifts and resolutions for each coordinate. The shift is defined as the median of the true minus the reconstructed position and the resolution is defined as half of the distance between 16% and 84% of the integrated number of events.

Figure 7.10 shows the energy resolution of reconstructed NC1π^0 events passing all selection cuts described in Chapter 8. A Gaussian has been fit to the distribution between ± 0.2. The value of the fitted width is 0.16. Figure 7.11 shows the angle between the reconstructed π^0 direction and the true direction.

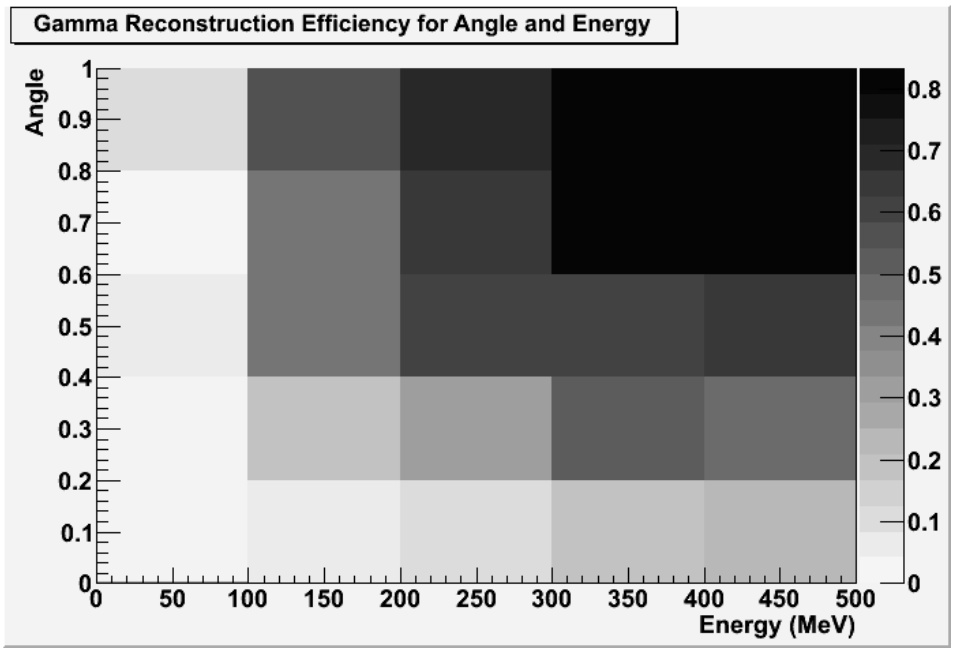

Figure 7.8: The efficiency to reconstruct a gamma as a function of energy and angle with respect to the z axis

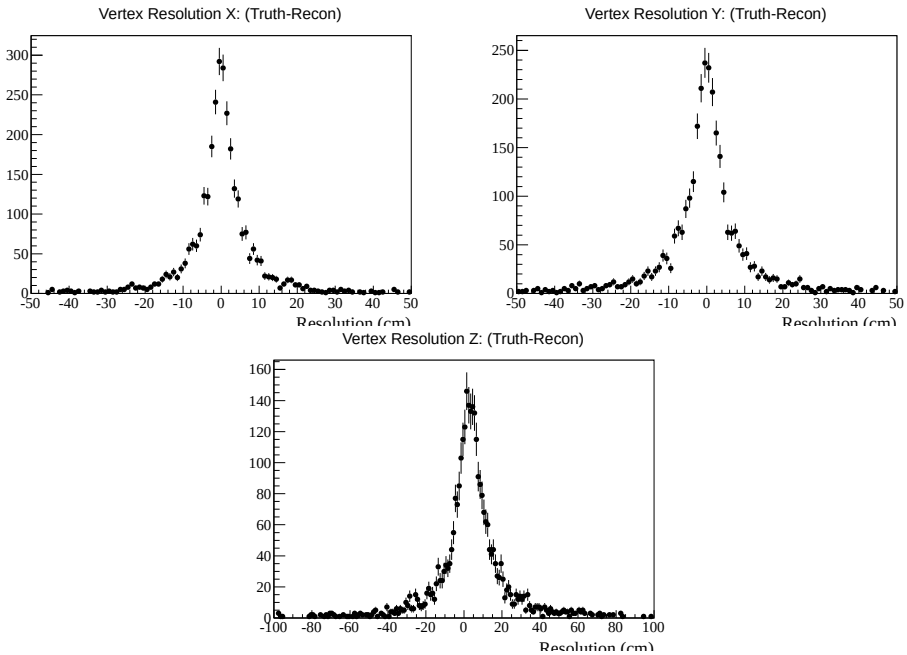

Figure 7.9: The vertex resolutions for signal events passing all selection cuts described in Chapter 8

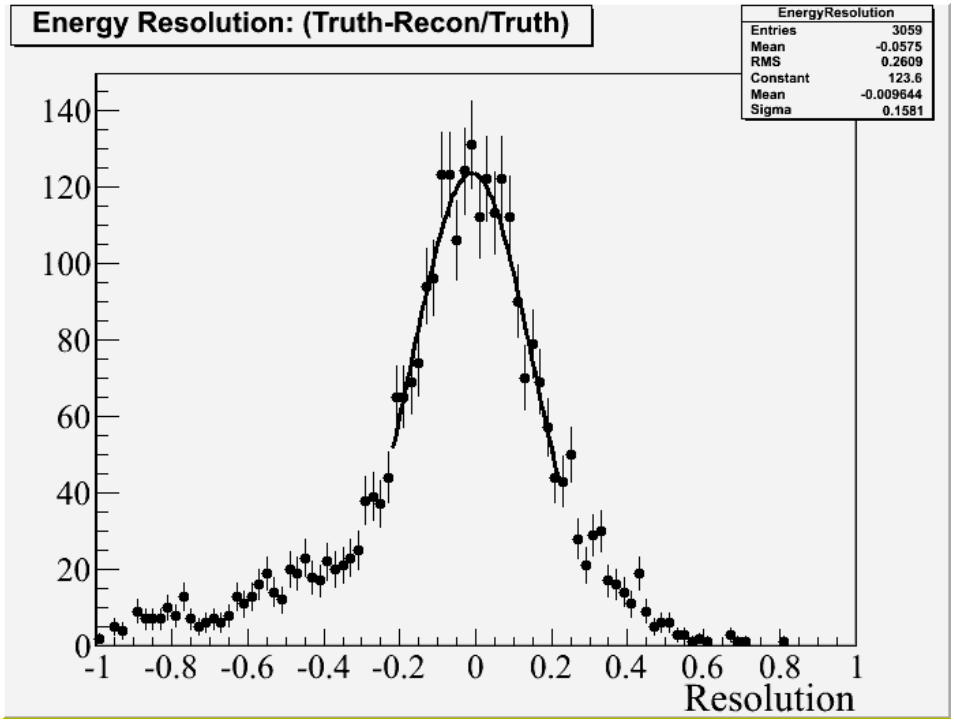

Figure 7.10: The energy resolution for signal events passing all selection cuts described in Chapter 8

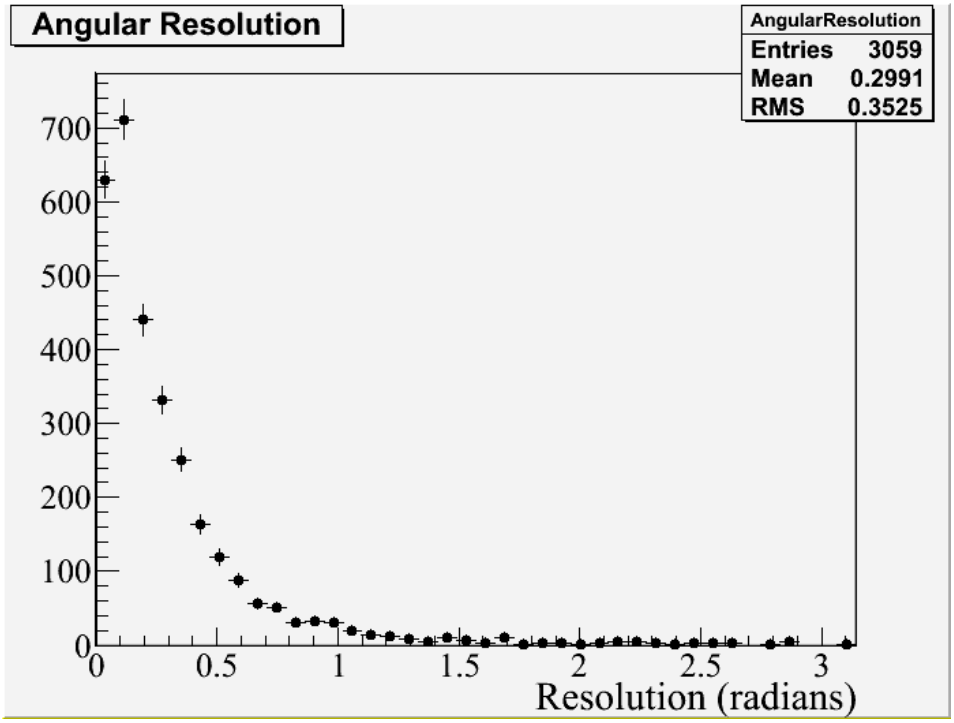

Figure 7.11: The difference in reconstructed vs. true angle for signal events passing all selection cuts described in Chapter 8

Chapter 8

Event Selection

This section summarizes the criteria used to select NC1π^0 events. The event selection is done on oaAnalysis files using only the information contained in the TP0DReconModule, as only the results of p0dRecon are used for this analysis. The p0dRecon algorithm chain is shown in Chapter 7. The results of the reconstruction are obtained for each TFB integration cycle so as to account for possible multiple interactions in a given beam spill. For the rest of this chapter, we define an event to be a cycle containing at least one reconstructed vertex.

Events are broken down into several categories to denote signal events as well as the different categories of background events. Signal events (Red), are NC1π^0 events as defined in Chapter 4. The background events are broken down into four categories: Charged Current (CC), Neutral Current (NC), external, and other. Charged current background events (Blue), are events with a charged lepton in the final state. Neutral current background events (Green), are events that are neutral current but not NC1π^0. External background events (Yellow), are events from neutrino interactions outside the PØD. Lastly, the category "other" (Black), are events where multiple true vertices produced reconstruction objects within the same cycle, thereby making it impossible to uniquely define the event.

8.1 Pre-selection

Prior to performing any selection cuts we require the event to have occurred within the 6(8) bunches that make up the beam spill for the Run I(II) beam configuration. For both the data and the simulation, the first beam bunch is always in time with the 5th cycle, with a cycle index 4. We therefore require the cycle index to be between 4 and 9(11) for Run I(II). Additionally, we require the event to have at least one reconstructed 3D vertex. In this analysis, this cut does not affect the number of events obtained in our final sample, but it is possible that it could.

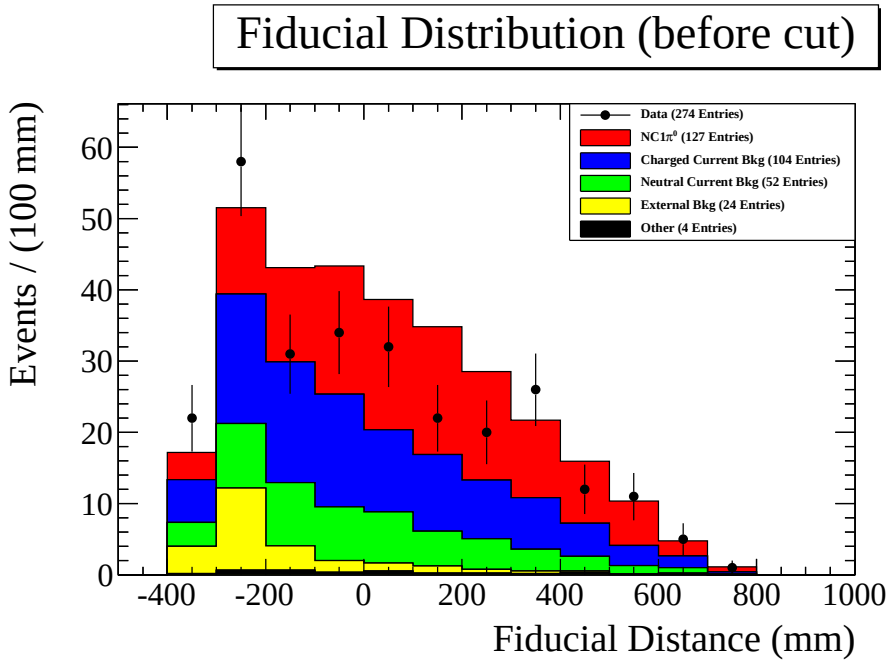

Figure 8.1: The distance from the edge of the fiducial volume defined in Table 8.1 for events passing all selection cuts except for the fiducial volume cut. Negative values indicate vertices reconstructed outside the fiducial volume. Events with vertices outside the fiducial volume are rejected.

8.2 Fiducial Volume Cut

To reduce external contamination, we select events with reconstructed vertices inside a fiducial volume. The fiducial volume is defined by a box centered about the central point of the Water Target Super-PØDule. The box is defined by a pre-determined half-width. The definition of the fiducial volume is shown in Table 8.1. Figure 8.1 shows the distribution of the miniminum distance from the edge of the fiducial volume. Events within the fiducial volume are defined as positive.

Figure 8.1 shows a discrepancy between the data and the MC for events inside the fiducial volume. As noted in the caption, the figure shows the fiducial distance of events passing all selection cuts except for the fiducial volume cut. Therefore it is possible for the distributions to disagree if the overall rate of NC1π^0 events is different in the simulation than it is in nature. Aside from one bin, the MC consistently overshoots the data, implying an overestimation of the number of NC1π^0 events. This is consistent with our final result described in Chapter 9.

Table 8.1: Definition of the PØD fiducial volume. Column 2 shows the center position for all three dimensions in global coordinates. Column 3 shows the half-widths of the box. Columns 3 and 4 give the minimum and maximum positions. All locations and dimensions are in units of millimeters.

Fiducial Volume				
Coordinate	Center	$\frac{\text{Width}}{2}$	Minimum	Maximum
X	-36	800	-836	764
Y	-1	870	-871	869
Z	-2116	853	-2969	-1264

8.3 Non-EM Track Cut

As described in Chapter 7, p0dRecon identifies tracks as EM or LightTrack. The LightTrack classification encompasses tracks produced by charged particles such as muons, protons, and pions, particles largely associated with charged current interactions. Due to the large relative size of the charged current cross section, events in the PØD consist mainly of charged current interactions and so an event with a LightTrack has a high probability of being a non-NC1π^0 interaction. We therefore reject any event that contains one or more of these tracks.

Figure 8.2 shows the distribution of the number of LightTrack particles contained in the candidate event. The data and MC are not necessarily expected to agree in the bin corresponding to 0 Non-EM constituents since that is the signal region in which we are measuring. In the bins corresponding to 1 or more Non-EM constituents there is disagreement that requires further explanation. The reason is twofold: the probability to identify a LightTrack is higher in data relative to MC due to differences in the PID parameter distributions, and the MC predicts a larger number of decay clusters coming from neutrons and so the muon cut removes events in the MC that would not pass the Non-EM constituents cut. To account for the former effect, we perform a study and include this as a systematic uncertainty in the final result. This is described in Chapter 10.

8.4 2D EM Cut

To fully reconstruct the π^0 invariant mass, it is necessary to have the energy and direction of both reconstructed γs. As described in Chapter 7, part of the PØD reconstruction is to match 2D showers in each projection, yielding 3-D EM showers. In some instances, the 3D matching will fail leaving

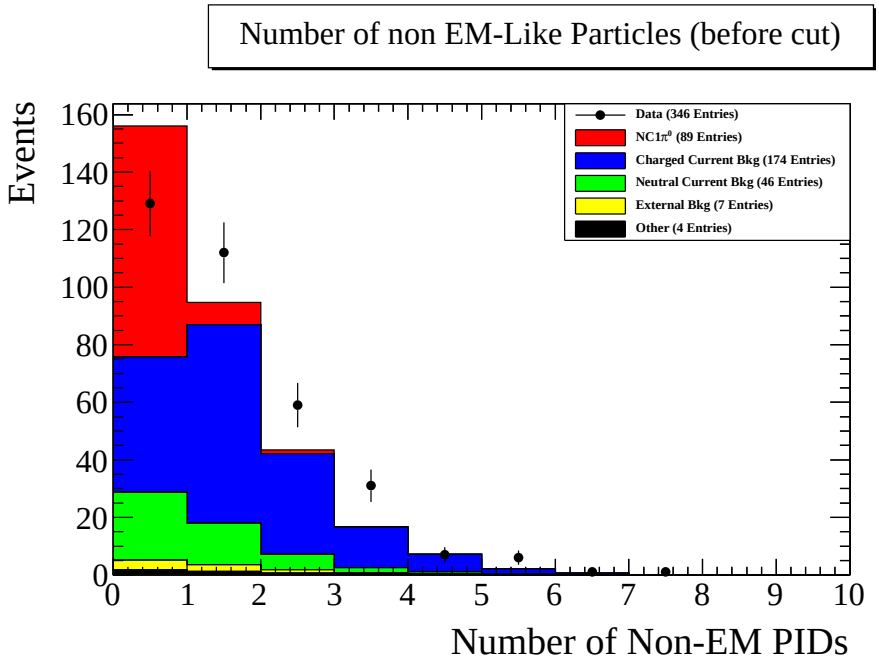

Figure 8.2: Number of Non-EM like reconstructed objects in events passing all selection cuts except the Non-EM cut.

only a 2D object. Since this implies that we have missing information in these cases, we reject any event where there is a 2-D EM particle in the final output. Figure 8.3 shows the number of 2-D EM particles per event after all other selection cuts have been applied. As is shown in the plot, the number of 2D showers that make it into our final sample is very small.

8.5 3D EM Cut

The most typical decay mode of the π^0 is the $\pi^0 \rightarrow \gamma\gamma$ channel. The Dalitz mode, $\pi^0 \rightarrow \gamma e^+ e^-$ has a branching ratio of 1% [12] and is ignored. We therefore expect two reconstructed 3D EM particles in the final state. We reject any events that do not meet this criterion.

8.6 Muon Decay Cut

In those instances where a muon is too low in energy or is otherwise misidentified, the detection of muon decay clusters provides another level of charged current filtering. Chapter 7 describes the algorithm used to reconstruct muon decay clusters. We reject any event where the algorithm tags a

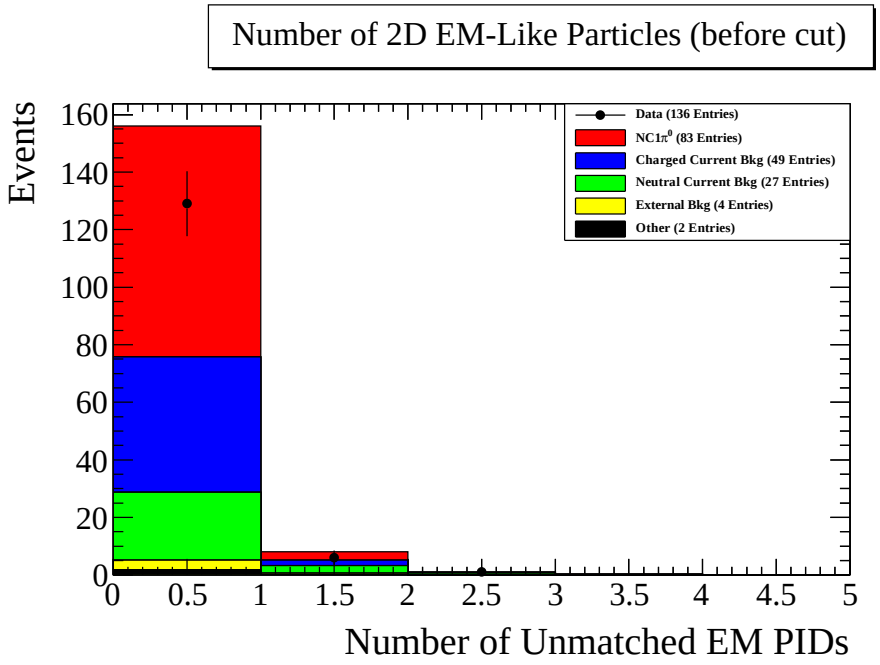

Figure 8.3: Number of reconstructed 2D EM-like objects in the event. All other selection cuts have been applied.

muon decay cluster in a event, with the condition that the decay cluster can not be in the same time cycle as the reconstructed vertex. The data and MC show disagreement in the distribution of the number of decay clusters. This is due to neutrons producing decay clusters at low energy in the MC. This has been observed in the PØD ν_e analysis [76], however due to the smaller event sizes, the effect is not as large in this analysis.

8.7 π^0 Direction Cut

The π^0 reconstruction efficiency is greatest for π^0s produced in the forward direction and approaches 0 as the angle with respect to the z-axis increases. In addition, at large angles the particle identification efficiency decreases, leading to more contamination from charged current events. Figure 8.6 shows the cosine of the π^0 angle with respect to the z-axis. At larger angles the contamination from background events is clearly visible. We reject events where the cosine of the reconstructed angle is less than 0.6, the value that maximizes the significance or the signal divided by the square root of the background. The discrepancy between data and MC in the forward direction is explained again by the fact that this is the signal region being measured.

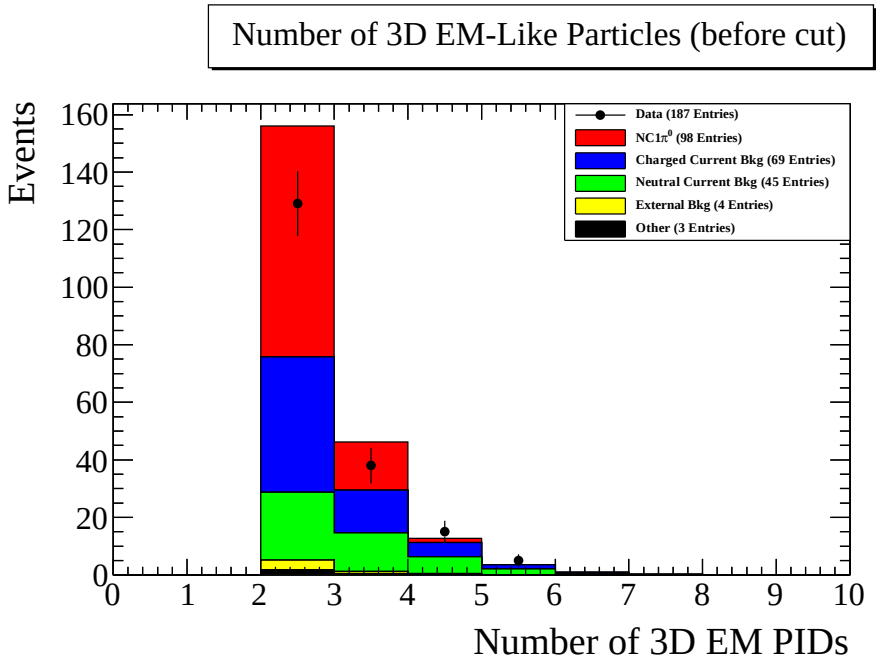

Figure 8.4: Number of reconstructed 3D EM like objects. All other selection cuts have been applied.

8.8 Shower Cluster-Charge Distribution Cut

To further reject those events where a shower is incorrectly reconstructed from a non-gamma particle we do a shower-like PID cut at the analysis level using the shower cluster information. Showers are made up of 3 to 5 clusters depending on the expanse of the shower. Several possibilities for a PID parameter were studied, with the best one involving the fractional charge difference between the first and last clusters in a shower. We take the charge of the last cluster and subtract from that the charge of the first cluster. The fractional difference is then obtained by dividing that difference by the total charge of the shower. This value is calculated for each reconstructed shower in the event and the maximum value is used for the discrimination. Figure 8.7 shows the distribution of this fractional charge difference. We reject events where this difference is larger that 0.027, which is one sigma from the expected signal mean.

8.9 Shower Separation Cut

Up to this point, the events remaining consist of a large number of reconstruction failures, in which spurious showers were reconstructed out of the

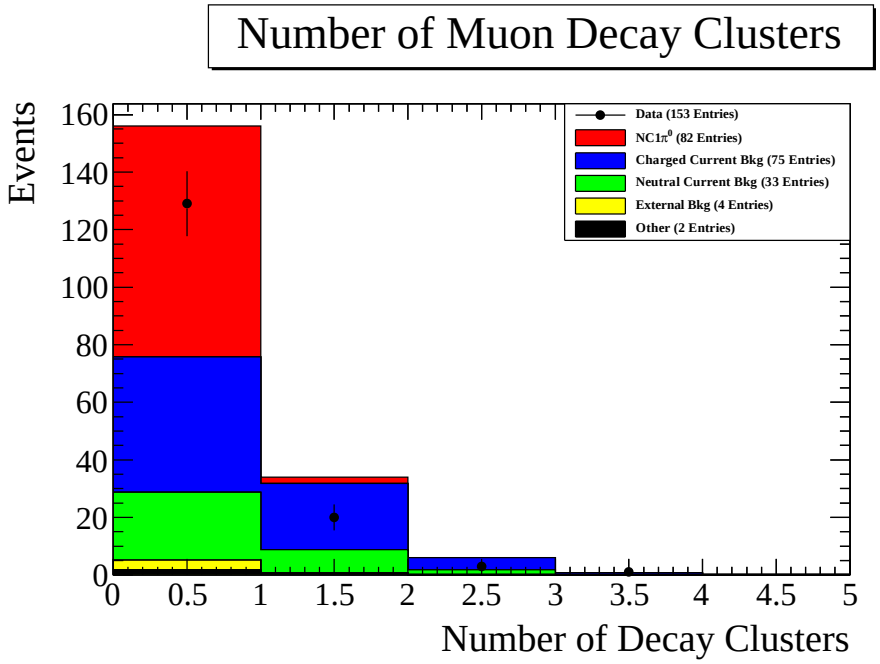

Figure 8.5: Number of reconstructed muon decay clusters. All other selection cuts have been applied.

hits. In background events, this can happen in low-energy interactions where the charged particle tracks are not reconstructed by the tracking algorithms. In signal events, this can happen when a decay gamma exits the PØD without producing any hits, and two showers are constructed out of the gamma that converted in the PØD. The effect on the invariant mass distribution is similiar in both cases since the reconstructed showers tend to have small opening angles, leading to a pile-up of events in the low-mass region. To reject the large amount of reconstruction failures remaining in the event sample, we place a cut on the spacial separation of the two reconstructed EM showers. A number of values (see Figure 8.9) were investigated between 0 and 100 mm, with 50 mm being chosen as the lowest value that flattens the background mass spectrum, determined by visual inspection of the MC only.

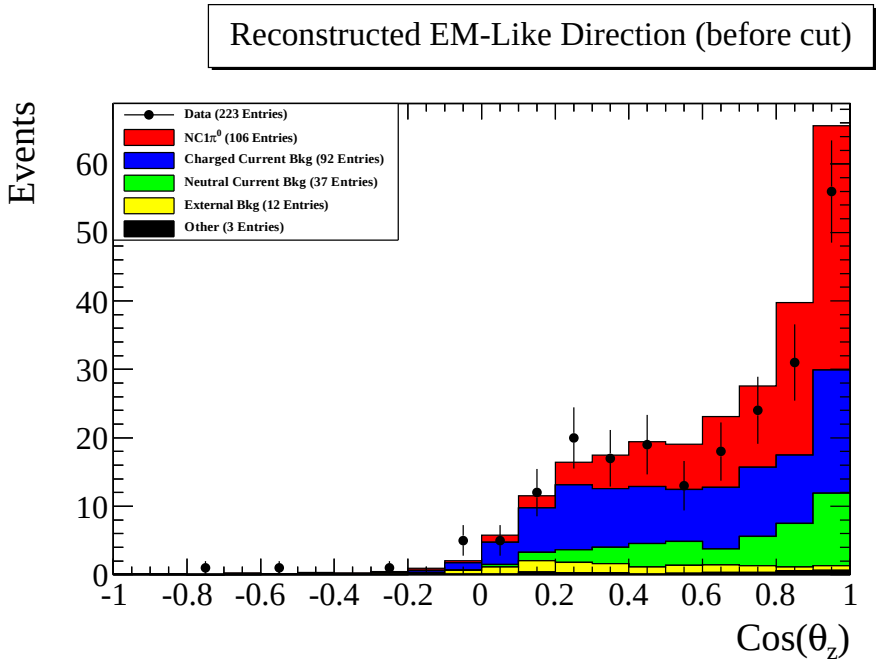

Figure 8.6: Reconstructed Pizero Direction. The angle plotted is the angle with respect to the z-axis of the PØD. All other selection cuts have been applied

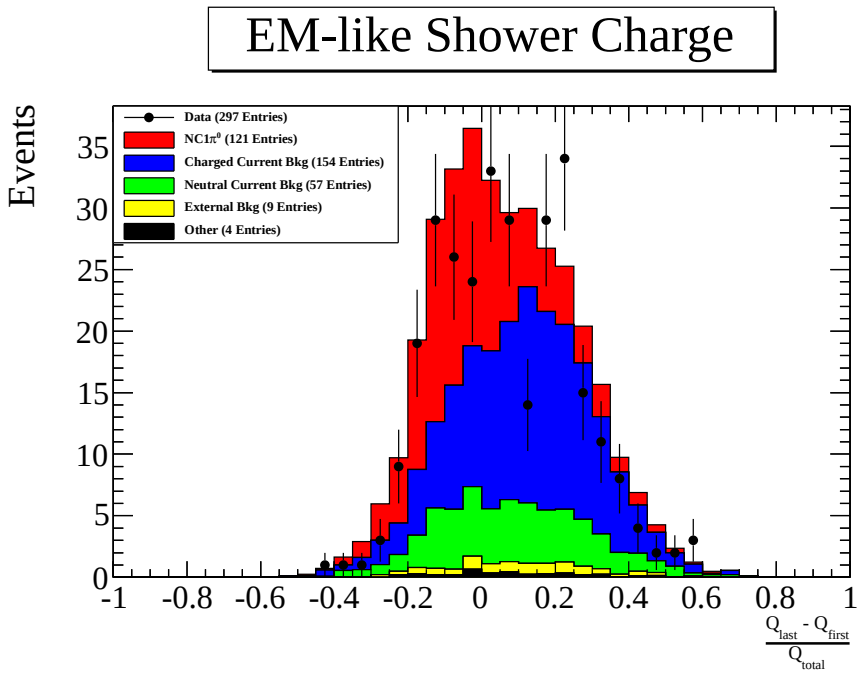

Figure 8.7: Fractional charge difference between the first and last cluster. All other selection cuts have been applied

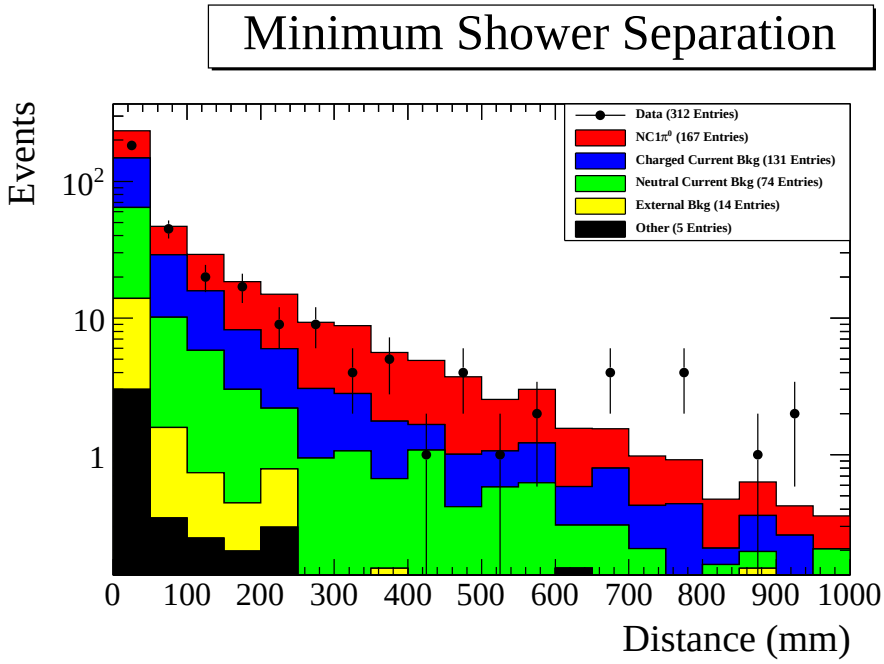

Figure 8.8: The separation of the reconstructed showers

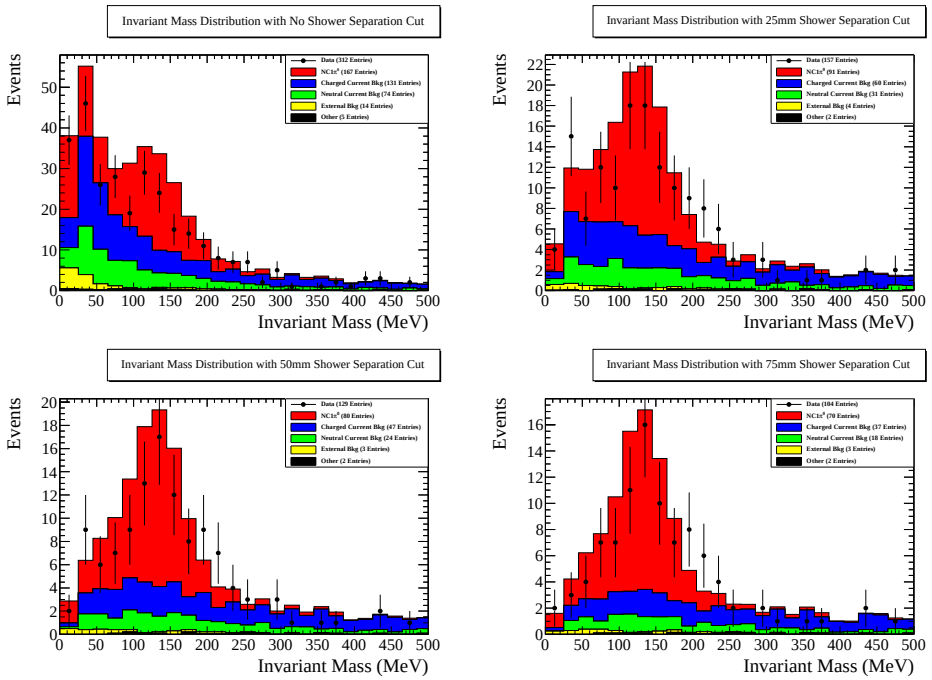

Figure 8.9: The effect of the nearest shower cut on the invariant mass distribution for several distances. Top Left: No separation cut. Top Right: 25mm shower separation. Lower Left: 50mm shower separation. Lower Right: 75mm shower separation.

Chapter 9

Extraction of NC1π^0Signal Events

Candidate events were selected for the data taken with the detector and the event samples from the simulation as described in Chapter 6. Candidate events are selected if they pass all cuts described in Chapter 8 and if they have an invariant mass less than 500 MeV/c^2. The invariant mass calculated from the energy and direction of the two reconstructed EM PIDs according to Equation 9.1.

$$M_{\gamma\gamma} = \sqrt{2E_{\gamma_1}E_{\gamma_2}(1-\cos(\theta_{\gamma\gamma}))} \tag{9.1}$$

Table 9.1 shows the total number of selected NC1π^0 candidates passing each analysis cut, along with the expectation from the simulation and the ratio of the number of events passing each cut. The number of expected signal events passing each cut is also shown. We do not make a comparison of the number of total events since the simulation does not include neutrino interactions happening outside of the magnet so that the samples are not expected to agree.

Table 9.2 shows a breakdown of the number of events passing all cuts. To normalize the MC to the data, we use the relative POTs listed in Table 6.1 and Table 6.2. In addition, since the mass of the PØD in the MC is larger than the measured value, we scale down the number of MC events by the correction factor listed in Chapter 10. Lastly we apply the 11av1(11av2) flux reweighting on the true neutrino energy of the event.

9.1 Signal and Background from MC

The MC for the combined Run I and Run II analysis predicts 143.6 $\pm$ 2.8 (stat) total events passing all selection cuts, with 79.1 $\pm$ 2.1 (stat) signal NC1π^0 events and 64.5 $\pm$ 1.9 (stat) background events. The predicted

Table 9.1: The number of events passing each cut. The first column gives the number of events found in the detector. The second and third column give the number of events predicted by the simulation and the number of expected signal events. The ratio (or relative efficiency) between cuts is also given.

Cut	Events	Rel. Eff.	Expected	Rel. Eff.	Signal	Rel. Eff.
Preselected	415750	n/a	187951.3 ± 102.4	n/a	4569.1 ± 16.1	n/a
Fiducial	51736	0.12	49833.2 ± 55.1	0.27	1716.1 ± 10.3	0.38
EM-Like	11170	0.22	11757.3 ± 25.9	0.24	1185.5 ± 8.0	0.69
Two 3D EM	2061	0.18	2357.1 ± 11.8	0.20	399.0 ± 4.7	0.34
No Muon Decay	1536	0.75	1723.0 ± 10.3	0.73	387.9 ± 4.6	0.97
Pi0 Direction	693	0.45	867.0 ± 7.7	0.50	250.4 ± 3.7	0.65
EM-Like Showers	312	0.45	390.2 ± 4.6	0.45	166.7 ± 3.0	0.67
Shower Distance	115	0.37	143.6 ± 2.8	0.37	79.1 ± 2.1	0.47

Table 9.2: A summary of the events selected by the cuts. The number of expected events is broken down into the contributions from signal and background. The background is further subdivided by the event category.

	Totals		
Detected	115		
Expected	143.6 ± 2.8		
Signal		79.1 ± 2.1	
Background		64.5 ± 1.9	
Charge Current		40.0 ± 1.5	
Muon			12.2 ± 0.8
Muon + π^0			7.4 ± 0.6
Muon + $\pi^\pm$			11.4 ± 0.8
Muon + other			9.0 ± 0.7
Neutral current		19.8 ± 1.0	
Other			16.5 ± 0.9
$\pi^\pm$			3.3 ± 0.4
Other		4.6 ± 0.5	

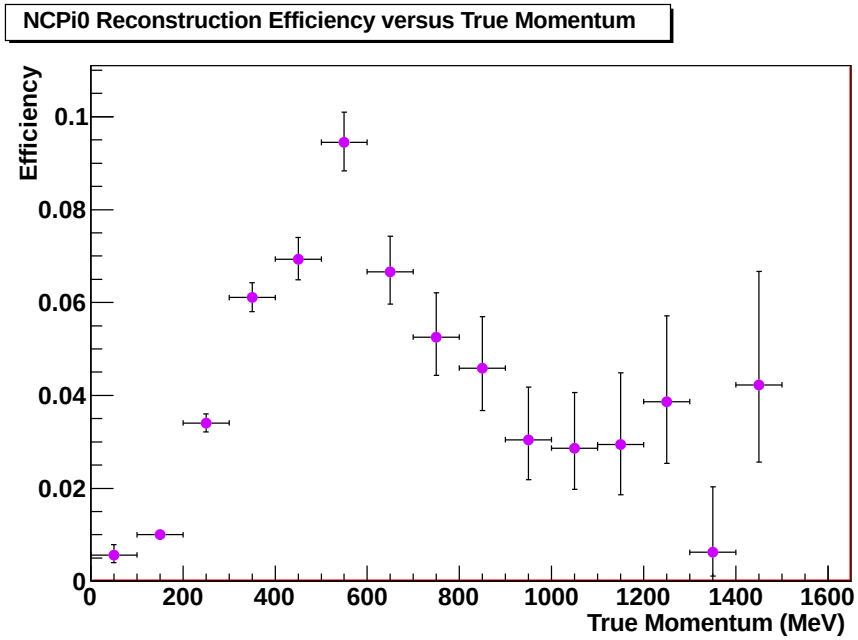

Figure 9.1: The NC1π^0 reconstrucion efficiency as a function of π^0 momentum

reconstruction efficiency is for Run I and Run II combined is 3.6%. The efficiency vs. momentum is shown in Figure 9.1.

9.2 Results from Data

We observe 115 events with an invariant mass below 500 MeV/c^2 and passing all selection cuts. The number of π^0 candidate events versus the accumulated POT is shown in Figure 9.2. The timing distribution of the saved events in the beam is given by Figure 9.3, and shows the events to be within the 6-8 bunch beam structure. The vertex distribution of saved events is shown in Figures 9.5 and 9.4. Figure 9.6 shows the reconstructed energy distribution of the candidate events overlayed with the MC prediction.

To extract the total number of signal events we use the RooFit package [77] to perform an extended likelihood fit to the invariant mass distribution. The shapes of the invariant mass distributions are shown in Figure 9.7, for signal and background. These are used as the shape pdfs in the fit. The normalization term in the fit is automatically constructed in RooFit by using the RooExtendPdf class. We include the systematic terms in the fit from the neutrino interaction cross section uncertainties and the absolute energy scale uncertainty. To include the energy scale uncertainty, we allow the value to float in the fit, essentially re-scaling the invariant mass of the pdf. We apply Gaussian constraints to these terms, with their nominal value as the Gaussian

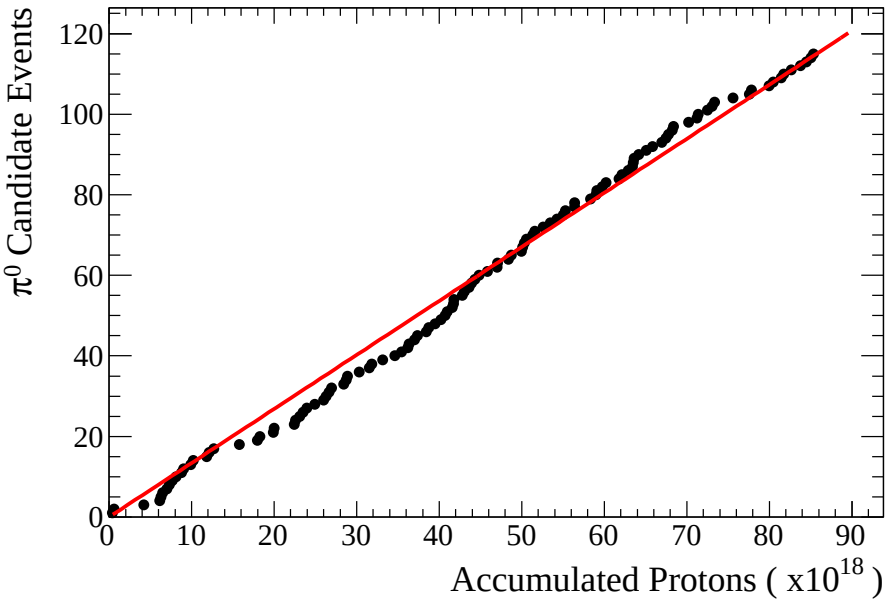

Figure 9.2: The number of π^0 candidate events vs. the accumulated pot. The black points are the events observed in data. The red line is the best fit line to the data through the origin. The slope of the best fit line is 1.34 events/(10^{18} POT). A KS test of the distribution gives a p-value of 0.94.

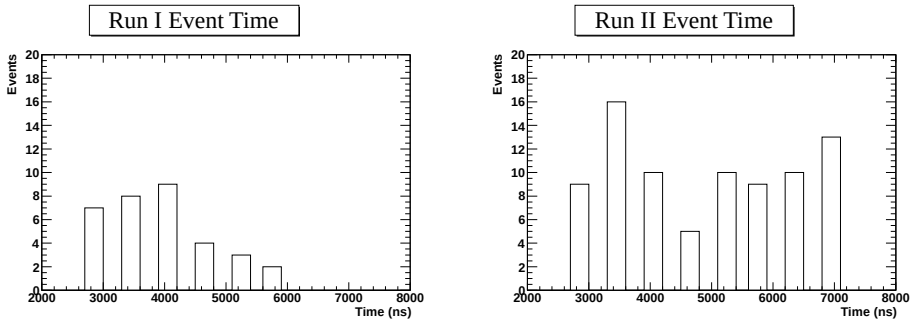

Figure 9.3: The timing of events passing all selection cuts. Left: Run I. Right Run II.

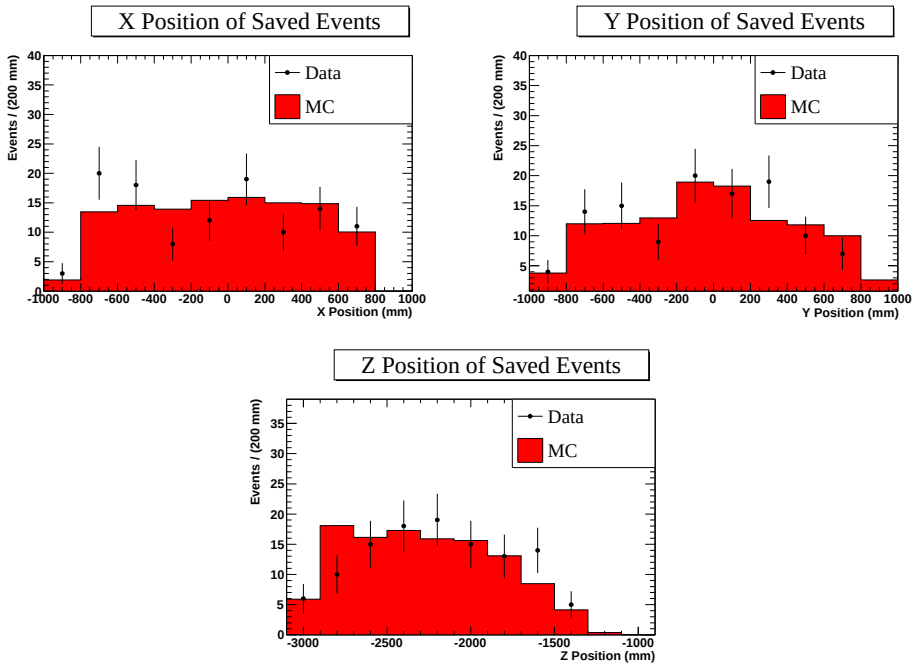

Figure 9.4: Reconstructed vertex position of events passing all selection cuts.

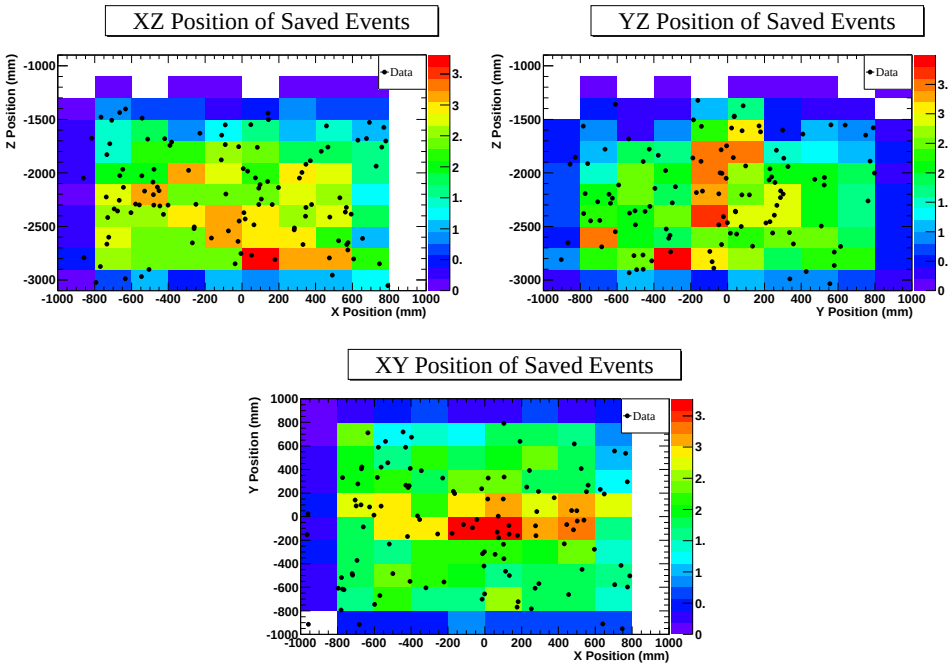

Figure 9.5: Reconstructed vertex position of events passing all selection cuts

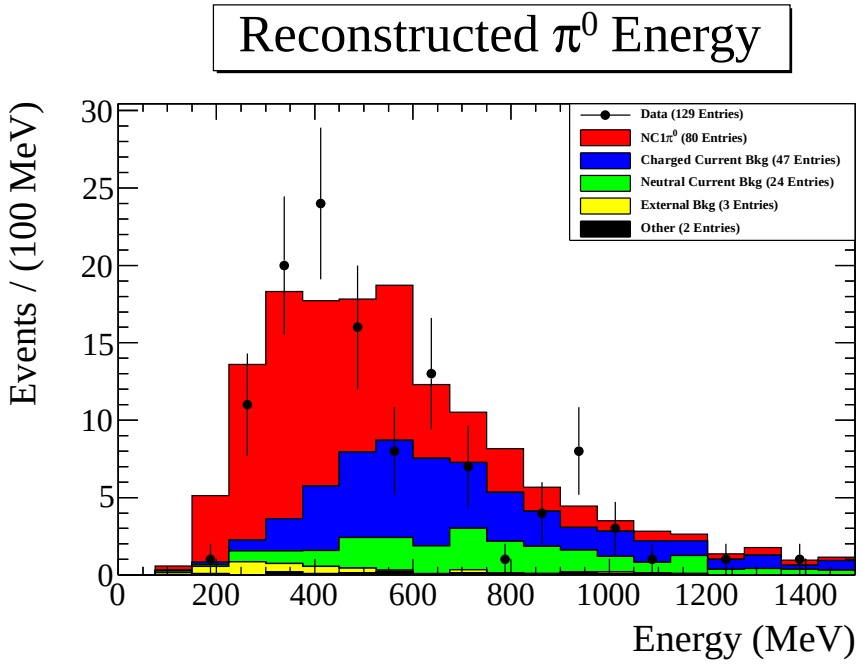

Figure 9.6: The reconstructed π^0 energy for events passing all selection cuts

mean, and the quoted uncertainty as the sigma. The total likelihood function is the product of all the individual terms and is shown in Equation 9.2. An unbinned fit to the data is performed to avoid biases with the choice of binning.

The results of the fit are shown in Figure 9.8. The fitting code fits the number of signal and background events between 0 and 500 MeV/c^2. The resulting ratio in the number of signal events is then calculated from the fitted events in the full range divided by the expectation from the simulation. As a cross check we calculate the number of events within an invariant mass window of 95 and 175 MeV/c^2. To determine the limits of the window, we fit the signal distribution in Figure 9.7 with a Gaussian function. Since the distribution is not actually Gaussian, the values of the fitted width vary between 36 and 42 MeV/c^2 depending on the range of the fit. For this reason, 40 MeV/c^2 is chosen as the width. To calculate the number of events in the window, we integrate the fitted signal shape within the limits. Multiplying this quantity by the total number of fitted signal events gives the number of signal events occuring in the window. The errors are calculated by RooFit, by linearly propagating the errors using the correlation matrix from the fit. Table 9.3 shows the correlation matrix. The correlation matrix shows a strong correlation between signal and background, which can be seen by the 1σ error elipse shown in Figure 9.9. Figure 9.10 shows the likelihood function as

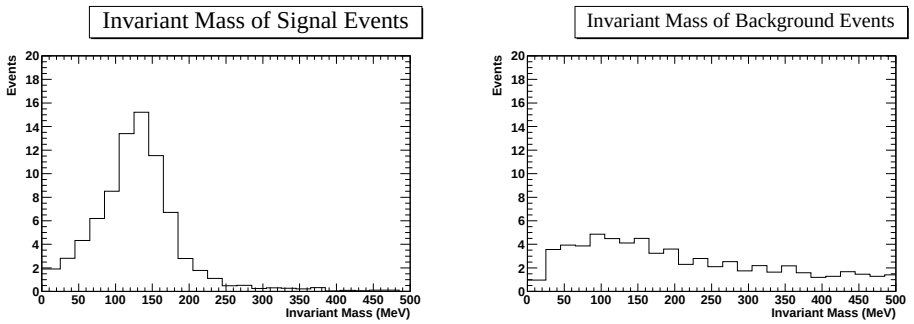

Figure 9.7: Reconstructed invariant mass for signal (left) and background (right)

Table 9.3: The Global Correlation Matrix

	Scale	Background	Signal
Scale	1.000	0.095	-0.094
Background	0.095	1.000	-0.591
Signal	-0.094	-0.591	1.000

a function of the fitting parameter when the other fitting parameters are at their best fit value. Table 9.4 summarizes the observed and expected events along with the corresponding ratios for both the full invariant mass range and the 95 to 175 MeV/c^2 window. The value of the energy scale at the best fit point is 0.94 ± 0.03. This indicates that the energy scale in data is larger than the MC by 6%.

$$L_{\text{Total}} = L_{\text{EScale}} \times L(\text{nbkg})_{\text{Xsec}} \times L(\text{nsig}, \text{nbkg})_{\text{Extended}} \tag{9.2}$$

Table 9.4: Summary of the number of observed and expected events along with the ratio for both the full invariant mass range and the 95 to 175 MeV window.

	0 - 500 MeV			95 - 175 MeV		
	Observed	Expected	Ratio	Observed	Expected	Ratio
Signal	66 ± 13	79 ± 2	0.84 ± 0.16	39 ± 6	49 ± 2	0.78 ± 0.12
Background	52 ± 10	65 ± 2	0.80 ± 0.16	14 ± 2	17 ± 1	0.83 ± 0.14

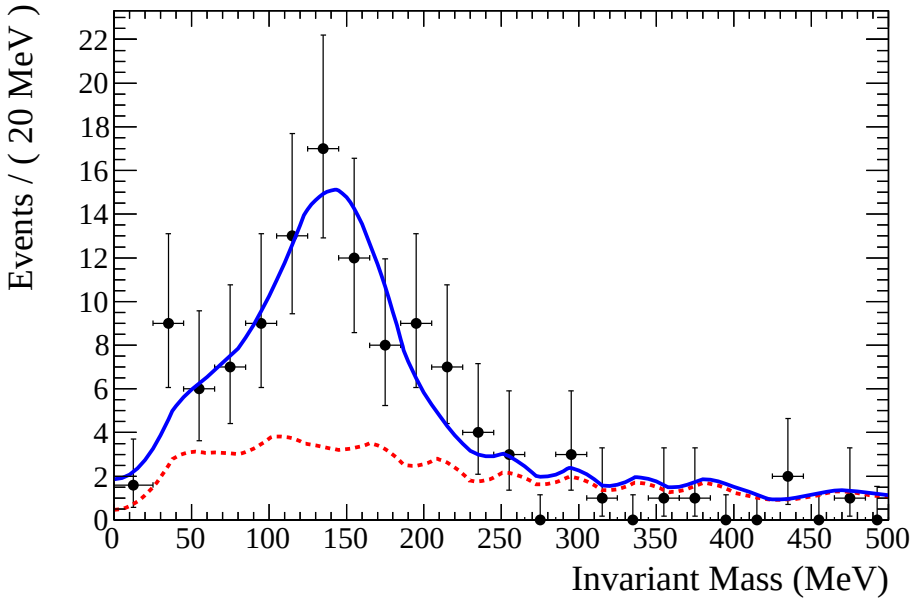

Figure 9.8: The result of the fit to the invariant mass distribution. The red dashed curve is the fit of the backround distribution. The blue curve is the signal + background.

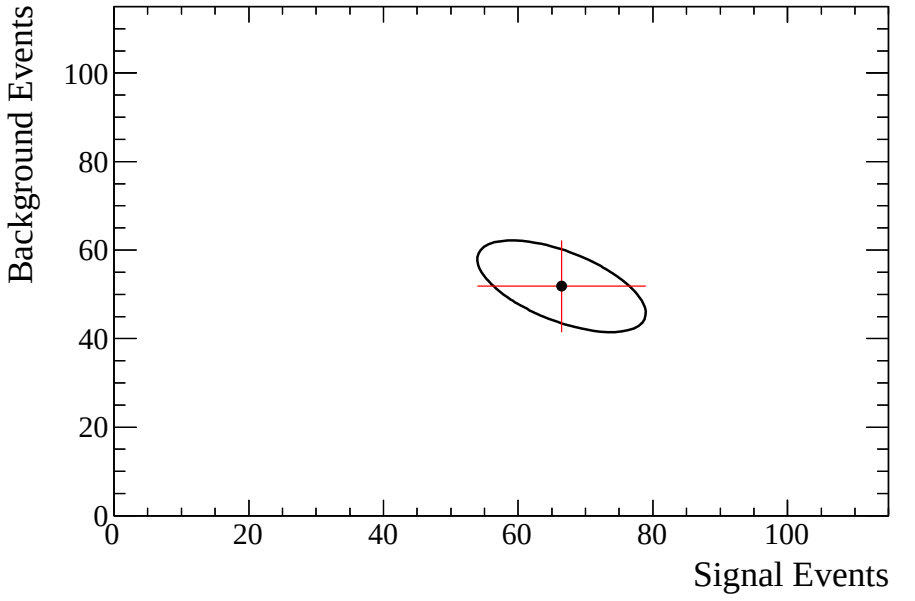

Figure 9.9: The contour plot showing the signal and background correlation. The black curve is the 1σ error elipse. The black dot is the best fit point.

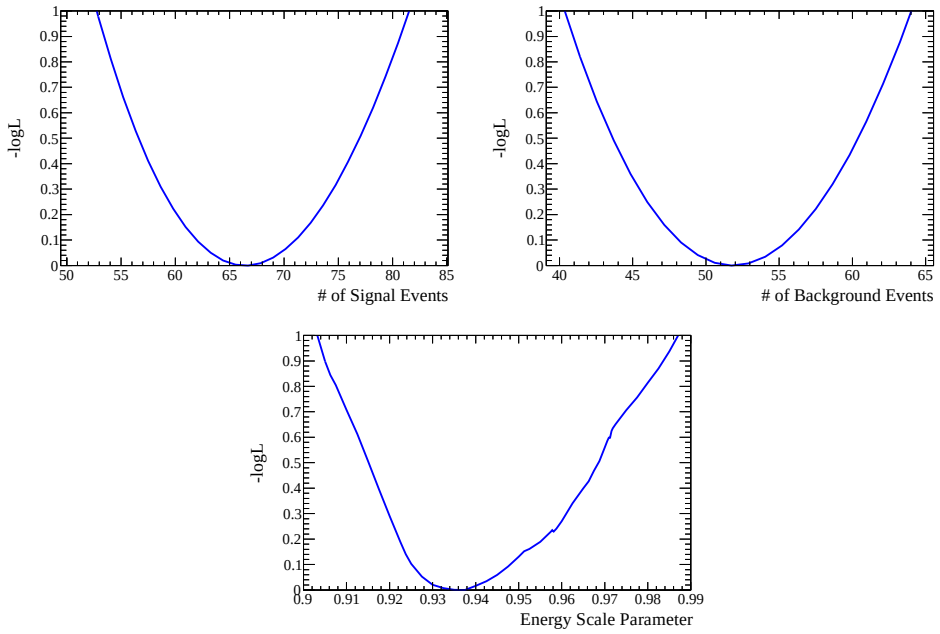

Figure 9.10: Values of the likelihood function vs. the fitting parameter. Top left shows the likelihood function vs the value of the signal, top right shows the same for the background, the central plots shows the likelihood vs the energy scale parameter. In each plot, the values of the other parameters are at their best fit value in the likelihood.

Table 9.5: Relative fractions of the NEUT codes making up the background events passing and failing the muon decay cut

Mode	Pass(%)	Fail(%)
CCQE	12	6
CC$\pi^{(\pm,0)}$	42	47
CC Other	13	21
NC$\pi^{(\pm,0)}$	8	7
NC Other	25	19

9.3 Sideband Cross Check Using Muon Decay Cut

This section describes a method of cross checking the expected invariant mass shape of background events. The muon decay cut provides a sample of event that is expected to contain mostly background, with only 3 events expected to come from signal. We therefore perform the same analysis on events failing the muon decay cut and compare the results. Figure 9.11 shows the comparison between the expected shape from the MC and the data shape. The MC distribution has been scaled by the number of events in data. Next, we compare the event classes of events passing and failing the cut. Table 9.5 shows the relative percentages of the event classes making up the Pass and Fail distributions. Because the largest discrepancy between the Pass and Fail distributions is of a few percent, we consider the event classes to have similar particle contents and therefore expect the two distributions to have similar mass shapes. To see this, we next compare the expected invariant mass distribution of background events passing and failing the muon decay cut shown in Figure 9.12. We see that there is reasonable agreement in the shapes, and so conclude that the MC is correctly predicting the shape of the invariant mass distribution of background events making it in the final sample. To complete the cross check we perform the same fit described above. The results of the fit are shown in Figure 9.13. The fitted parameters are shown in Table 9.6 and are consistent with the overall fit results. We observe 0 ± 4 events, consistent with the expectation from MC. We apply the 4 event uncertainty as an estimate of the shape uncertainty. This is described further in Chapter 10.

9.4 Results with 11av2 Flux Tuning

The analysis described above was done using the JNUBEAM 11a flux and the 11av1 flux tuning which incorporates the same hadron tuning used for

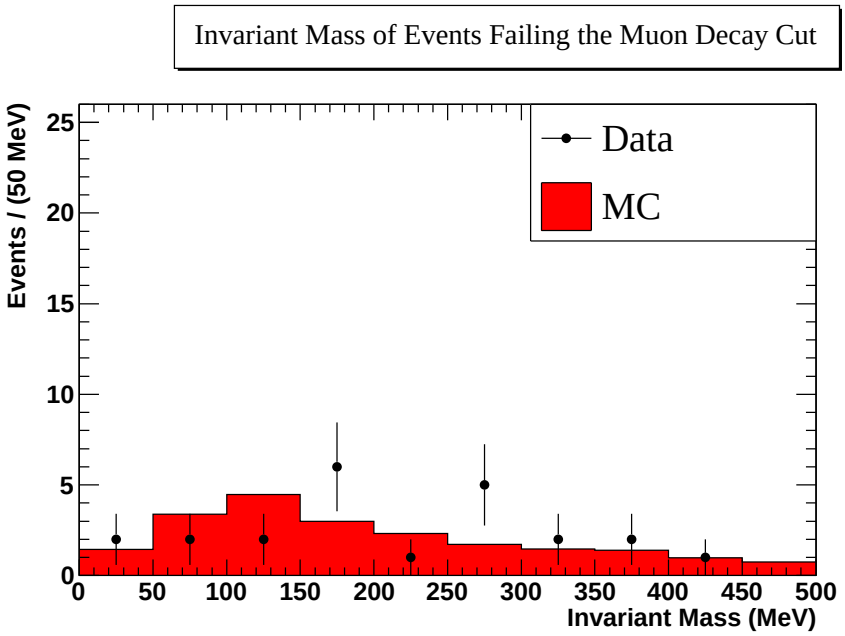

Figure 9.11: Invariant mass of events failing the muon decay cut for MC and data. The MC distribution has been scaled by the number of data events. The χ^2 test of the two distributions is 11.3 for 9 d.o.f., with a p-value of 0.25

Table 9.6: Results of the extended likelihood fit of events failing the muon decay cut

Parameter	Best Fit	Uncertainty
Scale	1.00	0.07
Signal	0	4
Background	23	3

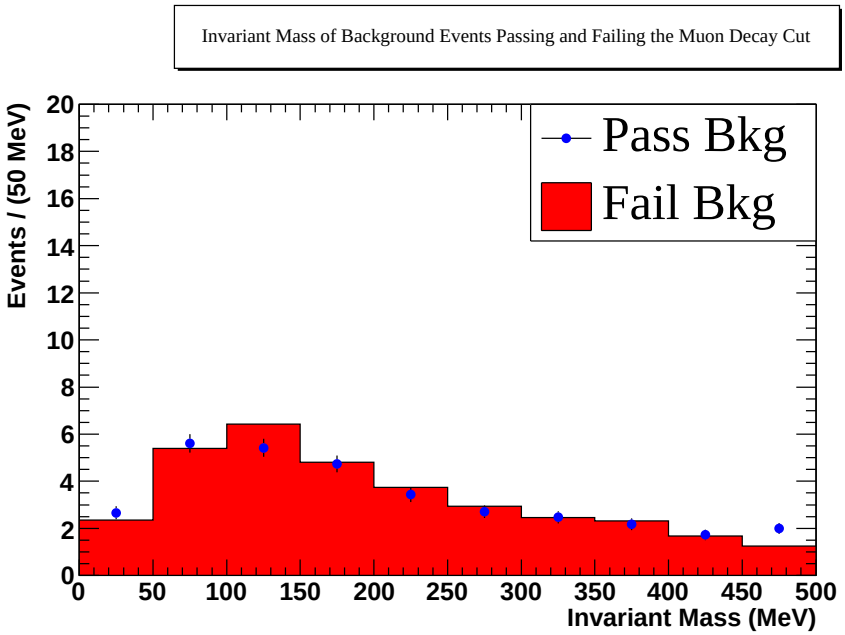

Figure 9.12: Invariant mass of background events passing and failing the muon decay cut. The Pass distribution has been scaled by the number of Failed events. The χ^2 test of the two distributions is 7.7 for 9 d.o.f., with a p-value of 0.56

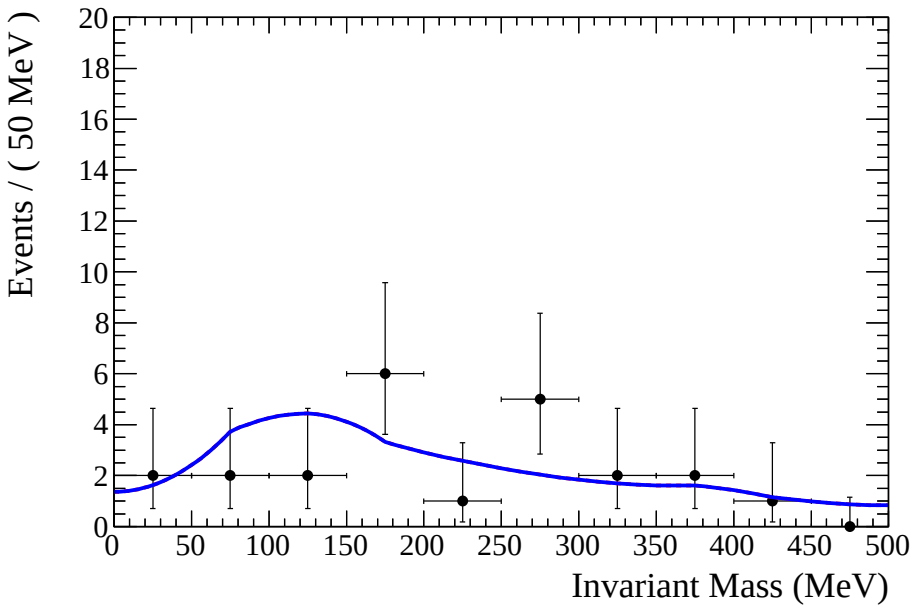

Figure 9.13: Fit of the invariant mass distribution for events failing the muon decay cut

the 2010 oscillation analysis. We now perform the analysis using the 11av2 flux tuning. This flux tuning incorporates kaon tuning from the NA61 experiment along with data from other experiments for the kaons not studied by NA61. The results are shown in Table 9.7 for the signal and background events. The best fit value of the energy scale is again 0.94 ± 0.03.

Table 9.7: Summary of the number of observed and expected events along with the ratio for both the full invariant mass range and the 95 to 175 MeV window using 11av2 flux tuning

	0 - 500 MeV			95 - 175 MeV		
	Observed	Expected	Ratio	Observed	Expected	Ratio
Signal	67 ± 13	82 ± 2	0.81 ± 0.15	39 ± 6	51 ± 2	0.76 ± 0.12
Background	52 ± 10	67 ± 2	0.78 ± 0.16	14 ± 2	17 ± 1	0.80 ± 0.14

Chapter 10

Systematic Uncertainty

10.1 EM Energy Scale

The electromagnetic energy of a reconstructed EM-like particle is described in Chapter 7 and depends on the amount of charge deposited in the detector relative to a MIP. The systematic uncertainty in this charge ratio is the EM energy scale systematic which will in turn affect the number of saved π^0 candidates in the final sample.

Two areas of potential disagreement between data and MC were identified: differences between the simulated and real geometries, and differences in the MPPC response to varied light levels. Both areas were studied with the same methodology. First, the MC was varied within the uncertainty, and used to generate through-going muons and mono-energetic photons. The simulation was re-calibrated using the muon sample, tuning the light of the bar to a constant level. The photons were then passed through the PØD reconstruction, and the variation in the shower energy was studied for successfully reconstructed events.

10.1.1 Material Mass and Density Uncertainty

For the geometry, the largest errors come from uncertainties in absorber materials. For two such materials, the brass in the water targets and the TiO_2 coating on the scintillator bars, there is a known discrepancy between the data and the simulation. For these materials, the thickness discrepancy was studied by adjusting the simulated material density. For example, the brass was simulated with a thickness of 1.5 mm while later measurements found a thickness of 1.26 mm. This discrepancy was studied by adjusting the normal value of the brass density from 8.5 g/cm to 7.14 g/cm. The nominal density of each material in the detector simulation was then varied over the range of common alloys (for brass, steel, and lead), or over the known uncertainty in the material composition (the TiO_2). The variations used are listed in Table 10.1.

Table 10.1: Variation of geometry parameters to study the effect on the energy scale. The first column gives the material that was varied, the second column is the default value in the simulation, the third and fourth column give the range of values studied.

Material	Default	Minimum	Maximum
Brass	8.500 g/cm^2	6.671 g/cm^2	7.277 g/cm^2
Steel	8.000 g/cm^2	7.725 g/cm^2	8.275 g/cm^2
Lead	11.350 g/cm^2	11.297 g/cm^2	11.403 g/cm^2
TiO_2	0.10 mm	0.17 mm	0.24 mm

Table 10.2: Variation of energy scale, for different geometry and MPPC sensor configurations. The first column gives the parameter.

	50 MeV %	100 MeV %	200 MeV %	500 MeV %
Brass				
shift -1σ	0.63 ± 1.67	3.16 ± 0.52	4.40 ± 0.53	4.46 ± 0.36
shift $+1\sigma$	1.59 ± 1.70	2.61 ± 0.53	2.80 ± 0.53	2.92 ± 0.36
Steel				
shift -1σ	1.18 ± 1.78	0.44 ± 0.54	-0.17 ± 0.54	1.23 ± 0.35
shift $+1\sigma$	-2.10 ± 1.76	-0.20 ± 0.54	-0.06 ± 0.53	0.57 ± 0.36
Lead				
shift -1σ	-0.65 ± 1.69	0.29 ± 0.54	0.47 ± 0.55	0.77 ± 0.37
shift $+1\sigma$	-0.10 ± 1.81	0.65 ± 0.54	1.15 ± 0.53	0.81 ± 0.36
TiO_2				
shift -1σ	-2.68 ± 1.91	-0.35 ± 0.54	-0.35 ± 0.54	0.26 ± 0.37
shift $+1\sigma$	4.31 ± 1.91	1.07 ± 0.55	0.61 ± 0.53	0.88 ± 0.37
Light Model				
$\sigma = 0.20$ mm	0.46 ± 1.52	-1.58 ± 0.37	-2.72 ± 0.24	-4.26 ± 0.20
$\sigma = 0.25$ mm	2.49 ± 1.43	-1.05 ± 0.43	-1.54 ± 0.26	-2.53 ± 0.17
$\sigma = 0.30$ mm	2.51 ± 1.52	0.66 ± 0.42	-0.11 ± 0.25	-1.02 ± 0.19
P.D.E.				
0.13	3.25 ± 1.60	0.48 ± 0.44	1.14 ± 0.26	0.89 ± 0.19
0.26	2.74 ± 1.25	-0.99 ± 0.39	-1.07 ± 0.25	-1.09 ± 0.18
0.39	6.77 ± 1.26	5.29 ± 0.42	5.11 ± 0.26	4.71 ± 0.19

Table 10.3: The assigned systematic error due to the electromagnetic scale uncertainties. The middle column gives the expected shift of the detector EM scale relative to the simulation, and the last column gives the assigned systematic error about the shifted mean. The final row gives the total shift and systematic for the electro-magnetic energy scale.

	Systematic Shift	Systematic Uncertainty
Brass	n/a ± n/a	0.65 ± 0.22
Steel	n/a ± n/a	0.29 ± 0.23
Lead	n/a ± n/a	0.14 ± 0.14
TiO_2	n/a ± n/a	0.50 ± 0.44
Material Modeling Shift	6.80 ± 0.27	0.31 ± neg.
Light Model	- 0.66 ± 1.53	1.27 ± 1.13
PDE	1.61 ± 0.64	5.65 ± 0.96
Total	7.76 ± n/a	6.21 ± n/a

10.1.2 MPPC Modeling

Two aspects of the model were investigated: the photon detection efficiency (PDE) of the MPPC, and the distribution of light leaving the fibre and falling on the MPPC. From recent studies the best fit value of the PDE was determined to be 0.26 ± 13 [78], so the model was varied within that range. The MC light distribution model for production 4 was a flat, uniform distribution. The new model of a Gaussian distribution about the center of the MPPC was studied in comparison, with width $\sigma = 0.25 \pm 0.05$ mm.

Table 10.2 shows the shift (and error on that shift) in the energy scale when each parameter is varied up and down by 1σ.

10.1.3 Total EM scale uncertainty

The total EM scale uncertainty has two components summarized in Table 10.3. The first component is the effect of known differences between the detector and the simulated detector geometry. This accounts for an expected 7.76% shift between the detector and simulation and is applied as a correction to the energy estimator. The second component is the uncertainty on the simulation energy scale. This accounts for a 6.21% uncertainty in the EM energy scale relative to the MIP energy scale which will be added in quadrature to the uncertainty in the MIP energy scale.

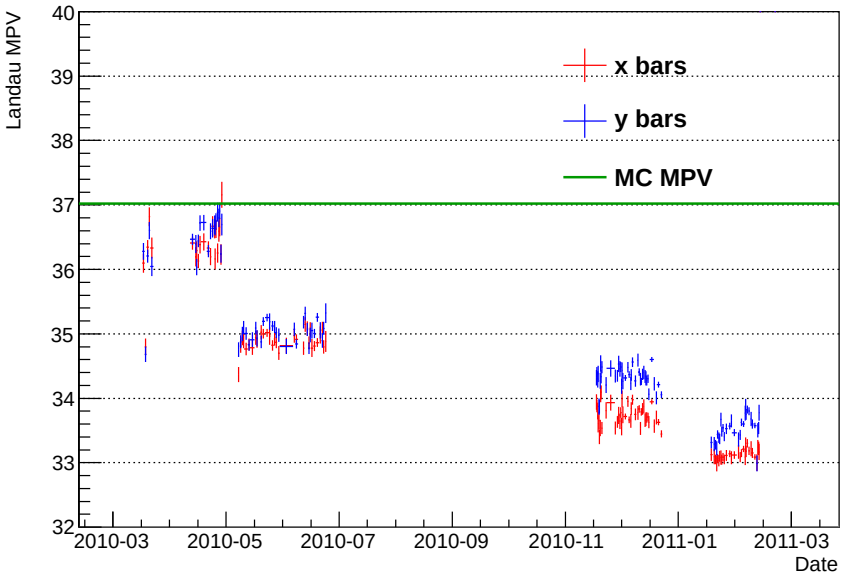

Figure 10.1: Through-going sand muon MPV as a function of time. The value for x bars is shown in red, and for y bars is shown in blue. The green line shows the corresponding value for Monte Carlo.

10.2 Absolute Energy Scale

10.2.1 Variation in PØD Response with Time

The calibration of the MIP light yield described in Section 3.6.2 is not constant in time as shown in Figure 10.1. The change over time can be understood in terms of changes to the detector and detector environment. On May 2010, there was a tuning of the overvoltage. Between June 2010 and November 2010, the temperature in the detector hall changed due to the seasonal change. Finally, in January 2011, there was a further tuning of the overvoltage. As a result of these changes, the calibration procedure was performed over the course of the data-taking period using through-going muons. Figure 10.1 shows the MPV of the landau-gaussian fit as a function of time. Table 10.4 shows the correction constants that are applied to energy reconstruction in data. After these correction constants have been applied, there is some residual width as shown in Figure 10.3. The systematic uncertainty therefore determined to be the width of this distribution, 3%.

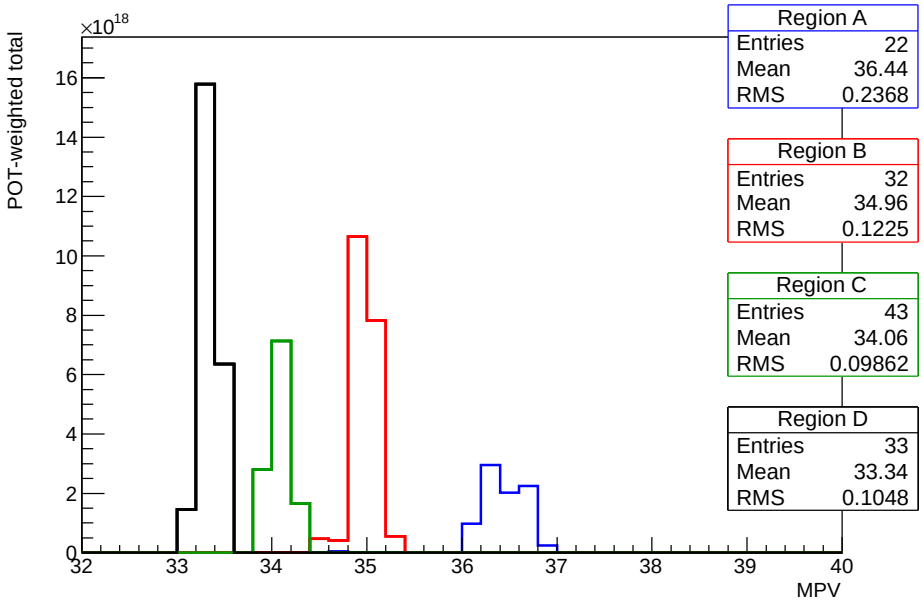

Figure 10.2: Response histograms for each of the four time periods that can be seen in Figure 10.1. Each entry in the histogram is weighted by the POT for the contributing runs. The mean of each histogram is used to derive the calibration constant for the time period.

Table 10.4: Time periods and their associated calibration constants.

Region	Time	Constant
A	Mar '10 - May '10	1.016
B	May '10 - Jun '10	1.059
C	Nov '10 - Jan '11	1.087
D	Jan '11 - Feb '11	1.111

Table 10.5: A summary of the uncertainties contributing to the total energy scale uncertainty.

Time Variation	3%
Electro-magnetic Scale	6.2%
Total	6.9%

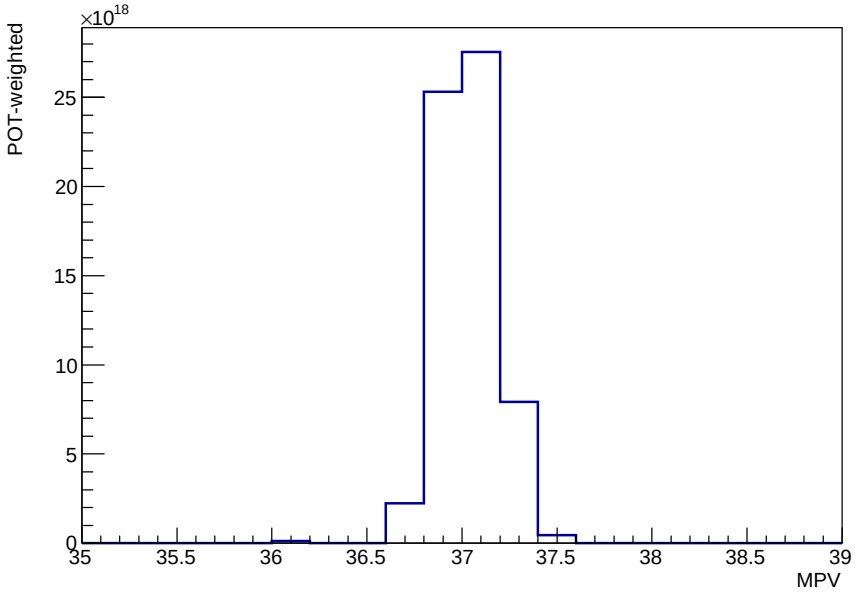

Figure 10.3: Through-going sand muon responses after correction by the factors shown in Table 10.4, with each entry weighted by POT.

10.2.2 Total Energy Scale Uncertainty

The absolute energy scale uncertainty is found by adding the contributions to the MIP energy scale and relative EM energy scale in quadrature. The individual values are summarized in Table 10.5 and give a total systematic uncertainty in the energy scale of 6.9%. In addition, as summarized in Section 10.1.3, there is a 7.8% shift between data and MC. The shift is applied to the energy reconstruction in data. The systematic is included in the fit.

10.3 PØD Detector Mass

Different calculations were performed for the fiducial mass in Run 1 and Run 2. These two calculations agree within error bars of each other and we assume that the fiducial mass should not change from one run to the next. Since there is a greater confidence in the fiducial mass calculation for Run 2, we accept it as the as-built mass. The PØD has a fiducial mass of 5454 ± 40 kg from Run 2. This mass was determined from measurements detailed in a separate technical note [79]. The geometry file has a fiducial mass of $5634.21 \pm 0.54(stat) \pm 5.63(sys)$ kg. From these values, the correction factor for the mass is $3.18 \pm 0.71(stat) \pm 0.10(sys)\%$. This correction factor is applied as a reweighting factor of the simulated events as described in Chapter 9; the

error on this factor is incorporated into the overall systematic errors.

10.4 PØD Detector Alignment

Monte Carlo studies were performed to find the minimum resolution of the PØD as well as the accuracy of the current alignment procedure. In particular, the resolution of a hit reconstructed from two hits in adjacent bars was studied. Due to the geometry of the detector, when a track passes through a layer, it will most likely leave two hits in adjacent bars. The resolution of the PØD for this configuration is 2.51 ± 0.02 mm for the x layers and 2.43 ± 0.02 mm for the y layers. The accuracy for the layer-by-layer alignment process was determined to be 0.5 mm, far better than the detector resolution. The unaligned detector has a layer-by-layer variation of ± 2.5 mm. Due to the fact that the detector in situ is aligned to the point of its resolution and the reconstruction parameters are varied sufficiently to cover any alignment uncertainty, the alignment systematic uncertainty is not covered by a separate systematic error.

10.5 PØD Fiducial Volume

The systematic errors associated with the fiducial volume are comprised of two separate effects: the first effect is a possible vertex position bias in the detector, the second is due to the stability of the result to the fiducial volume cut position itself. These effects combined resulted in a systematic error of 7%.

The position of the reconstructed vertex was studied for both the data and simulation to see if there was a vertex bias effect between the two. We studied the shapes of the vertex distribution within the fiducial volume by looking at the number of vertices within each section of the fiducial volume. Starting at the center, steps of 10 cm are taken in the x, y, and z directions and studied independently. Because the detector is symmetric, only the distance from the center is considered so that events in the positive and negative x and y directions are added to increase statistics. For the z direction, because of the low acceptance, the 5 most downstream 10 cm sections of the PØD are not considered.

For each dimension, a linear fit was applied to the data, and the number of events within the vertex resolution for x, y, and z, (see Table 7.1) of the end of the detector was calculated for both the data and simulation. The difference in the number of vertices within these volumes was then divided by the events from the simulation to give the systematic error. Through this method the errors were found to be: $1.73 \pm 0.1\%$ for x, $1.05 \pm 0.3\%$ for y, and $3.84 \pm 0.09\%$ for z. All together, these give a vertex position systematic error of $4.34 \pm 0.4\%$.

Table 10.6: Cross section uncertainties for a variety of interaction modes

Neutrino Interaction	Uncertainty
CC1π	$\pm$30%
CC Coh.	$\pm$100%
CC Other	$\pm$30%
NC1π^0	$\pm$30%
NC Coh.	$\pm$30%
NC Other	$\pm$30%

The effect of the fiducial volume cuts on the reconstruction was studied to understand the inherent systematic error introduced by the cut. To do so, we performed the event selection with several different choices of fiducial boundaries. The size of the fiducial volume was increased and decreased about their nominal values shown in Table 8.1. The x and y dimensions were varied together in 7 cm steps, while the upstream and downstream z boundaries were varied independently in steps of 10 cm. The ratio of the number of vertices within the fiducial volume in the data relative to the simulation was calculated and from this the ratio of the fraction at the changed fiducial volume to the original fiducial volume was calculated. The systematic uncertainty is defined as the maximum deviation of this ratio at one vertex resolution step from nominal. For x and y the error was found to be $2.54 \pm 2\%$. For upstream and downstream z, the error was found to be $2.34 \pm 3\%$ and $1.36 \pm 1\%$, respectively. Combined, the total systematic error from the fiducial volume cut is $3.72 \pm 4\%$.

Combining the two sources of fiducial volume systematic error in quadrature results in a final uncertainty of $5.72 \pm 4\%$. Since the uncertainty is significant, it is added in quadrature to give a total systematic error of 7%.

10.6 Simulation Uncertainties

The simulation was described in Chapter 5. Three possible systematic errors associated with this simulation are considered in this analysis. The first is the systematic error due to NEUT cross section uncertainties, the second is the error due to final-state interaction effects, and the last is the error due to uncertainties in the beam flux.

10.6.1 Neutrino Cross Section Uncertainties

In T2K the Neutrino Interactions Working Group (NIWG) has summarized the uncertainties associated with the NEUT generator for the various

analyses [80]. The cross section uncertainties for energies below 2 GeV are shown in Table 10.6. The cross section uncertainties at higher energies are not considered. The uncertainties have been incorporated into the extended likelihood fit as described in Chapter 9.

10.6.2 Beam Uncertainties

The beam simulation was described in Chapter 5. In T2K there is a dedicated beam group tasked with studying the sytematic uncertainties due to the beam flux. The following sources of uncertainty are considered:

- Uncertainty of the pion production multiplicity for both the primary and secondary interaction
- Uncertainty of the kaon production multiplicty for both the primary and secondary interaction
- Uncertainty of the interaction cross sections of $p, \pi^{\pm}, K^{\pm}$
- Off-axis angle uncertainty
- Uncertainty of the primary beam optics
- Horn alignment error
- Uncertainty of horn current
- Uncertainty of magnetic field distributions inside the horns

The effect of each source was studied to determine the systematic uncertainty of the number of near detector events for the T2K oscillation analyses. The total uncertainty was determined to be 15%, so that is the uncertainty used for this analysis.

To reduce these uncertainties on the beam flux we normalize by the CC inclusive measurement done by the T2K tracker [34]. The reduced beam flux uncertainty is then estimated from the uncertainty on the charged current inclusive measurement, Equation 4.3. For this analysis the statistical and systematic errors are added in quadrature giving a total uncertainty of 6.5%.

10.7 PØD Reconstruction Uncertainties

This section describes the method for estimating systematics coming from parameters in the PØD reconstruction algorithms. For this analysis, only reconstruction effects associated with the particle identification were investigated.

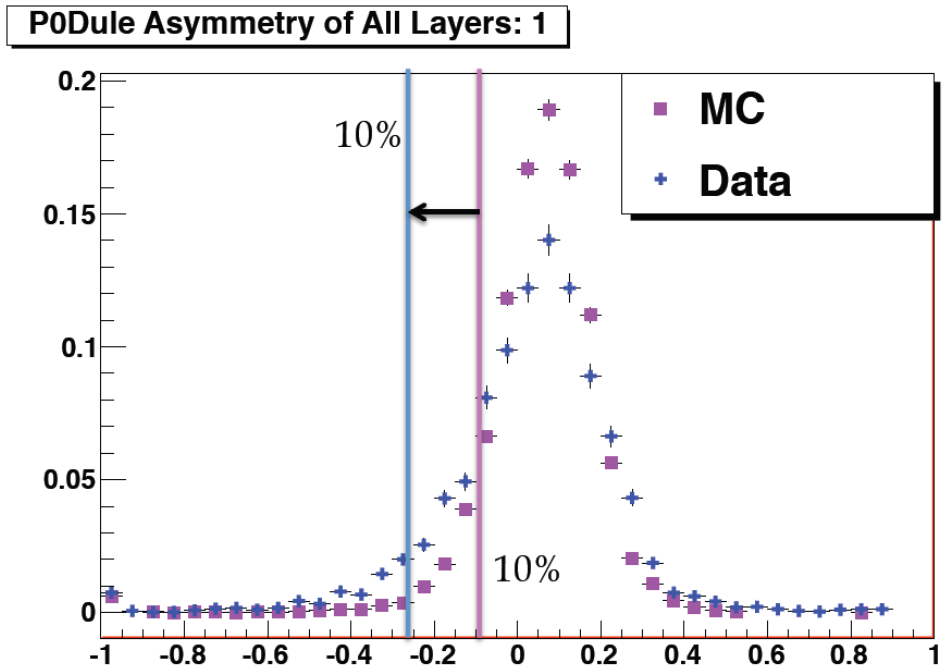

Figure 10.4: A example of the mapping procedure used to study the systematic uncertainty due to the reconstruction particle identification.

The particle identification systematic error compensates for the difference in efficiency of the PID on data and on Monte Carlo. To find this discrepancy, we made histograms for each PID parameter to study the distribution of the parameters in data and Monte Carlo. The histograms were constructed from events with stopping muons in the PØD. This sample is one of the easiest and cleanest to retrieve from data. Next, using the parameter histograms from data and Monte Carlo, a mapping was performed. The mapping takes a Monte Carlo parameter (i.e. 0.1), finds the cumulative probability (integral from -∞ to 0.1) of the associated Monte Carlo histogram, then finds the parameter with the same cumulative probability in the associated data histogram. In this way, the mapped parameter is at the same probability for data as it was originally in Monte Carlo. A visual example of this procedure is shown in Figure 10.4.

The NC1π^0 analysis looks for events that have only two EM particles and no light tracks (these are muons, pions, and others). At the tracking stage, the reconstruction gives an initial PID to each particle (kEM, kLightTrack, and kOther). Particles labeled EM or Other are then passed to the shower reconstruction. Two efficiencies were studied, the track identification and the event identification at the tracking level. This analysis required the final result to have one and only one vertex in the fiducial volume so as to match the NC1π^0 event selection.

Table 10.7: The number and percent of true tracks identified as EM or a light track (LT) for the default PID method and the mapped PID method compared to the true identity of the track is shown. In the second column, each row heading describes the truth information. For the Reconstruction information, the column headings across the top row describe the PID. The middle columns are the number of tracks identified as EM or LT organized in rows by the track's truth information. The last two columns show the percentage of tracks that are true EM tracks or not EM tracks organized in columns of the reconstructed PID.

	Recon / Truth	EM-Like (%)	LT-Like (%)
Default PID	EM	317820 (99.7)	1105 (0.3)
	Not EM	51079 (35.0)	95028 (65.0)
Mapped PID	EM	318739 (99.9)	195 (0.1)
	Not EM	73674 (50.4)	72433 (49.6)

10.7.1 Track PID Efficiency

For the track by track efficiency, the true identity of the track was decided by looking at the contribution to the total charge by EM and non-EM sources. If EM accounts for more than 90% of the total charge, then the particle is called a true EM particle. The value of 90% is used to ensure that the track is pure. As can be seen in Table 10.7, the track efficiency for finding a true EM particle is extremely good in both default and mapped cases. However, the efficiency for the light tracks is much worse. Table 10.7 also ignores the special cases of exiting muons and short tracks. These cases do not have PIDs computed.

10.7.2 Event PID Efficiency

For the event by event efficiency, the true identity of the track was decided by the same method explained above, except the charge contribution cut off is at 50%. As can be seen in Table 10.8, the PID loses 10% of the true only-EM events and gains less than 5% of the true events containing a light track. What is of particular importance is the true background of the reconstructed PID, the number of events reconstructed as only containing EM tracks that have non-EM truth normalized by all events reconstructed as EM only events. For the default PID, representing the Monte Carlo, the background is at 8.3% and for the mapped PID, representing the data, the background is at 13.0%.

Table 10.8: The number and percentage of true events identified as only containing EM particles or containing a light track (LT) for the default PID method and the mapped PID method is shown. For the second column, each row heading describes the truth information. For the reconstruction information, the column headings across the top row describes the PID. The middle columns are the number of events identified as only EM or containing a LT organized in rows by the event's truth information. The last two columns show the percentage of events that are truly EM or not organized in columns of the reconstructed event PID.

	Truth \ Recon	Only EM (%)	Contains LT (%)
Default PID	EM	267973 (91.0)	26594 (9.0)
	Not EM	24208 (3.0)	783222 (97.0)
Mapped PID	EM	268350 (91.1)	26217 (8.9)
	Not EM	39960 (4.9)	767470 (95.1)

The error on both of the previous numbers is negligible due to the nature and size of the sample. Thus, we find a systematic error of 4.7% due to the difference between data and Monte Carlo efficiencies of the PID.

10.8 Background Shape Uncertainty

The background shape uncertainty is the uncertainty due to the MC predicted shape of the invariant mass distribution of background events in the extended likelihood fit. This uncertainty is intended to cover effect associated with the uncertainties in the background invariant mass shape, including uncertainties due to final state interactions. To quantify this uncertainty, in Section 9 we performed a likelihood fit to determine the number of signal events in the background-enhanced sample of events failing the muon decay cut. The resulting fit of the signal was consistent with 0 events and had an uncertainty, σ_{Sig}, of 4 events. The quoted value of the uncertainty, σ_{Shape}, is then determined from

$$\sigma_{Shape} = \sigma_{Sig} \times \frac{N_{Fit}^{Bkg}}{N_{Side}^{Bkg}} \times \frac{1}{N_{Fit}^{Sig}} \tag{10.1}$$

where N_{Fit}^{Bkg} (52), is the number of observed background events in our final event sample, N_{Fit}^{Bkg} (23) is the number of observed background events in the

Table 10.9: Systematic Error Contributions to the Data/MC Ratio

Source	Error	Contribution to Ratio (%)
Mass Uncertainty	0.8%	0.8%
Detector Alignment	2.5 mm	$< 0.1\%$
Fiducial Volume	7%	7%
Flux Uncertainty	(15)6.5%	(15)6.5%
Reconstruction Uncertainties	4.7%	4.7%
Shape Uncertainty	13.7%	13.7%
Total	—	(22)17%

sideband and N_{Fig}^{Sig} (66) is the number of observed signal events in the final event sample. Inserting those values into the equations yields 13.7%. Because this uncertainty is dominated by the statistical fluctuation in the number of events in the side band, it is taken as uncorrelated with the other systematic uncertainties.

10.9 Summary of Systematic Uncertainties

The contribution of all sources of systematic error is shown in Table 10.9. The middle column shows the systematic uncertainty on each parameter and the final column shows the effect on the normalized (unnormalized) ratio of the observed number of NC1π^0 events to the number expected from the NEUT simulation.

Chapter 11

Results

Results of the measurement are shown in Table 11.1 for the 11av1 flux tuning and Table 11.2 for the 11av2 flux tuning. Note that the double ratio is not shown for 11av2 because the CC inclusive interaction cross section has not yet been measured with this flux tuning.

Table 11.1: Results with the 11av1 flux tuning.

Quantity	Value	Stat. Error	Sys. Error
$N^{Data}_{NC1\pi^0}/N^{MC}_{NC1\pi^0}$	0.84	0.16	0.18
$\frac{N^{Data}_{NC1\pi^0}/N^{Data}_{CC}}{N^{MC}_{NC1\pi^0}/N^{MC}_{CC}}$	0.81	0.15	0.14

Table 11.2: Results with the 11av2 flux tuning.

Quantity	Value	Stat. Error	Sys. Error
$N^{Data}_{NC1\pi^0}/N^{MC}_{NC1\pi^0}$	0.81	0.15	0.18

Chapter 12

Conclusion

The analysis presented in this thesis is a measurement of the neutral current single π^0 production cross section using the T2K π^0 detector. The data analyzed corresponds to 8.55×10^{19} POT of T2K's Run I and Run II data. We measure the ratio of the NC1π^0 cross section relative to the charged current inclusive interaction to be $0.81 \pm 0.15(stat.) \pm 0.14(sys.)$ times the value predicted by the NEUT simulation.

The T2K and the MINOS experiments recently have published results indicating that the value of θ_{13} may be larger than expected. For the T2K experiment, the measurement of θ_{13} is currently statistics-limited, as the integrated POT so far delivered amounts to less than 2% of T2K's stated goal. This is expected to change when T2K resumes data taking in March 2012. As a result, this will require a greater understanding of the systematic uncertainties associated with the ν_e appearance measurement.

To reduce the systematic uncertainty from the π^0 background at Super-Kamiokande, the PØD detector will have to measure the NC1π^0 production cross section on water. This will require roughly equal amounts of data-taking with the PØD water targets filled with water as well as with the PØD water targets emptied. This analysis was done using only data taken while the PØD was filled, however there is no reason why it would not be applicable to the data taken while the PØD was empty. And so, if nothing else, the work done in this thesis will provide future analyzers with the means to measure the on-water cross section once that data becomes available.

Bibliography

[1] H. Becquerel, "Sur les radiations mises par phosphorescence," *Comptes Rendus*, **122**, 501-503 (1896).

[2] E. Rutherford, *Philosophical Magazine*, Series 5, **47**, 284 (1899).

[3] P. Villard, "Sur la rflexion et la rfraction des rayons cathodiques et des rayons dviables du radium," *Comptes Rendus*, **130**, 1010-1012, (1900)

[4] W. Pauli, "Open Letter to the group of radioactive people at the Gauverein meeting in Tubingen."

[5] C. L. Cowan, Jr., F. Reines, F. B. Harrison, H. W. Kruse, A. D. McGuire, Science **124**, 103 (1956).

[6] G. Danby, J. M. Gaillard, K. Goulianos, L. M. Lederman, N. Mistry, M. Schwartz, J. Steinberger, Phys. Rev. Lett. **9**, 13 (1962).

[7] F. J. Hasert *et al.*, Phys. Lett. B **46**, 121 (1973).

[8] F. J. Hasert *et al.*, Phys. Lett. B **46**, 138 (1973).

[9] K. Kodama *et al.*, [The DONUT Collaboration], Phys. Lett. B **504**, 218 (2001).

[10] W. N. Cottingham and D. A. Greenwood, *An Introduction to the Standard Model of Particle Physics*, (Cambridge University Press, 1998)

[11] M. Goldhaber, L. Grodzins, A. W. Sunyar, Phys. Rev. **109**, 1015 (1958).

[12] K. Nakamura *et al.*, (Particle Data Group), J. Phys. G **37**, 075021 (2010).

[13] U. Seljak *et al.*, JCAP **0610**, 014 (2006).

[14] B. Pontecorvo, Sov. Phys. JETP **6**, 429 (1957). Sov. Phys. JETP **7** 172 (1958).

[15] Z. Maki *et al.*, Prog. Theor. Phys. **28**, 870 (1962).

[16] Y. Fukuda *et al.*, [The Super-Kamiokande Collaboration], Phys. Rev. Lett **81**, 1562 (1998).

[17] P. Adamson *et al.*, [The MINOS Collaboration], Phys. Rev. Lett. **106**, 181801 (2011).

[18] P. Adamson *et al.*, [The MINOS Collaboration], Phys. Rev. Lett. **107**, 181802 (2011).

[19] S. Yamamoto, *Search for ν_μ to ν_e Oscillation in a Long-baseline Accelerator Experiment*, PhD. Thesis, Kyoto University, June 2006.

[20] K. Abe *et al.*, [The T2K Collaboration], Nucl. Instrum. Meth. A **659**, 106 (2011).

[21] K. Matsuoka *et al.*, Nucl. Instrum. Meth. A **624**, 591 (2010).

[22] K. Abe *et al.*, [The T2K Collaboration], submitted to Nucl. Instrum. Meth A (2011), arXiv:1111.3119

[23] N. Abgrall *et al.*, Nucl. Instrum. Meth. A **637**, 25 (2011).

[24] Y. Fukuda *et al.*, [The Super-Kamiokande Collaboration], Nucl. Instrum. Meth. A **501**, 418 (2003).

[25] K. Abe. *et al.*, [The T2K Collaboration], Phys. Rev. Lett. **107**, 041801 (2011).

[26] K. Abe. *et al.*, [The T2K Collaboration], (2012) arXiv:1201.1386

[27] S. Assylbekov *et al.*, submitted to Nucl. Instrum. Meth A (2011) arXiv:1111.5030

[28] M. Yokoyama *et al.*, (2006) arXiv:physics/0605241

[29] M. Yokoyama *et al.*, Nucl. Instrum. Meth A **622**, 567 (2010).

[30] A. Vacheret, S. Greenwood, M. Noy, M. Raymond, A. Weber, in: Nuclear Science Symposium Conference Record, 2007. NSS '07. IEEE, Vol. 3, pp 1984-1991.

[31] The ND280 Calibration Group, *Calibration of the ND280 Scintillator Detectors*, (T2K Internal Note).

[32] L. P. Trung, *Event Reconstruction and Energy Calibration using Cosmic Muons for the T2K Pizero Detector*, PhD. Thesis, Stony Brook University, December 2009.

[33] S. Ritt, P. Amaudruz, K. Olchanski, MIDAS (Maximum Integration Data Acquisition System), 2001. http://midas.psi.ch.

[34] C. Giganti *et al.*, *Study of Neutrino Charged Current Interactions in the ND280 Tracker*, (T2K Internal Note).

[35] GEANT3, A detector description and simulation tool, 1993. Application Software Group, Computing and Networks Division, CERN, Geneva.

[36] FLUKA version 2008.3c, 2008. http://www.fluka.org/fluka.php.

[37] N. Abgrall *et al.*, [The NA61 Collaboration] Report from the NA61/SHINE Experiment at the CERN SPS, Technical Report CERN-SPSC-2010-025. SPSC-SR-066, CERN, Geneva, 2010.

[38] N. Abgrall *et al.*, [The NA61 Collaboration], Calibration and Analysis of the 2007 Data, CERN-SPSC-2008-018, Technical Report CERN-SPSC-2008-018. SPSC-SR-033, CERN, Geneva, 2008.

[39] N. Abgrall *et al.*, Phys. Rev. C **84**, 034604 (2011).

[40] N. Abgrall *et al.*, [The NA61/SHINE Collaboration] (2011) arXiv:1112.0150

[41] T. Eichten *et al.*, Nucl. Phys. B **44**, 333 (1972).

[42] J. V. Allaby *et al.*, Yad. Fiz. **12**, 538 (1970).

[43] Y. Hayato, Nucl. Phys. Proc. Suppl. **112**, 171 (2002).

[44] C. H. Llewellyn Smith, Phys. Rept. **3**, 261 (1972).

[45] R. P. Feynman and M. Gell-Mann, Phys. Rev. **109**, 193 (1958).

[46] R. A. Smith and E. J. Moniz, Nucl. Phys. B **43**, 605 (1972),Erratum-ibid. B 101, 547 (1975).

[47] R. Gran *et al.*, [The K2K Collaboration], Phys. Rev. D **74**, 052002 (2006).

[48] A. A. Aguilar-Arevalo *et al.*, [The MiniBooNE Collaboration], Phys. Rev. D **81**, 092005 (2010).

[49] K. Abe *et al.*, Phys. Rev. Lett. **56**, 1107 (1986).

[50] C. H. Albright *et al.*, Phys. Rev. D **14**, 1780 (1976).

[51] D. Rein, L. M. Sehgal, Annals Phys. **133**, 79 (1981).

[52] R. P. Feynman, M. Kislinger, F. Ravndal, Phys. Rev. D **3**, 2706 (1971)

[53] A. Rodriguez et al. [The K2K Collaboration], Phys. Rev. D **78**, 032003 (2008).

[54] S. Nakayama et al. [The K2K Collaboration], Phys. Lett. B **619**, 255 (2005).

[55] A. A. Aguilar-Arevalo et al. [MiniBooNE Collaboration], Phys. Rev. Lett. **103**, 081801 (2009).

[56] A. A. Aguilar-Arevalo et al. [MiniBooNE Collaboration], Phys. Rev. D **81**, 013005 (2010).

[57] Y. Kurimoto et al. [SciBooNE Collaboration], Phys. Rev. D **81**, 033004 (2010).

[58] M. Gluck, E. Reya and A. Vogt, Eur. Phys. J. C **5**, 461 (1998).

[59] A. Bodek and U. K. Yang, arXiv:hep-ex/0308007

[60] M. Nakahata et al. [The KAMIOKANDE Collaboration], J. Phys. Soc. Jap. **55**, 3786 (1986).

[61] T. Sjostrand, Comput. Phys. Commun. **82**, 74 (1994).

[62] D. Rein and L. M. Sehgal, Nucl. Phys. B **223**, 29 (1983).

[63] D. Rein and L. M. Sehgal, Phys. Lett. B **657**, 207 (2007).

[64] M. Hasegawa et al. [The K2K Collaboration], Phys. Rev. Lett. **95**, 252301 (2005).

[65] K. Hiraide et al. [The SciBooNE Collaboration], Phys. Rev. D **78**, 112004 (2008).

[66] Y. Kurimoto et al. [The SciBooNE Collaboration], Phys. Rev. D **81**, 111102 (2010).

[67] P. de Perio *et al.*, *2010a Neutrino Interaction Systematic Uncertainty Choices for the NEUT Generator*, (T2K Internal Note).

[68] P. de Perio *et al.*, *NEUT Nuclear Effects (FSI)*, (T2K Internal Note).

[69] S. Agostinelli *et al.*, Nucl. Instrum. Meth. A **506**, 250 (2003).

[70] http://geant4.web.cern.ch/geant4/

[71] M. Bass *et al. Quality Assessment of the 2010a Data Set at ND280*, *Quality Assessment Strategy of the 2010b Data Set at ND280*, *Data Quality at the Near Detectors for Run 2* (T2K Internal Notes).

[72] P. V. C. Hough, *Machine Analysis of Bubble Chamber Pictures*, Proc. Int. Conf. High Energy Accelerators and Instrumentation (1959).

[73] R. E. Kalman, *Transaction of the ASME*, Journal of Basic Engineering, 35-45 (1960).

[74] C. D. McGrew, *A Search for Baryon Nonconservation using the IMB-3 Detector*, PhD. Thesis, UC Irvine 1994.

[75] Rene Brun and Fons Rademakers, ROOT - An Object Oriented Data Analysis Framework, Proceedings AIHENP'96 Workshop, Lausanne, Sep. 1996, Nucl. Instrum. Meth. in Phys. Res. A **389** (1997) 81-86. See also http://root.cern.ch/.

[76] I. J. Taylor *et al.*, *Crosscheck of High-Energy Nue Event Rate with the PØD* (T2K Internal Note).

[77] W. Verkerke, D. Kirkby, *The RooFit Users Manual 2.91*, available at http://root.cern.ch

[78] I. Taylor, Private communication.

[79] K. Gilje, *PØD Geometry and Mass*, (T2K Internal Note).

[80] P. de Perio *et al.*, *NEUT Systematic Studies for the 2010a Analysis* (T2K Internal Note).

[81] N. Abgrall *et al.*, *Beam Update for 2010a Nue Analysis Using Run I+II Data*, (T2K Internal Note).

[82] Clark McGrew, Private communication.

[83] Walter Toki, Private communication.

Appendix A

PØDule Construction

The PØD was constructed at Stony Brook University between the summer of 2008 until the spring of 2009 when the entire detector was shipped to Japan. One of the major tasks was the construction of the 40 PØDules along with 4 spares. This chapter describes the step-by-step construction of an individual PØDule.

A.1 Construction Crew

The crew consisted of approximately 6 people. One person was deemed the shift leader and was in charge of overseeing each step of the construction. One person was tasked with managing the mixing and pouring of epoxy. The rest of the crew performed the actual construction.

A.2 Preparation

The first step of PØDule construction was the preparation of materials. The list of materials is shown in Figure A.1. Once the materials were assembled, the gluing preparation would begin. This mostly consisted of cleaning the lab space and individual components of excess debris. A dry fit was also performed in order to ensure the quality of the components before the actual gluing stage began. The gluing preparation is shown in Figure A.2.

A.3 Gluing

The PØDule gluing was done on a custom made assembly table. The table was made of poured epoxy to ensure flatness. In the epoxy, holes for alignment pins were inserted to allow precision alignment of the individual components during gluing.

First, a the black plastic HDPE light-tight skin was placed on the table and into position using the alignmen pins. Next, a batch of HYSOL epoxy was mixed. The exact ratio of epoxy to hardener was recorded on a traveler along with the total mass of epoxy prepared, see Figure A.3. Next, workers applied a layer of epoxy to the surface of the skin using paint rollers. Next, workers placed the four outer PVC frames into position around the edges of the skin and applied epoxy to the corners of the frames to keep the joints strong. Next, a layer of x scintillator planks were placed into position on the skin. In order to align the scintillator channels, steel pins were inserted through the holes in the PVC frame and into the holes in the scintillator bars. Next, a layer of epoxy was applied to the top of the scintillator bars. When finished workers placed the layer of y scintillator planks into position and the processes was repeated. Finally, the workers applied the HYSOL epoxy to the top of the scintillator planks as well as the top edge of the PVC frames. When finished, the top light tight skin was placed into position

A.4 Vacuum Curing

The PØDules were placed under vacuum pressure for 12 hours overnight in order to allow the epoxy to harden. The PØDules were first covered with a layer of protective blankets in order to prevent epoxy from sticking to the vacuum bag. Once covered, a custom made aluminum frame was placed over the PØDule. The frame was fitted with a plastic bag on top to provide the downward pressure on the PØDule for the duration of the curing time. On the outside of the frame was a gasket where the vacuum pump was attached. The pump provided 0.5 atm of pressure on the PØDule. Once completed, each PØDule was tested for quality control by the shift leader. See Figures A.4-A.7.

Checklist of Materials Required

- ☐ - 4 PVC frames(2 LIS / 2 photosensor)
- ☐ - 8 6mm stainless steel bushings
- ☐ - 28 5mm stainless steel bushing
- ☐ - 36 stainless steel pins
- ☐ - 2 light tight skins
- ☐ - 8 short planks (2 #4 planks / 6 #3 planks)
- ☐ - 8 long planks (2 #2 planks / 6 #1 planks)
- ☐ - 8 PVC filler bars (4 long / 4 short)
- ☐ - Pins for fiber holes
- ☐ - Pin removal tool
- ☐ - 260 light injection fiber guides
- ☐ - Tool to insert guides
- ☐ - Epoxy resin
- ☐ - Epoxy hardener
- ☐ - 3 mixing buckets
- ☐ - 3 mixing sticks
- ☐ - Epoxy measuring scale
- ☐ - 2 paint rollers
- ☐ - 12 small paint brushes
- ☐ - 2 roller trays
- ☐ - Vacuum frame
- ☐ - Vacuum pump and hose
- ☐ - Putty for vacuum leaks
- ☐ - Long nosed pliers
- ☐ - Rubber mallet
- ☐ - Flathead screwdriver
- ☐ - Plastic gloves
- ☐ - Paper towel, brown and white
- ☐ - Cotton swabs
- ☐ - Cleaning alcohol
- ☐ - Scissors
- ☐ - Non-stick clear plastic sheet
- ☐ - Cloth vacuum sheet
- ☐ - Foam space fillers for vacuum
- ☐ - Mold release
- ☐ - Logbook
- ☐ - Tables
- ☐ - 2 Glue carts
- ☐ - 50 grit sandpaper
- ☐ - Newspaper for covering table
- ☐ - Flashlight
- ☐ - Mirror tool

1

Figure A.1: Materials required for PØDule construction.

Checklist for Gluing Preparation

PØDule Number: ____ **Date:** _____

- ☐ - Clean gluing table
- ☐ - Clean lab tables
- ☐ - Sweep lab floor
- ☐ - Cut skins and drill holes
- ☐ - Cut 1mm off the corner of each skin
- ☐ - Lightly sand one side of skin
- ☐ - Workers wearing gloves
- ☐ - Clean one side of skin, flip, place on clean table and clean other side
- ☐ - Clean planks
- ☐ - Clean PVC frames
- ☐ - Apply mold release to pins
- ☐ - Inspect vacuum frame gasket for damage
- ☐ - Perform dry fit
- ☐ - Prepare logbook entry

1

Figure A.2: PØDule gluing preparation

Checklist for Preparing Epoxy

Epoxy Manager: _____ **Date:** _____
PØDule Number: _____

- ☐ ☐ ☐ - Cut plastic ring and open cans with a screwdriver
- ☐ ☐ ☐ - Verify that the ratio of resin to hardener is 100:6
- ☐ ☐ ☐ - Mix resin and hardener in glue bucket
- ☐ ☐ ☐ - Stir mixture thoroughly for approximately 200 turns
- ☐ ☐ ☐ - Pour glue into 2 roller trays
- ☐ ☐ ☐ - Save a sample of the batch and record number as ddmmyy-batch#
- ☐ ☐ ☐ - Record information on spaces below
- ☐ ☐ ☐ - Record information in logbook if necessary

Epoxy Batch #1

Start Time: _____

Batch Data: _____ **g Resin** _____ **g Hardener**

Sample # _____

End Time: _____

Epoxy Batch #2

Start Time: _____

Batch Data: _____ **g Resin** _____ **g Hardener**

Sample # _____

End Time: _____

Epoxy Batch #3

Start Time: _____

Batch Data: _____ **g Resin** _____ **g Hardener**

Sample # _____

End Time: _____

1

Figure A.3: Checklist for epoxy mixing

PØDule Assembly Checklist

PØDule Number: _____ **Date:** _____

Number of Workers: _____

Shift Leader: _____

Glue Crew:

Rollers: _____ and _____
Brushers: _____ and _____
Cleaner: _____

Epoxy Manager: _____

Plank Crew: _____ **and** _____

Pin Crew: _____ **and** _____

1

Figure A.4: Checklist for shift leader

Preparation

- ☐ - Verify that the necessary materials for gluing are present
- ☐ - Verify that the necessary preparation steps have been performed
- ☐ - Assign workers into various crews

Installation of Bottom Light-Tight Skin

Start Time: _____

- ☐ - Layer brown paper towel around edge of table
- ☐ - Layer sheets of clear plastic on gluing table making sure to extend beyond the PØDule frame but not the vacuum frame.
- ☐ - Place skin on table, sanded side up, and align with holes
- ☐ - Inspect skin for any debris and wipe down if necessary
- ☐ - Epoxy manager prepares epoxy batch #1
- ☐ - Glue crew applies epoxy to skin
- ☐ - Shift leader inspects epoxy distribution
- ☐ - Insert 6mm and 5mm pins

Installation of Frames

Start Time: _____

- ☐ - Y-axis light injection frame installed holes up on side 2
- ☐ - Y-axis photosensor frame installed holes up on side 4
- ☐ - Glue crew applies epoxy to each of the four joints
- ☐ - X-axis light injection frame installed holes down on side 1
- ☐ - X-axis photosensor frame installed holes down on side 3
- ☐ - Cleaner removes excess epoxy from frame joints
- ☐ - Shift leader inspects corner joints

2

Figure A.5: Checklist for shift leader

Installation of Y-axis Planks

Start Time: _____

Position 1 Plank #: _____ **Position 2 Plank #:** _____
Position 3 Plank #: _____ **Position 4 Plank #:** _____
Position 5 Plank #: _____ **Position 6 Plank #:** _____
Position 7 Plank #: _____ **Position 8 Plank #:** _____

- ☐ - Glue crew applies epoxy to bottom of Y-axis frames
- ☐ - Plank crew inserts planks flush against X-axis LIS frame
- ☐ - Glue applied to PVC spacers and inserted
- ☐ - Pin crew inserts pins and light injection fiber guides
- ☐ - Epoxy manager prepares epoxy batch #2
- ☐ - Glue crew applies epoxy to Y-axis planks
- ☐ - Shift leader inspects epoxy distribution, pins, and fiber guides

Installation of X-axis Planks

Start Time: _____

Position 1 Plank #: _____ **Position 2 Plank #:** _____
Position 3 Plank #: _____ **Position 4 Plank #:** _____
Position 5 Plank #: _____ **Position 6 Plank #:** _____
Position 7 Plank #: _____ **Position 8 Plank #:** _____

- ☐ - Glue crew applies epoxy to top of X-axis frames
- ☐ - Plank crew inserts planks flush against Y-axis LIS frame
- ☐ - Glue applied to PVC spacers and inserted
- ☐ - Pin crew inserts pins and light injection fiber guides
- ☐ - Epoxy manager prepares epoxy batch #3
- ☐ - Glue crew applies epoxy to X-axis planks
- ☐ - Shift leader inspects epoxy distribution, pins, and fiber guides

Installation of Top Light Tight Skin

Start Time: _____

- ☐ - Position light tight skin rough side down on one side of the PØDule
- ☐ - Roll the rest of the skin onto the PØDule to remove air bubbles

Figure A.6: Checklist for shift leader

Final Pre-Cure Inspection and Checkout

Start Time: _____

- ☐ - Remove any excess epoxy
- ☐ - Ensure that all steel alignment pins are installed on the readout frames
- ☐ - Ensure that all LIS Fiber guides are installed to their proper depth in LIS frames
- ☐ - Ensure that all alignment pins and bushing are properly installed
- ☐ - Check for air bubbles under top skin

Vacuum Bagging, Radiator Assembly and Curing

Start Time: _____

- ☐ - Prepare batch of epoxy for radiator if necessary
- ☐ - Cover PØDule with layer of clear plastic sheet
- ☐ - Cover plastic sheet with vacuum fabric
- ☐ - Position foam spacers around PØDule
- ☐ - Position vacuum frame over PØDule

Vacuum Set Pressure: _____

Date and Time of End of Cycle (18 hours minimum) _____

Time of Removal From Gluing Table: _____

Post Curing Inital QC:

Date: _____

Time: _____

Inspectors: _____ **and** _____

- ☐ - Perform light tests on individual channels
- ☐ - Insert test fibers into each channel

Approved for use in the PØD by: _____

4

Figure A.7: Checklist for shift leader

Appendix B

Determining the Optimum Water-In/Water-Out Data Taking

B.1 The Water-In Water-Out Subtraction

To extract the NC1π^0 cross section on water, a statistical subtraction of water-in and water-out event measurements will be performed. This leads to the question of what the optimal ratio of water-in to water-out data-taking is such that the uncertainty of the measurement is minimized.

We start by considering that for event measurements $N_{IN(OUT)}$ with a POT exposure $t_{IN(OUT)}$ corresponding to the water-in(out) data taking periods, the total event rate on water is given by the time normalized difference

$$N^{\pi^0}_{H_2O} = N_{IN}(t_{IN}) - \frac{t_{IN}}{t_{OUT}} N_{OUT}(t_{OUT}). \tag{B.1}$$

If we consider that the water-in and water-out data taking periods can be represented as fractions of some total period T such that

$$t_{IN} = xT, t_{OUT} = (1-x)T \tag{B.2}$$

then we can represent the total event rate in Equation B.1 as a function of this water-in fraction as

$$N^{\pi^0}_{H_2O} = N_{IN}(xT) - \alpha N_{OUT}((1-x)T), \tag{B.3}$$

where $\alpha = \frac{x}{1-x}$ is the exposure ratio. For the individual water-in and water-out periods, the measured number of events is assumed to be the measured number of signal events corrected for the efficiency, and with the background subtracted according to

$$N_{IN}(xT) = \epsilon_{IN}^{-1}\tilde{N}_{IN}(xT) - \bar{N}_{IN}(xT) \quad \text{(B.4)}$$
$$N_{OUT}(xT) = \epsilon_{OUT}^{-1}\tilde{N}_{OUT}((1-x)T) - \bar{N}_{OUT}((1-x)T), \quad \text{(B.5)}$$

where $\tilde{N}$ the measured number of events, and $\bar{N}$ is the background.

We further assume that the measured number of events is equal to the rate multiplied by the total exposure such that

$$N_{IN}(xT) = \epsilon_{IN}^{-1}\tilde{R}_{IN}xT - \bar{R}_{IN}xT \quad \text{(B.6)}$$
$$N_{OUT}((1-x)T) = \epsilon_{OUT}^{-1}\tilde{R}_{OUT}(1-x)T - \bar{R}_{OUT}(1-x)T. \quad \text{(B.7)}$$

To determine the optimum exposure we minimize the statistical error with respect to the fraction so that

$$\frac{d}{dx}\frac{\Delta N_{H_2O}^{\pi^0}}{N_{H_2O}^{\pi^0}} = 0. \quad \text{(B.8)}$$

Differentiating this equation yields

$$N_{H_2O}^{\pi^0}\frac{d}{dx}\Delta N_{H_2O}^{\pi^0} - \Delta N_{H_2O}^{\pi^0}\frac{d}{dx}N_{H_2O}^{\pi^0} = 0. \quad \text{(B.9)}$$

Inserting Equations B.6 and B.7 into Equation B.3 we obtain

$$N_{H_2O}^{\pi^0} = \left[(\epsilon_{IN}^{-1}\tilde{R}_{IN} - \bar{R}_{IN}) - (\epsilon_{OUT}^{-1}\tilde{R}_{OUT} - \bar{R}_{OUT})\right] xT \quad \text{(B.10)}$$

The derivative, $\frac{d}{dx}N_{H_2O}^{\pi^0}$ is trivial:

$$\frac{d}{dx}N_{H_2O}^{\pi^0} = \frac{N_{H_2O}^{\pi^0}}{x}. \quad \text{(B.11)}$$

For the statistical error, we assume poisson statistics, so that the error is simply the square root of the number of events

$$\begin{aligned}\Delta N_{IN}(xT) &= \sqrt{N_{IN}(xT)} \\ &= \sqrt{(\epsilon_{IN}^{-1}\Delta\tilde{N}_{IN}(xT))^2 + (\Delta\bar{N}_{IN}(xT))^2} \\ &= \sqrt{(\epsilon_{IN}^{-1})^2\tilde{R}_{IN}xT + \bar{R}_{IN}xT} \quad \text{(B.12)}\end{aligned}$$

and similarly for N_{OUT}

$$\begin{aligned}\Delta N_{OUT}((1-x)T) &= \sqrt{N_{OUT}((1-x)T)} \\ &= \sqrt{(\epsilon_{OUT}^{-1}\Delta\tilde{N}_{OUT}((1-x)T))^2 + (\Delta\bar{N}_{OUT}((1-x)T))^2} \\ &= \sqrt{(\epsilon_{OUT}^{-1})^2\tilde{R}_{OUT}(1-x)T + \bar{R}_{OUT}(1-x)T} \qquad \text{(B.13)}\end{aligned}$$

It follows from Equation B.13 that

$$\alpha[\Delta N_{OUT}((1-x)T)]^2 = [\Delta N_{OUT}((xT)]^2, \qquad \text{(B.14)}$$

which will be useful later.

Using Equation B.3 the statistical error of the number of events is the sum in quadrature of the IN and OUT errors:

$$\Delta N_{H_2O}^{\pi^0} = \sqrt{[\Delta N_{IN}(xT)]^2 + \alpha^2[\Delta N_{OUT}((1-x)T)]^2}. \qquad \text{(B.15)}$$

The error on the exposure ratio α is assumed to be negligible. Using Equation B.15 the derivative can be calculated:

$$\begin{aligned}&\Delta N_{H_2O}^{\pi^0}\frac{d}{dx}\Delta N_{H_2O}^{\pi^0} = \\ &\quad \big[\Delta N_{IN}(xT)]\frac{d}{dx}[\Delta N_{IN}(xT)] \\ &\quad +[\Delta N_{OUT}((1-x)T)]^2\alpha\frac{d}{dx}\alpha \\ &\quad +\alpha^2[\Delta N_{OUT}((1-x)T)]\frac{d}{dx}[\Delta N_{OUT}((1-x)T)\big]. \qquad \text{(B.16)}\end{aligned}$$

Calculating each term individually we get

$$\frac{d}{dx}\Delta N_{IN}(xT) = \frac{1}{2}\frac{(\epsilon_{IN}^{-1})^2\tilde{R}_{IN}T + \bar{R}_{IN}T}{\sqrt{(\epsilon_{IN}^{-1})^2\tilde{R}_{IN}xT + \bar{R}_{IN}xT}}$$
$$= \frac{1}{2}\frac{1}{x}\Delta N_{IN}(xT) \quad \text{(B.17)}$$

$$\frac{d}{dx}\Delta N_{OUT}((1-x)T) = \frac{1}{2}\frac{(\epsilon_{OUT}^{-1})^2\tilde{R}_{OUT}T + \bar{R}_{OUT}T}{\sqrt{[(\epsilon_{OUT}^{-1})^2\tilde{R}_{OUT}((1-x)T) + \bar{R}_{OUT}]((1-x)T)}}$$
$$= -\frac{1}{2}\frac{1}{1-x}\Delta N_{OUT}((1-x)T) \quad \text{(B.18)}$$

$$\frac{d}{dx}\alpha = \frac{\alpha^2}{x^2} \quad \text{(B.19)}$$

Plugging these into Equation B.16 we get

$$2\Delta N_{H_2O}^{\pi^0}\frac{d}{dx}\Delta N_{H_2O}^{\pi^0} = \frac{1}{x}[\Delta N_{IN}(xT)]^2 + \frac{2\alpha^3}{x^2}[\Delta N_{OUT}((1-x)T)]^2 - \frac{\alpha^2}{1-x}[\Delta N_{OUT}((1-x)T)]^2. \quad \text{(B.20)}$$

This result is plugged into Equation B.9, which is then solved for x.

$$0 = N_{H_2O}^{\pi^0}\times \left[\frac{1}{2\Delta N_{H_2O}^{\pi^0}}\left[\frac{1}{x}[\Delta N_{IN}(xT)]^2 + \frac{\alpha^3(2-x)}{x^2}[\Delta N_{OUT}((1-x)T)]^2\right]\right] - \Delta N_{H_2O}^{\pi^0}\frac{N_{H_2O}^{\pi^0}}{x}. \quad \text{(B.21)}$$

The factor $N_{H_2O}^{\pi^0}$ can be factored out since it is not 0. Multiplying by $2x$ and collecting terms we get

$$\Big[\Delta N_{IN}(xT)\Big]^2 + \frac{(2-x)\alpha^3}{x}\Big[\Delta N_{OUT}((1-x)T)\Big]^2 - 2\Big[\Delta N_{H_2O}^{\pi^0}\Big]^2 = 0 \quad \text{(B.22)}$$

$$\Big[\Delta N_{IN}(xT)\Big]^2[1-2] + [\frac{(2-x)\alpha^3}{x} - 2\alpha^2]\Big[\Delta N_{OUT}((1-x)T)\Big]^2 = 0 \quad \text{(B.23)}$$

and using the result of Equation B.15

$$\begin{aligned}
\Big[\Delta N_{IN}(xT)\Big]^2 &= \alpha^2[\frac{(2-x)\alpha}{x} - 2]\Big[\Delta N_{OUT}((1-x)T)\Big]^2 \\
&= \alpha^2[\frac{2-x}{1-x} - 2]\Big[\Delta N_{OUT}((1-x)T)\Big]^2 \\
&= \alpha^3\Big[\Delta N_{OUT}((1-x)T)\Big]^2 \qquad \text{(B.24)}
\end{aligned}$$

Finally, using the result of Equation B.14 and solving for α we get

$$\alpha = \frac{\Delta N_{IN}(xT)}{\Delta N_{OUT}(xT)} \qquad \text{(B.25)}$$

and then use Equations B.12 and B.13 to obtain the final result for α:

$$\alpha = \sqrt{\frac{(\epsilon_{IN}^{-1})^2\tilde{R}_{IN} + \bar{R}_{IN}}{(\epsilon_{OUT}^{-1})^2\tilde{R}_{OUT} + \bar{R}_{OUT}}} \approx \frac{\epsilon_{OUT}}{\epsilon_{IN}}\sqrt{\frac{\tilde{R}_{IN}}{\tilde{R}_{OUT}}} \qquad \text{(B.26)}$$

According to Equation B.26 the ratio of the water-in to water-out data taking periods is proportional to the ratio of the (OUT)/(IN) efficiencies, and the square root of the ratio of the (IN)/(OUT) event rates. This makes sense because if the (IN)/(OUT) event rate is high, then it means there are more π^0s on water. However, if the water-out efficiency is so much lower than the water-in efficiency, then there will be fewer water-out π^0s to actually do the subtraction, and therefore the statistical uncertainty will be higher.

Based on initial MC studies of the PØD π^0 event rate [82], the ratio of the event rates was estimated to be 1.4. Assuming equal efficiencies, Equation B.26 yields a value of 55% of the total exposure as the optimal value of the water-in data taking. A separate calculation was performed based on considerations of the materials in the PØD for the water-in and water-out data taking. That calculation yielded the same result [83].